



UNIVERSIDADE FEDERAL DE SANTA CATARINA  
CENTRO TECNOLÓGICO  
PROGRAMA DE PÓS-GRADUAÇÃO EM ENGENHARIA ELÉTRICA

Rossano Mendes Sotoriva

**Algorithmic Approach for Optimal Design of DAB Converter**

Florianópolis  
Julho de 2024

Rossano Mendes Sotoriva

## Algorithmic Approach for Optimal Design of DAB Converter

Dissertação submetida ao Programa de Pós-Graduação em Engenharia Elétrica da Universidade Federal de Santa Catarina para a obtenção do título de Mestre em Engenharia Elétrica

**Supervisor:** Prof. Samir Ahmad Mussa, Dr.

**Co-supervisor:** Prof. Franciéli Lima de Sá, Dra.

Florianópolis  
Julho de 2024

Catálogo na fonte pela Biblioteca Universitária da Universidade Federal de Santa Catarina.  
Arquivo compilado às 15:33h do dia 08 de julho de 2024.

Rossano Mendes Sotoriva

Algorithmic Approach for Optimal Design of DAB Converter/ Rossano Mendes Sotoriva.  
- Florianópolis, Julho de 2024-  
103 p. : il. (algumas color.) ; 30 cm.

Supervisor: Prof. Samir Ahmad Mussa, Dr.

- Universidade Federal de Santa Catarina - UFSC  
Departamento de Engenharia Elétrica e Eletrônica - EEL  
Programa de Pós-Graduação em Engenharia Elétrica - PGEEL, Julho de 2024.

1. Eletrônica de Potência. 2. Conversor CC-CC Isolado. 3. Dual Active Bridge. 4.  
Comutação Suave. 5. Otimização de Conversores.

CDU 02:141:005.7

Rossano Mendes Sotoriva

**Algorithmic Approach for Optimal Design of DAB Converter**

O presente trabalho em nível de mestrado foi avaliado e aprovado por banca examinadora composta pelos seguintes membros:

Prof. André Luis Kirsten, Dr.  
Universidade Federal de Santa Catarina

Prof. Gustavo Alves de Lima Henn, Dr.  
UNILAB

Certificamos que esta é a **versão original e final** do trabalho de conclusão que foi julgado adequado para obtenção do título de Mestre em Engenharia Elétrica.

---

Prof. Telles Brunelli Lazzarin, Dr.  
Coordenador do Programa

---

Prof. Samir Ahmad Mussa, Dr.  
Orientador

Florianópolis  
Julho de 2024.



---

## Acknowledgements

Agradeço, primeiramente, a Deus pela sabedoria e pelas condições para realizar este trabalho.

À minha família, expresso minha mais profunda gratidão pelo seu apoio incondicional e incentivo constante, que foram pilares essenciais durante os momentos desafiadores e inspiradores desta jornada.

Aos meus colegas do laboratório, sou imensamente grato. Suas contribuições, conhecimentos compartilhados e o companheirismo foram cruciais para o desenvolvimento deste trabalho em especial a Eduardo Francisco Celli Grabovski e Mateus de Freitas Bueno. Cada conversa, troca de ideias e colaboração moldaram este projeto de maneira significativa.

Agradeço também a todos os professores que cruzaram meu caminho ao longo desta trajetória. Suas aulas, orientações e sabedoria foram fundamentais para minha formação acadêmica e profissional. Cada ensinamento foi um degrau importante rumo à conclusão desta dissertação.

Às instituições que possibilitaram este estudo, meu sincero reconhecimento. Ao proporcionar um ambiente propício à pesquisa foi essencial para alcançar este resultado.

Por fim, agradeço a todos que, direta ou indiretamente, contribuíram para este trabalho. Cada palavra escrita, cada ideia compartilhada, cada desafio superado foi uma peça fundamental neste quebra-cabeça acadêmico.

Que este trabalho possa contribuir de forma positiva para a comunidade acadêmica e para a sociedade como um todo.

*“O sucesso é construído de 99 por cento de fracasso.”*  
Soichiro Honda



---

## Resumo

O estudo em questão visa aprimorar um conversor Dual Active Bridge através de otimização algorítmica e explorar suas aplicações, especialmente como carregador on-board para veículos elétricos, onde é possível utilizar aplicações como V2G ou V2L, ou mesmo em outras situações que demandem conversores CC-CC isolados bidirecionais. O processo de otimização emprega um algoritmo de otimização por enxame de partículas para determinar os parâmetros construtivos ideais, incluindo o número de espiras no indutor, o comprimento do gap do indutor e as espiras nos enrolamentos do transformador primário e secundário. O objetivo é minimizar a soma global de perdas e identificar as frequências otimizadas para cada um dos quatro pontos de operação predefinidos.

Subsequentemente, é elaborada uma tabela de consulta para otimizar a frequência como variável única, garantindo a eficácia operacional do conversor on-board em diferentes níveis de potência de saída e corrente. Para validar o estudo, um conversor foi projetado e construído com uma entrada de tensão de 400 V, potência de saída de 2 kW e várias faixas de tensão de saída, variando de 300 V a 450 V. As perdas no interruptor de potência e a eficiência geral do conversor foram comparadas com cálculos teóricos e resultados de simulação obtidos do PLECS 4.7.2, além do protótipo construído para testes experimentais.

Os resultados obtidos confirmam a eficácia do método na construção de um conversor CC-CC bidirecional isolado, alcançando níveis de eficiência superiores a 95% para todos os pontos testados no protótipo construído.

**Palavras-chave:** *Dual-Active Bridge*, Design otimizado, *Particle swarm optimization*, Carregador on-board, Conversor CC-CC Isolado Bidirecional.



---

## Abstract

The aim of this study is to enhance a Dual Active Bridge converter through algorithmic optimization and explore its applications, notably as an on-board charger for electric vehicles where applications like V2G or V2L can be utilized, or in other instances requiring bidirectional isolated DC-DC converters. The optimization process employs a particle swarm optimization algorithm to determine the ideal construction parameters, including the number of turns in the inductor, the length of the inductor gap, and the turns in the primary and secondary windings of the transformer. The objective is to minimize overall losses and identify the optimized frequencies for each of the four predetermined operating points.

Subsequently, a query table is developed to optimize the frequency as a single variable, ensuring the operational efficacy of the on-board converter at different output power and current levels. To validate the study, a converter was designed and constructed with a 400 V input voltage, 2 kW output power, and various output voltage ranges from 300 V to 450 V. Power switch losses and the overall converter efficiency were compared with theoretical calculations and simulation results obtained from PLECS 4.7.2, in addition to the prototype built for experimental testing.

The obtained results corroborate the method's effectiveness in constructing an isolated bidirectional DC-DC converter, achieving efficiencies exceeding 95% for all tested points in the built prototype.

**Key-words:** Dual-Active Bridge, Optimum design, particle swarm algorithm, On-board charger, IBDC.



---

## Resumo Expandido

### Introdução

O foco global na redução das emissões de CO<sub>2</sub> tem levado à adoção fontes de energia renováveis e o uso de veículos elétricos como uma solução de transporte sustentável. No entanto, a limitada autonomia das atuais baterias de íons de lítio representa um desafio para a autonomia dos veículos, exigindo avanços na tecnologia de baterias e na infraestrutura de carregamento. Além disso, existem limitações na rede elétrica em áreas residenciais devido à alta demanda de carga para carregamento dos veículos elétricos.

Para enfrentar os numerosos desafios apresentados para um mundo sustentável, têm-se realizado pesquisas em diversas áreas da tecnologia, uma delas são os conversores CC-CC isolados bidirecionais. Os conversores oferecem vantagens como volume, custo e massa reduzidos, baixo ruído de conversão, alta densidade de potência e eficiência. Portanto são adequados para diversas aplicações como conexões de barramento, conversão de tensão, transmissão de energia e isolamento elétrico em redes de distribuição CC.

Alguns dos exemplos de aplicações nos quais é possível utilizar conversores CC-CC isolados bidirecionais são:

- Microrredes nos quais fontes de energia renováveis como fotovoltaica e energia eólica são usadas como recursos energéticos distribuídos. No entanto, devido à natureza intermitente dessas fontes de energia, medidas como a distribuição de sistemas de armazenamento de energia na rede elétrica podem mitigar os efeitos da falta de confiabilidade dessas fontes de energia. Esses sistemas podem incluir baterias de íons de lítio, super capacitores ou até mesmo veículos elétricos em uma aplicação Vehicle to Grid(V2G).
- Carregadores de veículos elétricos a medida que a adoção cresce diariamente, é necessário desenvolver tecnologias de carregamento para uma transição viável para veículos elétricos no futuro.

Os conversores CC-CC isolados bidirecionais, podem ser aplicadas desde geração até distribuição de energia. Para projetar um conversor para sua aplicação específica, optou-se por utilizar uma abordagem computacional, e otimizar o conversor para uma maior eficiência, ao tornar a função a ser otimizada as perdas do conversor.

## **Objetivos**

O principal objetivo deste estudo é projetar um conversor de DAB usando algoritmo de otimização. Os objetivos específicos são:

- Analisar a performance do conversor DAB projetado pelo algoritmo de otimização;
- Otimizar o conversor para diferentes condições, mantendo os mesmos componentes e verificando se há significantes diferenças nos resultados da otimização.

## **Resultados**

Observando os resultados obtidos por meio do *particle swarm optimization* (*PSO*) nota-se que é possível se otimizar uma mesma configuração de componentes para varias diferentes configurações enquanto mantendo os níveis de potencia do conversor. O algoritmo de otimização permite o refinamento contínuo do projeto do conversor, utilizando os parâmetros de construção disponíveis para garantir a melhor configuração possível para o conversor.

Os resultados obtidos confirmam níveis de eficiência superiores a 95% para todos os pontos testados no protótipo construído, confirmando a eficácia do método na construção de um conversor CC-CC bidirecional isolado, alcançando níveis de eficiência superiores a 95% para todos os pontos testados no protótipo construído.

**Palavras-chave:** *Dual-Active Bridge*, Design otimizado, *Particle swarm optimization*, Carregador on-board, Conversor CC-CC Isolado Bidirecional.

---

## List of Figures

|   |    |
|---|----|
| Figure 1.1 – Several energy sources grid. . . . .   | 20 |
| Figure 1.2 – IBDC Application on electrical grid. . . . .   | 21 |
| Figure 1.3 – ISOP structure IBDC scheme based on DAB modules. . . . .   | 22 |
| Figure 1.4 – Microgrid IBCD application. . . . .  | 23 |
| Figure 1.5 – On-board charger. . . . .  | 25 |
| Figure 1.6 – EV charging system on-board/off-board charger. . . . .   | 26 |
| Figure 1.7 – Basic structure of the particle swarm optimization. . . . .  | 27 |
| Figure 2.1 – Dual Active Bridge (DAB) converter. . . . .  | 29 |
| Figure 2.2 – Power transfer scheme (a) where the $\phi$ angle is higher than 0 and the power flows from $V_1$ to $V_2$ , and (b) where the $\phi$ angle is lower than 0 and the power flows from $V_2$ to $V_1$ . . . . . | 30 |
| Figure 2.3 – DAB Single phase shift modulation. . . . .   | 31 |
| Figure 2.4 – DAB interval I: Negative inductor current(a); Positive inductor current(b). . . . .  | 32 |
| Figure 2.5 – DAB interval II. . . . .   | 32 |
| Figure 2.6 – DAB interval III: Positive inductor current(a); Negative inductor current(b). . . . .  | 33 |
| Figure 2.7 – DAB interval IV. . . . .   | 34 |
| Figure 2.8 – Simplified DAB Model. . . . .  | 34 |
| Figure 2.9 – Transformer voltage and inductor current. . . . .  | 35 |
| Figure 2.10 – ZVS range with normalized output power over voltage ratio. . . . .  | 38 |
| Figure 3.1 – Design optimization flowchart for obtaining construction parameters. . . . .   | 41 |
| Figure 3.2 – Switching loss flowchart. . . . .  | 45 |
| Figure 3.3 – PWM generator based on lookup table. . . . .   | 49 |
| Figure 4.1 – Energy interpolation curves. . . . .   | 54 |
| Figure 4.2 – Switches power losses [W]. . . . .   | 55 |
| Figure 4.3 – Magnetic elements power losses [W]. . . . .  | 56 |
| Figure 4.4 – Components temperature rise [°C]. . . . .  | 57 |
| Figure 4.5 – Theoretical converter’s efficiency. . . . .  | 58 |
| Figure 4.6 – Switches power losses [W]. . . . .   | 60 |
| Figure 4.7 – Magnetic elements power losses. . . . .  | 61 |
| Figure 4.8 – Components temperature rise [°C]. . . . .  | 62 |
| Figure 4.9 – Theoretical converter’s efficiency. . . . .  | 63 |
| Figure 4.10 – Converters efficiency comparison. . . . .   | 64 |
| Figure 4.11 – Frequency lookup table ranging from 20 kHz < to > 80 kHz. . . . .   | 65 |
| Figure 4.12 – Phase-Shift lookup table ranging from < 10 $\phi$ to > 55 $\phi$ . . . . .  | 65 |
| Figure 4.13 – Dab Efficiency map FF ranging from <0.1% to >97%. . . . .   | 66 |
| Figure 4.14 – Dab Efficiency map for VF ranging from < 0.1% to > 97%. . . . .   | 66 |

|   |     |
|---|-----|
| Figure 4.15–ZVS regions - fixed frequency. . . . .  | 67  |
| Figure 4.16–ZVS regions - variable frequency. . . . .   | 68  |
| Figure 5.1 – Inductor impedance analyser. . . . .   | 70  |
| Figure 5.2 – Assembled magnetics: (a) inductor; (b) transformers. . . . .                                   | 71  |
| Figure 5.3 – Model transformer. . . . .   | 71  |
| Figure 5.4 – Leakage inductance characterization. . . . .   | 71  |
| Figure 5.5 – Measured inductances transformer I primary and secondary. . . . .                              | 72  |
| Figure 5.6 – Measured total inductance transformer I while the opposing side is<br>short-circuited. . . . . | 72  |
| Figure 5.7 – Measured inductances transformer II primary and secondary. . . . .                             | 73  |
| Figure 5.8 – Measured total inductance transformer II. . . . .  | 73  |
| Figure 5.9 – DAB test setup schematic. . . . .  | 75  |
| Figure 5.10–DAB converter prototype. . . . .  | 76  |
| Figure 5.11–Converter’s primary and secondary waveforms in PLECS simulation -<br>300 V. . . . .             | 77  |
| Figure 5.12–Converter’s primary and secondary waveforms - 300 V. . . . .                                    | 78  |
| Figure 5.13–300 V wattmeter results. . . . .  | 79  |
| Figure 5.14–Converter’s primary and secondary waveforms in PLECS simulation -<br>350 V. . . . .             | 80  |
| Figure 5.15–Converter’s primary and secondary waveforms - 350 V. . . . .                                    | 81  |
| Figure 5.16–350 V wattmeter results. . . . .  | 82  |
| Figure 5.17–Converter’s primary and secondary waveforms in PLECS simulation -<br>400 V. . . . .             | 83  |
| Figure 5.18–Converter’s primary and secondary waveforms - 400 V. . . . .                                    | 84  |
| Figure 5.19–400 V wattmeter results. . . . .  | 85  |
| Figure 5.20–Converter’s primary and secondary waveforms in PLECS simulation -<br>450 V. . . . .             | 86  |
| Figure 5.21–Converter’s primary and secondary waveforms - 450 V. . . . .                                    | 87  |
| Figure 5.22–450 V wattmeter results. . . . .  | 88  |
| Figure 5.23–Converter efficiency curve. . . . .   | 89  |
| Figure A.1–DAB top layer. . . . .   | 101 |
| Figure A.2–DAB botton layer. . . . .  | 102 |
| Figure A.3–DAB command board top layer. . . . .   | 103 |
| Figure A.4–DAB command board botton layer. . . . .  | 103 |

---

## List of Tables

|   |    |
|---|----|
| Table 1.1 – Charging specifications of some available EVs. . . . .              | 25 |
| Table 2.1 – Switching states. . . . .   | 34 |
| Table 4.1 – Optimization limits. . . . .  | 52 |
| Table 4.2 – Material list. . . . .  | 52 |
| Table 4.3 – Optimum design summary. . . . .                                     | 53 |
| Table 4.4 – Converter’s frequency and phase shift and operation points. . . . . | 53 |
| Table 4.5 – Switches power losses. . . . .                                      | 54 |
| Table 4.6 – Magnetics elements power losses. . . . .                            | 55 |
| Table 4.7 – Magnetics elements density flux. . . . .                            | 56 |
| Table 4.8 – Components temperature rise. . . . .                                | 56 |
| Table 4.9 – Theoretical converter’s efficiency. . . . .                         | 57 |
| Table 4.10–Optimum design summary variable frequency. . . . .                   | 59 |
| Table 4.11–Converter’s frequency and phase shift - variable frequency. . . . .  | 59 |
| Table 4.12–Power switch losses - variable frequency. . . . .                    | 60 |
| Table 4.13–Magnetics elements power losses. . . . .                             | 60 |
| Table 4.14–Magnetics elements density flux. . . . .                             | 61 |
| Table 4.15–Components temperature rise. . . . .                                 | 61 |
| Table 4.16–Theoretical converter’s efficiency. . . . .                          | 62 |
| Table 4.17–Optimum design summary comparison. . . . .                           | 63 |
| Table 5.1 – DAB prototype parameters . . . . .                                  | 69 |
| Table 5.2 – Converter’s testing parameters configuration. . . . .               | 75 |
| Table 5.3 – 300 V PLECS simulation results. . . . .                             | 77 |
| Table 5.4 – 300 V Results comparison . . . . .                                  | 79 |
| Table 5.5 – 350 V PLECS simulation results. . . . .                             | 81 |
| Table 5.6 – 350 V Results comparison . . . . .                                  | 82 |
| Table 5.7 – 400 V PLECS simulation results. . . . .                             | 84 |
| Table 5.8 – 400 V Results comparison . . . . .                                  | 85 |
| Table 5.9 – 450 V PLECS simulation results. . . . .                             | 86 |
| Table 5.10–450 V Results comparison . . . . .                                   | 88 |
| Table A.1 –Capacitors. . . . .  | 97 |



---

## List of abbreviations and acronyms

|      |   |
|------|---|
| AWG  | American Wire Gauge                     |
| DAB  | Dual Active Bridge Converter            |
| EV   | Electric Vehicle                        |
| EVSE | Electric Vehicle Supply Equipment       |
| IBDC | Isolated Bidirectional DC-DC Converters |
| iGSE | Improved Generalized Steinmetz Equation |
| NPZ  | No Project Zone                         |
| OBC  | On-board Charger                        |
| PFC  | Power Factor Correction                 |
| PSO  | Particle Swarm Optimization             |
| SPS  | Single Phase-Shift Modulation           |
| V2G  | Vehicle to Grid                         |
| V2H  | Vehicle to House                        |
| V2L  | Vehicle to Load                         |
| ZVS  | Zero Voltage Switching                  |

---

## List of symbols

|                  |  |
|------------------|--|
| $\Delta B_L$     | Peak-to-peak density flux in the inductor                    |
| $\Delta B_{trs}$ | Peak-to-peak density flux in the transformer                 |
| $\Delta T$       | Temperature rise   |
| $A_c$            | Cross-sectional area of the magnetic core                    |
| $A_e$            | Effective magnetic cross section                             |
| $B_{max}$        | Peak value for magnetic flux density                         |
| $dB_L(t)/dt$     | Derivative of the density flux in the inductor               |
| $dB_{trs}(t)/dt$ | Derivative of the density flux in the transformer            |
| $D_m$            | Diameter of the circular cross section of the wire           |
| $E_{off}$        | Turn off energies  |
| $E_{on}$         | Turn on energies   |
| $F_p$            | Proximity effect factor                                      |
| $F_s$            | Skin effect factor   |
| $I_L$            | Inductor's current   |
| $I_{rms,pri}$    | RMS value of current for the primary side of the converter   |
| $I_{rms,sec}$    | RMS value of current for the secondary side of the converter |
| $I_{sw}$         | Switching currents   |
| $i_{Avg}$        | Average current  |
| $i_{L,n}$        | Inductor current in $n^{th}$ harmonic                        |
| $i_{p,pk}$       | Peak current in the primary power switch                     |
| $i_{p,rms}$      | RMS current in the primary power switch                      |
| $i_{s,pk}$       | Peak current in the secondary power switch                   |
| $i_{s,rms}$      | RMS current in the secondary power switch                    |

|             |  |
|-------------|--|
| $i_{trs,n}$ | Transformer current at $n^{th}$ harmonic       |
| $k$         | Number of strands of the litz wire             |
| $L$         | Inductance                                     |
| $L_{mag}$   | Magnetizing inductance                         |
| $L_{tr}$    | Leakage inductance                             |
| $l_e$       | Effective magnetic path length                 |
| $lg$        | Length of inductor's gap                       |
| $\mu_0$     | Magnetic permeability of free space            |
| $\mu_{ef}$  | Effective relative permeability                |
| $N_l$       | Number of layers                               |
| $N_L$       | Number of turns of the inductor                |
| $N_p$       | Number of turns of the transformer's secondary |
| $N_s$       | Number of turns of the transformer's primary   |
| $N_T$       | Number of turns of the windings                |
| $N_{sw}$    | Number of switches on the heat-sink            |
| $P_{cond}$  | Conduction losses                              |
| $P_{cw}$    | Total power loss of the element                |
| $P_{off}$   | Turn off switching losses                      |
| $P_{on}$    | Turn on switching losses                       |
| $P_{semi}$  | Power losses on the semiconductors             |
| $P_{sw}$    | Total switching losses                         |
| $P_{tr}$    | Transformer losses                             |
| $P_v$       | Core volumetric losses                         |
| $P_{jc}$    | Junction to case thermal resistance            |
| $P_{htk}$   | Heat-sink thermal resistance                   |
| $\phi$      | Phase shift angle                              |
| $\Psi$      | Power loss density of the element              |
| $R_{ds-on}$ | Drain source on-state resistance               |
| $R_{htiso}$ | Insulator thermal resistance                   |



|                  |   |
|------------------|---|
| $R_{w,ac}$       | AC resistance of the wire                             |
| $R_{w,dc}$       | DC resistance of the wire                             |
| $S_n$            | Power switch number n                                 |
| $S_p$            | Primary switches                                      |
| $S_s$            | Secondary switches                                    |
| $T_a$            | Ambient temperature                                   |
| $T_{L,limit}$    | Inductor's temperature limit                          |
| $T_L$            | Inductor's temperature                                |
| $T_{Semi,limit}$ | Power switches temperature limit                      |
| $T_{Semi}$       | Power switches temperature                            |
| $T_{trs,limit}$  | Transformer temperature limit                         |
| $T_{trs}$        | Transformer temperature                               |
| $V_1$            | Voltage source 1                                      |
| $V_2$            | Voltage source 2                                      |
| $V_i$            | Input voltage   |
| $V_{Np}$         | Transformer primary's voltage                         |
| $V_{Ns}$         | Transformer secondary's voltage                       |
| $V_o$            | Output voltage  |
| $V_{bus}$        | Bus voltage   |
| $\rho_w$         | Resistivity of the material                           |
| $\eta$           | Efficiency  |
| $\eta_p$         | Equivalent porosity factor of the litz wire           |
| $\delta_w$       | Skin depth of the wire                                |
| $d_l$            | Diameter of the litz wire                             |
| $d_w$            | The equivalent square cross section width of the wire |

---

# CONTENTS

|          |  |           |
|----------|--|-----------|
| <b>1</b> | <b>INTRODUCTION</b> . . . . .                        | <b>20</b> |
| 1.1      | ISOLATED BIDIRECTIONAL DC-DC CONVERTER . . . . .     | 21        |
| 1.1.1    | <b>Microgrids</b> . . . . .                          | 22        |
| 1.1.2    | <b>Electrical vehicles chargers</b> . . . . .        | 23        |
| 1.2      | ON-BOARD CHARGER . . . . .                           | 25        |
| 1.3      | DAB DESIGN OPTIMIZATION METHOD . . . . .             | 26        |
| 1.4      | OBJECTIVES . . . . .                                 | 28        |
| 1.5      | WORK STRUCTURE . . . . .                             | 28        |
| <b>2</b> | <b>DUAL-ACTIVE BRIDGE CONVERTER REVIEW</b> . . . . . | <b>29</b> |
| 2.1      | CONVERTER OVERVIEW . . . . .                         | 29        |
| 2.2      | DAB MODULATION AND SWITCHING SEQUENCE . . . . .      | 30        |
| 2.2.1    | <b>Interval I</b> . . . . .                          | 31        |
| 2.2.2    | <b>Interval II</b> . . . . .                         | 32        |
| 2.2.3    | <b>Interval III</b> . . . . .                        | 33        |
| 2.2.4    | <b>Interval IV</b> . . . . .                         | 33        |
| 2.3      | INDUCTOR CURRENT AND POWER TRANSFER . . . . .        | 34        |
| 2.4      | CONCLUSION . . . . .                                 | 38        |
| <b>3</b> | <b>DAB DESIGN OPTIMIZATION</b> . . . . .             | <b>39</b> |
| 3.1      | PARTICLE SWARM OPTIMIZATION . . . . .                | 39        |
| 3.2      | PSO ALGORITHM . . . . .                              | 40        |
| 3.3      | DAB CONVERTER PARAMETERS DEFINITION . . . . .        | 43        |
| 3.3.1    | <b>Inductor</b> . . . . .                            | 43        |
| 3.3.2    | <b>Transformer</b> . . . . .                         | 43        |
| 3.4      | POWER LOSSES AND THERMAL MODELS . . . . .            | 44        |
| 3.4.1    | <b>Semiconductor losses</b> . . . . .                | 44        |

|         |   |    |
|---------|---|----|
| 3.4.2   | <b>Magnetic losses</b>                                  | 45 |
| 3.4.2.1 | Core losses   | 45 |
| 3.4.2.2 | Copper losses   | 47 |
| 3.4.3   | <b>Thermal Models</b>                                   | 48 |
| 3.4.3.1 | Semiconductors thermal models                           | 48 |
| 3.4.3.2 | Magnetic thermal models                                 | 49 |
| 3.4.4   | <b>Lookup table</b>                                     | 49 |
| 3.5     | CONCLUSION  | 49 |
| 4       | <b>OPTIMIZATION PROCESS</b>                             | 51 |
| 4.1     | OBJECTIVE OF THE CONVERTER OPTIMIZATION DESIGN          | 51 |
| 4.2     | PSO INITIALIZATION                                      | 51 |
| 4.3     | DAB OPTIMIZATION RESULTS                                | 53 |
| 4.3.1   | <b>Power switches losses results</b>                    | 53 |
| 4.3.2   | <b>Magnetics results</b>                                | 55 |
| 4.4     | DAB OPTIMIZATION RESULTS - VARIABLE FREQUENCY           | 58 |
| 4.4.1   | <b>Variable frequency optimization</b>                  | 58 |
| 4.4.2   | <b>Power switches losses variable frequency results</b> | 59 |
| 4.4.3   | <b>Magnetics results - Variable Frequency</b>           | 60 |
| 4.4.4   | <b>Variable frequency x Fixed frequency comparison</b>  | 63 |
| 4.5     | CONCLUSION  | 68 |
| 5       | <b>DAB CONVERTER PROTOTYPE</b>                          | 69 |
| 5.1     | PROTOTYPE CONSTRUCTION                                  | 69 |
| 5.2     | MAGNETICS DESIGN  | 69 |
| 5.2.1   | <b>Inductor Design</b>                                  | 70 |
| 5.2.2   | <b>Transformer Design</b>                               | 70 |
| 5.3     | TRANSISTORS   | 74 |
| 5.4     | EXPERIMENTAL RESULTS                                    | 74 |
| 5.4.1   | <b>DAB test setup</b>                                   | 75 |
| 5.4.2   | <b>Efficiency Comparison</b>                            | 76 |
| 5.4.2.1 | Experimental results - 300 V                            | 76 |
| 5.4.2.2 | Experimental results - 350 V                            | 80 |
| 5.4.2.3 | Experimental results - 400 V                            | 83 |
| 5.4.2.4 | Experimental results - 450 V                            | 85 |
| 5.5     | CONCLUSION  | 88 |
| 6       | <b>CONCLUSION</b>                                       | 90 |
| 6.1     | FUTURE WORKS  | 91 |

|                     |                                |           |
|---------------------|--------------------------------|-----------|
| <b>BIBLIOGRAPHY</b> | <b>92</b>                      |           |
| <b>APPENDIX A</b>   | <b>DAB CONVERTER PROTOTYPE</b> | <b>97</b> |
| A.1                 | CAPACITORS                     | 97        |
| A.2                 | DAB SCHEMATICS                 | 97        |
| A.3                 | DAB LAYOUT                     | 101       |

---

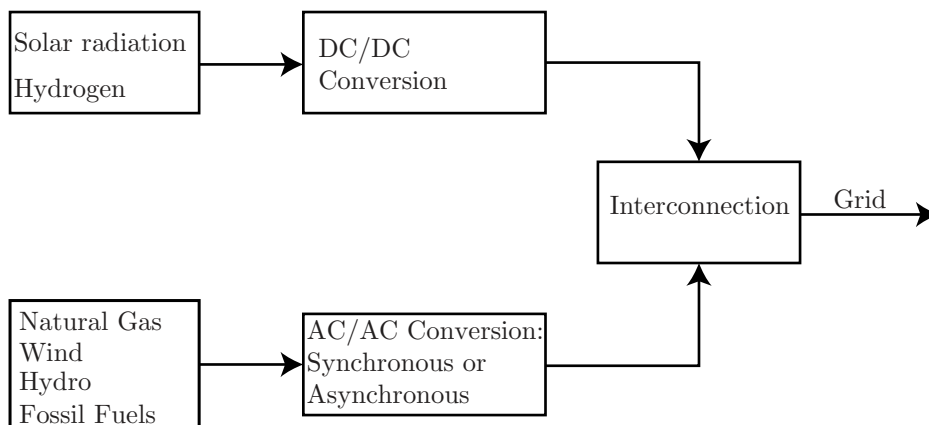
## Introduction

The contemporary global focus on reducing CO<sub>2</sub> emissions has driven the widespread adoption of electric vehicles (EVs) as a sustainable mode of transportation. However, the limited operational range of current lithium-ion batteries presents a significant challenge to vehicular autonomy. This challenge underscores the urgent need for substantial advancements in battery technology and charging infrastructure, as discussed in previous studies [1].

Moreover, the increasing prevalence of EVs has placed considerable strain on residential electric grids, primarily due to the rising demand for EV charging facilities. This strain has been extensively examined and highlighted in the existing literature [2, 3].

Addressing this growing demand requires a strategic approach focused on generating more sustainable energy and optimizing its distribution for efficiency. This imperative is a central theme in scholarly discussions [4]. Consequently, there is a notable trend towards exploring various distributed energy resources to complement traditional power stations. Figure 1.1 provides an illustrative depiction of this trend, supported by scholarly investigations [5, 6].

**Figure 1.1** – Several energy sources grid.

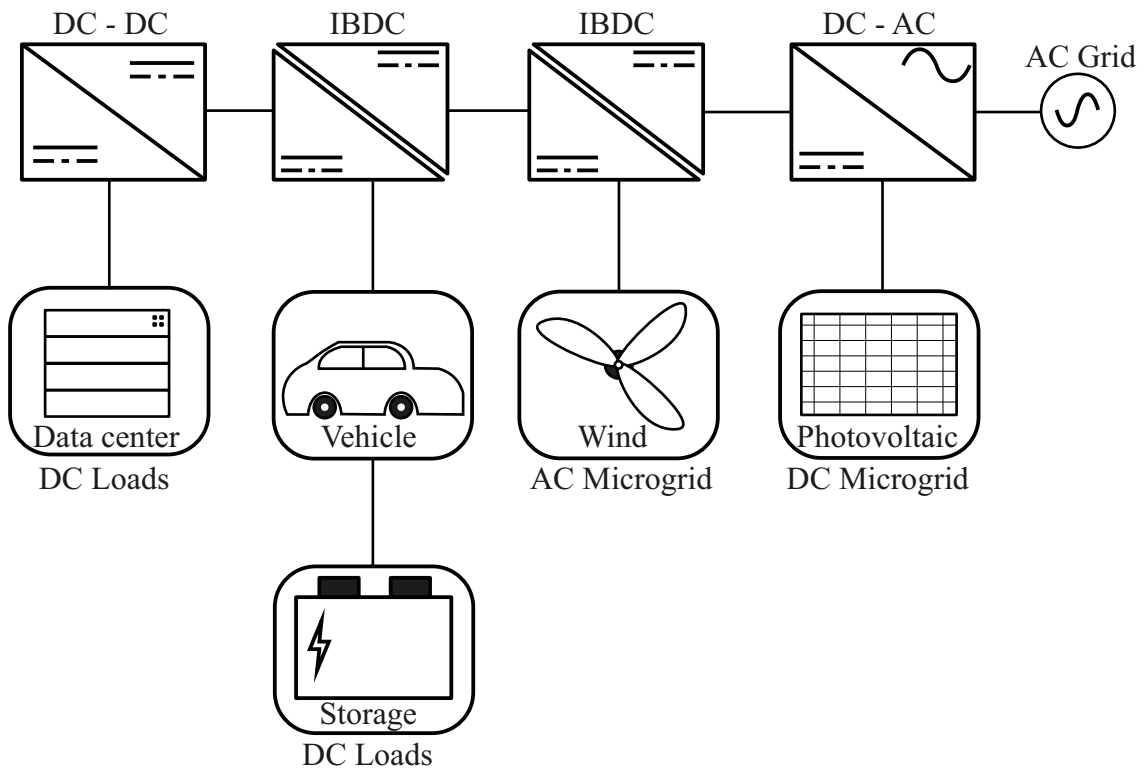


Note. Own authorship, based on [6].

## 1.1 ISOLATED BIDIRECTIONAL DC-DC CONVERTER

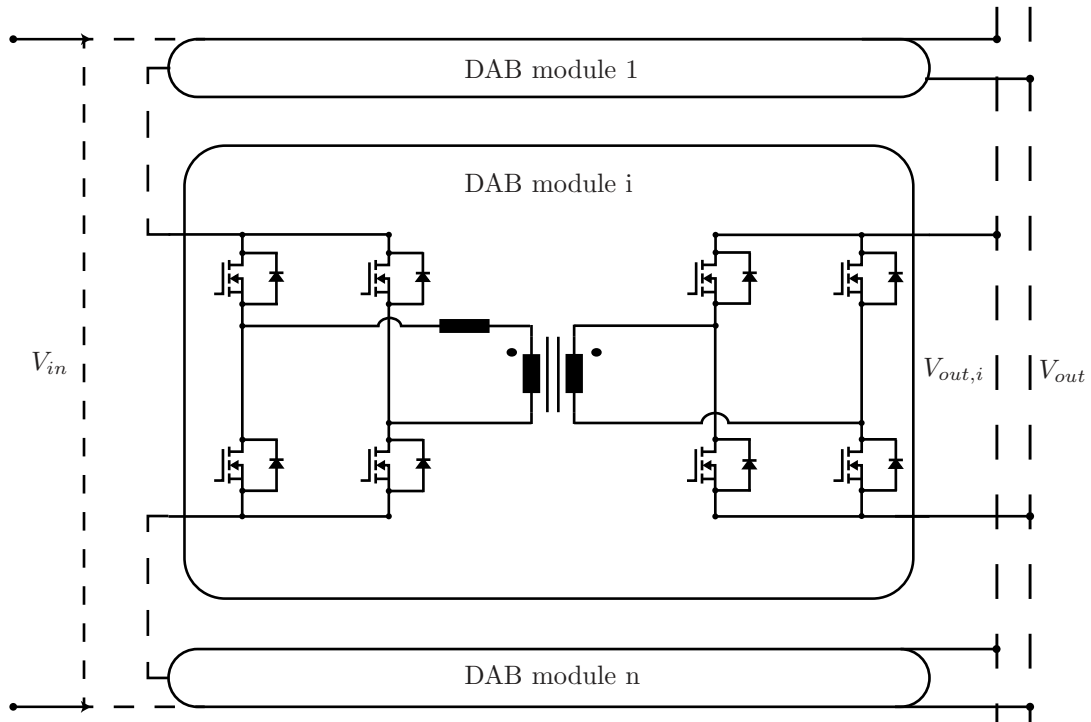
An solution to the multifaceted challenges of the isolated bidirectional DC-DC converter (IBDC). Render it an apt choice for a spectrum of applications such as bus connections, voltage conversion, power transmission, and electrical isolation within DC distribution networks [7]. Within the context of a medium-voltage DC power distribution system, the IBDC can function as a DC transformer [8] or as a solid-state transformer [9, 10]. The versatile utility of the IBDC is exemplified in Figure 1.2, showcasing its diverse applications within the electrical grid.

**Figure 1.2** – IBDC Application on electrical grid.



Note. Own authorship, based on [7].

The versatility of IBDCs extends voltage and power ratings of applications through the adoption of modular structures. These structures input-series-output-series [11], input-parallel-output-series [12], and input-series-output-parallel configurations [13]. Such modular designs not only afford redundant architectures but also facilitate flexible installation, thereby augmenting power transmission capabilities while mitigating reactive power and minimizing current stress. An illustrative example of this flexibility is depicted in Figure 1.3, showcasing an input-series-output-parallel structure based on a Dual-active-bridge module.

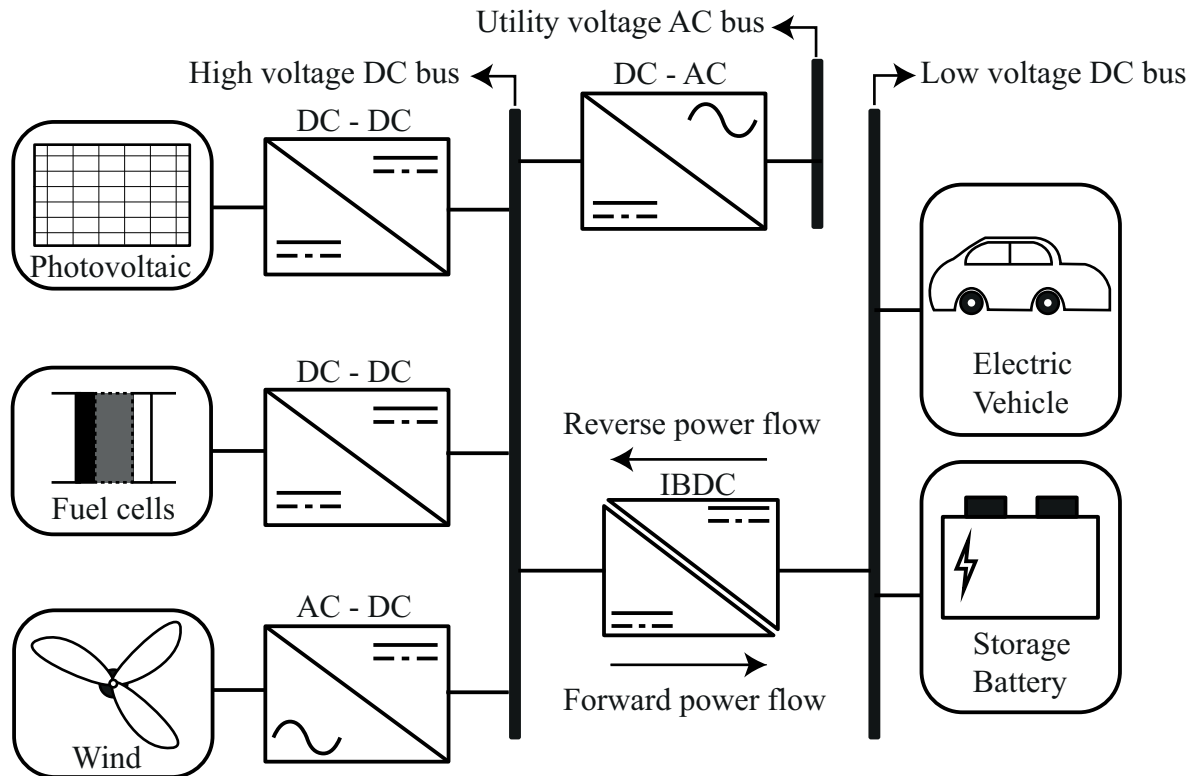
**Figure 1.3** – ISOP structure IBDC scheme based on DAB modules.

Note. Own authorship, based on [7].

### 1.1.1 Microgrids

Renewable energy sources like photovoltaic and wind power are increasingly integrated into microgrids as distributed energy resources. However, their intermittent nature necessitates strategies such as deploying energy storage systems (ESS) across the electrical grid, a measure that helps mitigate the reliability issues associated with these sources [14]. These systems aggregate various technologies, including lithium-ion batteries, supercapacitors, and electric vehicles utilized in Vehicle-to-Grid (V2G) applications [15].

Efficiently integrating these diverse systems into the grid and ensuring proper energy distribution necessitates the utilization of Isolated Bidirectional DC-DC Converters (IBDCs). These converters offer the advantage of system reconfiguration flexibility while adhering to stringent safety standards owing to their galvanic isolation properties. Figure 1.4 illustrates how IBDCs can serve as interfaces between high-voltage buses housing distributed energy resources and low-voltage buses containing energy storage devices within microgrids.

**Figure 1.4** – Microgrid IBCD application.

Note. Own authorship, based on [15].

### 1.1.2 Electrical vehicles chargers

IBDCs find another compelling application in electric vehicle (EV) chargers. With the ongoing proliferation of electric vehicles, the imperative to advance charging technologies becomes increasingly apparent for a seamless transition to EVs in the future. Presently, EV chargers are categorized into distinct levels as per global standards [16]:

- Level-1 (AC):
  - Charger Location: On-board (Residential charging);
  - Power Supply: 120/230  $V_{ac}$  - 12 A to 16 A (Single Phase);
  - Charger Power Level: From 1.44 kW to 1.92 kW;
  - Protection Type: Breaker in cable;
  - Charging time: 11-36 hours for EVs (16-50 kWh ).
- Level-2 (AC):
  - Charger Location: On-board (Charging at home or workplace);
  - Power Supply: 208/240  $V_{ac}$  - 15 A to 80 A (Single/split Phase);
  - Charger Power Level: From 3.1 kW to 19.2 kW;
  - Protection Type: Pilot function breaker in cable;



- Charging time: 2-6 hours for EVs (16-30 kWh).
- Level-3 (*DC Fast*):
  - Charger Location: Off-board (Charging at public places similar to gas stations);
  - Power Supply: 300/600  $V_{dc}$  - (Maximum current 400 A) (Three Phase);
  - Charger Power Level: From 50 kW to 350 kW;
  - Protection Type: Monitoring and communication between charging station and EV;
  - Charging time: Less than 30 minutes for EVs (20-50 kWh).
- Next generation, DC Ultra-Fast Charging:
  - Charger Location: Off-board (Charging at public places similar to gas stations);
  - Power Supply: 800  $V_{dc}$  and higher - 400 A and higher (Polyphase Phase);
  - Charger Power Level: From 400 kW and higher;
  - Protection Type: Monitoring and communication between charging station and EV, liquid cooling;
  - Charging time: Approximately 10 minutes for EVs (20-50 kWh).

As shown above, the vehicle charging process can be either AC or DC. Levels 1 and 2 represent AC charging for on-board chargers and are slower, while Level 3 DC charging is considerably faster but is only available off-board. Level 1 charging is typically installed in residential buildings for use during the night. Level 2 charging is commonly found in commercial locations such as malls and offices. Level 3 chargers are usually located at specified locations due to the high power flow, similar to a gas station setup.

In the case of DC ultra-fast charging, the technology aims to solve the charging time problem, drastically reducing the time for a full battery recharge from hours to minutes, almost as fast as refueling a gas tank. However, the technologies necessary to make this possible are still under research and development, such as batteries that can handle overheating during the charging process and the standardization of charging systems between vehicles [17].

However, current Level 3 chargers are still capable of supplying commercially available EVs, as indicated in Table 1.1 [18]. Most available vehicles can be fully charged in under 10 hours with a Level 2 charger. Many of the specifications for DC ultra-fast charging are considered future-proof, as they overdimension many current specifications.

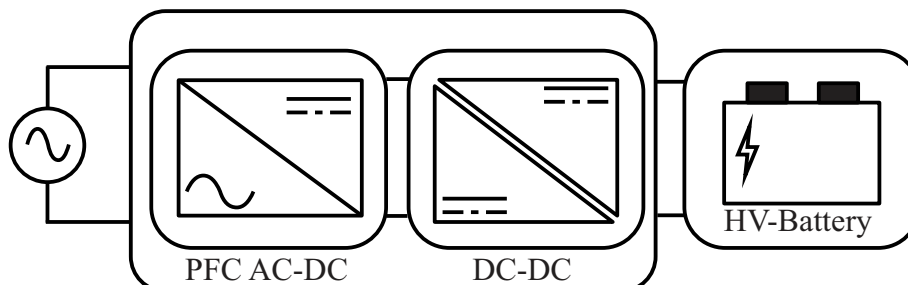
**Table 1.1** – Charging specifications of some available EVs.

| Model             | Battery Voltage | Rated Energy (Usable) | Onboard Charging Power (Time)  | Max. Charging Power (Time) |
|-------------------|-----------------|-----------------------|--------------------------------|----------------------------|
| eCitaro (bus)     | 400 V           | 182 kWh               | N/A                            | 300 kW (29 min)            |
| 7900 Elec. (bus)  | 600 V           | 150 kWh               | 11 kW (10.9 h)                 | 300 kW (24 min)            |
| Model S           | 400 V           | 100 kWh               | 11.5 kW (10.25 h)              | 250 kW (38 min)            |
| E-tron 55 Quattro | 396 V           | 95 kWh                | 11 kW (10.5 h)                 | 150 kW (26 min)            |
| EQC 400 4Matic    | 405 V           | 85 kWh                | 7.4 kW (10.5 h)                | 150 kW (31 min)            |
| Taycan 4S         | 800 V           | 79.2 kWh              | 11 kW (9 h);<br>9.6 kW (9.5 h) | 270 kW (21 min)            |
| Model 3           | 360 V           | 75 kWh                | 11.5 kW (7.75 h)               | 250 kW (22 min)            |
| Polestar 2        | 450 V           | 75 kWh                | 11 kW (7.75 h)                 | 150 kW (31 min)            |
| Bolt              | 350 V           | 62.2 kWh              | 7.4 kW (8.3 h)                 | 50 kW (60 min)             |
| Leaf 3+           | 360 V           | 62 kWh                | 6.6 kW (11.5 h)                | 100 kW (35 min)            |
| Zoe ZE50          | 400 V           | 54.7 kWh              | 22 kW (3 h)                    | 50 kW (56 min)             |
| Ioniq             | 320 V           | 40.4 kWh              | 7.2 kW (6.25 h)                | 100 kW (20.6 min)          |
| Leaf              | 360 V           | 40 kWh                | 6.6 kW (6.5 h)                 | 50 kW (40 min)             |

Note. Own authorship, based on [16].

## 1.2 ON-BOARD CHARGER

The on-board charger (OBC) enables direct battery recharging from the grid. While traditional OBCs support unidirectional power flow, bidirectional OBCs offer greater flexibility, allowing EVs to be utilized for applications such as vehicle-to-grid (V2G), vehicle-to-home (V2H), or vehicle-to-load (V2L) systems during idle periods [19].

**Figure 1.5** – On-board charger.

Note. Own authorship, based on [19].

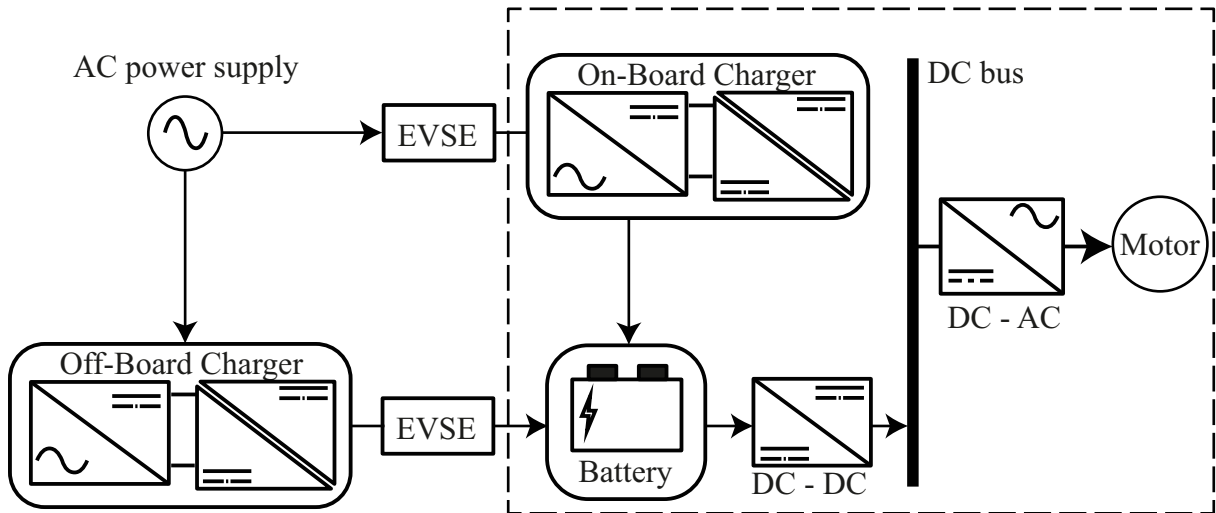
On-board chargers commonly consist of two conversion stages: power factor correction (PFC) and DC-DC conversion, as illustrated in Figure 1.5 [20].

The present study focuses specifically on the DC-DC stage, aiming to investigate the implementation and optimization of a DAB converter for integration into an on-board

charger (OBC).

The schematic of the EV charging system is displayed in Figure 1.6, where the AC power supply can be connected directly to the electric vehicle supply equipment (EVSE) in the case of an on-board charger. In the case of an off-board charger, the vehicle's EVSE only connects to the off-board charger, which then connects to the AC power supply to charge the vehicle.

**Figure 1.6** – EV charging system on-board/off-board charger.



Note. Own authorship, based on [16].

### 1.3 DAB DESIGN OPTIMIZATION METHOD

As elucidated in previous sections, IBDCs exhibit a wide spectrum of applications, ranging from power generation to power distribution and tailored power converter design for specific applications. Achieving optimal results in these domains entails leveraging computational methodologies to evaluate converter requirements' impacts on specifications and optimize key parameters, such as weight limitations or power losses [21].

One such computational approach involves employing optimization algorithms like the particle swarm optimization (PSO). This algorithm functions by iteratively enhancing swarms of particles within an optimization-defined search space, akin to simulating bird behavior. Beginning with a random solution, PSO evolves iteratively by improving its fitness function towards the optimal solution [22]. Figure 1.7 illustrates the foundational structure of the PSO optimization process.

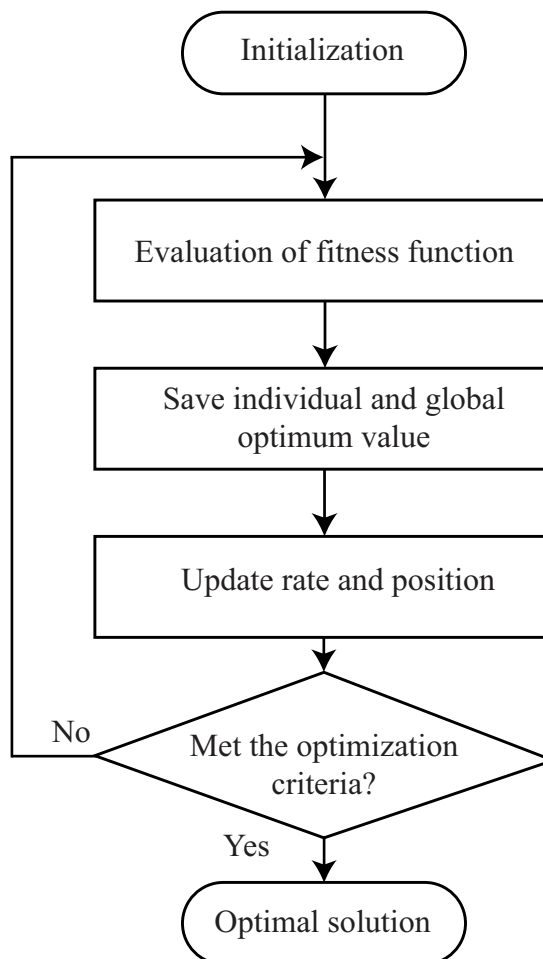
The utilization of PSO within the realm of IBDCs holds immense promise, particularly in optimizing converter specifications for various applications. By iteratively refining particle movements based on fitness functions, PSO can effectively navigate complex parameter spaces, enabling the identification of optimal solutions that meet desired performance criteria while considering constraints such as weight limitations or power losses. This iterative refinement process mimics the evolutionary strategies observed

in natural systems, contributing to its efficacy in solving optimization problems efficiently.

Furthermore, PSO's ability to handle multi-objective optimization makes it particularly suitable for addressing diverse and conflicting objectives in IBDC design. For instance, in power generation applications, optimizing for both efficiency and reliability can be achieved through PSO's capacity to balance trade-offs and converge on Pareto-optimal solutions. This versatility positions PSO as a valuable tool in the design and optimization of IBDCs across various domains, enhancing their performance, efficiency, and overall effectiveness in modern power systems.

In essence, the integration of computational optimization techniques like PSO into IBDC design processes represents a significant advancement, enabling the navigation of complex design spaces effectively and derive optimal solutions that meet stringent performance criteria while considering practical constraints. This approach not only enhances the functionality and efficiency of IBDCs but also contributes to advancing the broader field of power electronics and renewable energy systems towards sustainable and resilient infrastructure solutions.

**Figure 1.7** – Basic structure of the particle swarm optimization.



Note. Own authorship, based on [22].

## 1.4 OBJECTIVES

The main objective is to design a Dual-active-bridge (DAB) converter using algorithm optimization, with a focus on its application in on-board chargers. The specific objectives are:

- Analyse the performance of the DAB converter designed under the method of algorithm optimization;
- Optimize the converter under different conditions, while maintaining sets of components and verify if there is any significant difference on the optimization results.

## 1.5 WORK STRUCTURE

The present work is organized on five chapters and an appendice, they focus on the following:

- Chapter 1 consists of an analysis of a IBDCs converters and their diverse applications, together with an brief introduction on optimization algorithm and electrical vehicles chargers and its categories;
- Chapter 2 introduces the Dual-Active-Bridge converter, categorized as an IBDC. The chapter provides a comprehensive overview of the converter, delving into its capabilities, operational mechanisms, modulation techniques, and switching sequences. It navigates through the converter's operation intervals, elucidating the intricate details of current waveforms and presenting pertinent equations essential for the study at hand;
- Chapter 3 introduces the the optimization algorithm for the DAB converter, the equations and methodology used for the optimization of the main components;
- Chapter 4 describes each of the parameters utilized on the optimization process and material of choice for said parameters along with the theoretical results for the study;
- Chapter 5, the focus shifts to the DAB converter prototype, highlighting the experimental outcomes concerning the theoretical results obtained through the optimization algorithm. This chapter meticulously examines the efficacy and efficiency of the optimization methodology, offering a comprehensive analysis of the experimental data vis-à-vis the anticipated theoretical outcomes.
- Appendice A further expands on the converter prototype constructed.

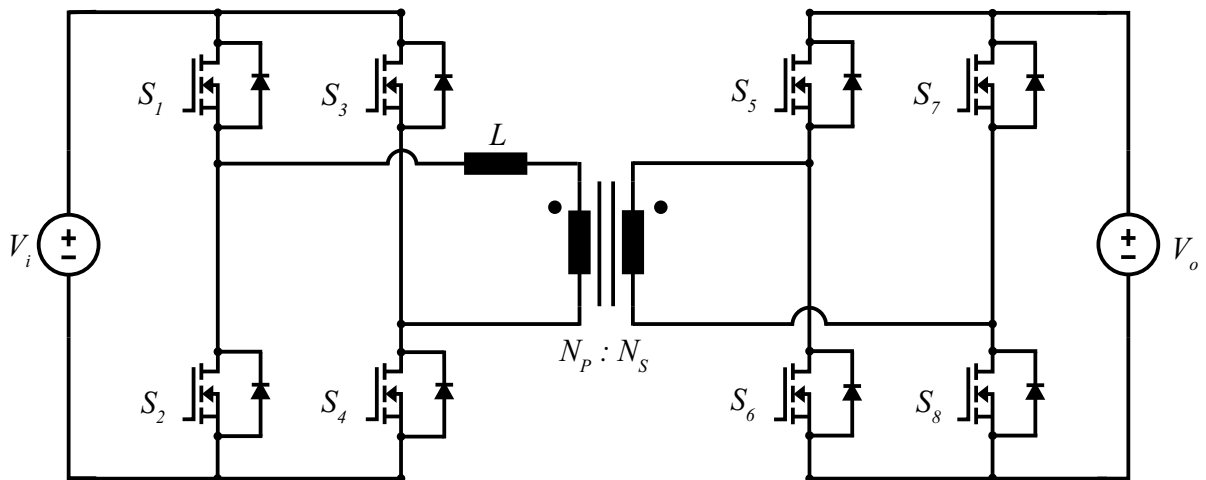
## Dual-Active Bridge Converter Review

The main objective of this chapter, is to present the Dual-Active-Bridge (DAB) converter, the modulation technique and the switching sequence employed in this work, the intervals of operation with equations of interest and zero voltage switching (ZVS) conditions.

### 2.1 CONVERTER OVERVIEW

The DAB converter, presented in Figure 2.1, is a bidirectional converter characterized by a symmetrical structure that facilitates power transfer between its two bridges. Its selection for this specific application stems from a myriad of advantageous features. These include a low component count, operation with zero voltage switching (ZVS), high flexibility with modulation schemes, and a modular structure, as noted in sources such as [23] and [24].

**Figure 2.1** – Dual Active Bridge (DAB) converter.



Note. Own authorship.

This topology represents a high-power, high-density, and high-efficiency converter

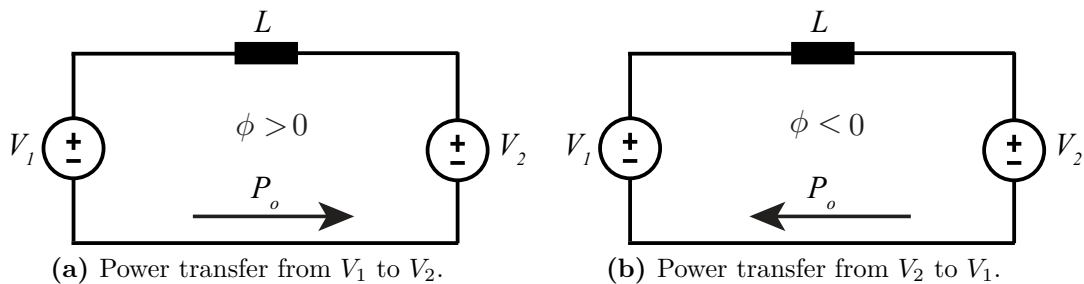
characterized by minimal switching losses. It boasts the capability of operating in both buck and boost modes while facilitating bidirectional power flow, as detailed in sources such as [25] and [26].

The power flow control within the DAB converter can be achieved through various methods. These include manipulating the phase shift angle ( $\phi$ ) between the primary and secondary sides of the converter, modulating the duty cycle, or adjusting the switching frequency, as discussed in [27]. Among these approaches, adjusting the phase shift angle emerges as the most prevalent and practical. For the specific focus of this work, a single phase shift with a variable frequency is selected as the method for controlling power transfer.

## 2.2 DAB MODULATION AND SWITCHING SEQUENCE

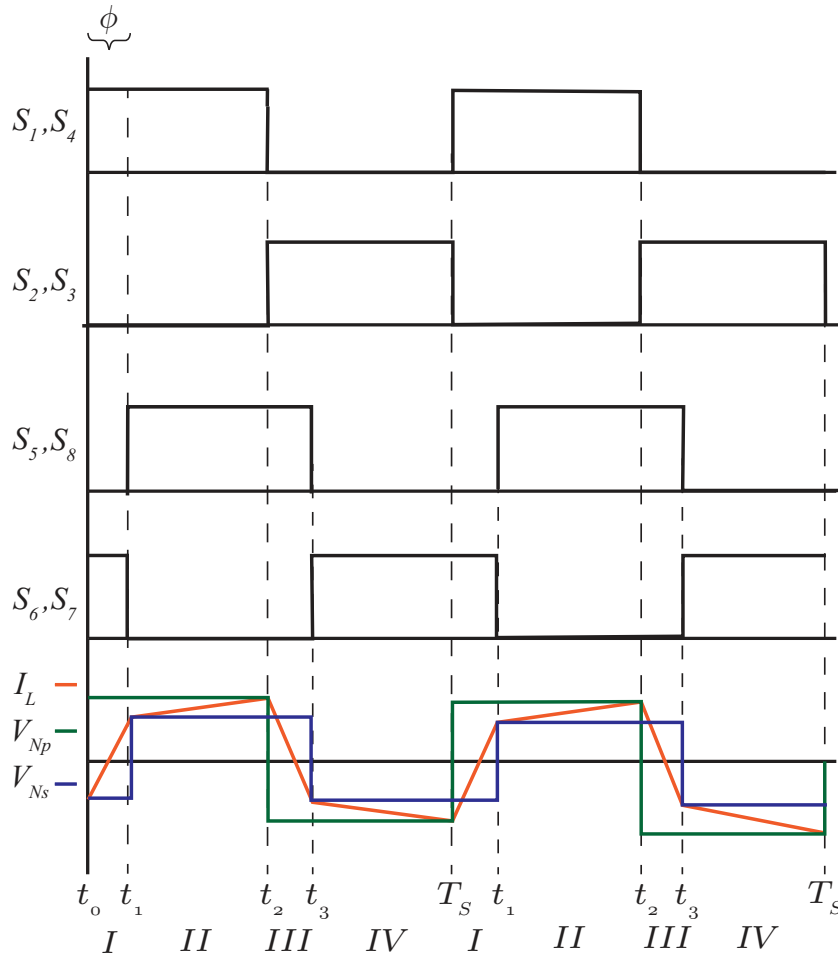
For a DAB converter, single-phase shift (SPS) modulation emerges as a fundamental control strategy, as discussed in [28]. In this operational mode, each pair of switches maintains a 50% duty cycle, while both bridges exhibit a defined phase shift denoted by the phase shift angle. Consequently, one bridge leads while the other lags, facilitating power transfer from the leading bridge to the lagging one. By adjusting the phase shift angle  $\phi$ , either within the range of  $0 < \phi$ , or  $\phi > 0$ , the direction of power flow within the DAB converter can be effectively established, as illustrated in Figure 2.2.

**Figure 2.2** – Power transfer scheme (a) where the  $\phi$  angle is higher than 0 and the power flows from  $V_1$  to  $V_2$ , and (b) where the  $\phi$  angle is lower than 0 and the power flows from  $V_2$  to  $V_1$ .



Note. Own authorship.

The switching sequence of the DAB converter is delineated into four distinct intervals, a segmentation based on the inductor waveform dynamics and the phase shift observed between the primary and secondary of the transformer. This operational delineation is visually depicted in Figure 2.3, showcasing the intricate waveforms and operational states of the converter under single-phase shift (SPS) modulation, as documented in [23].

**Figure 2.3** – DAB Single phase shift modulation.

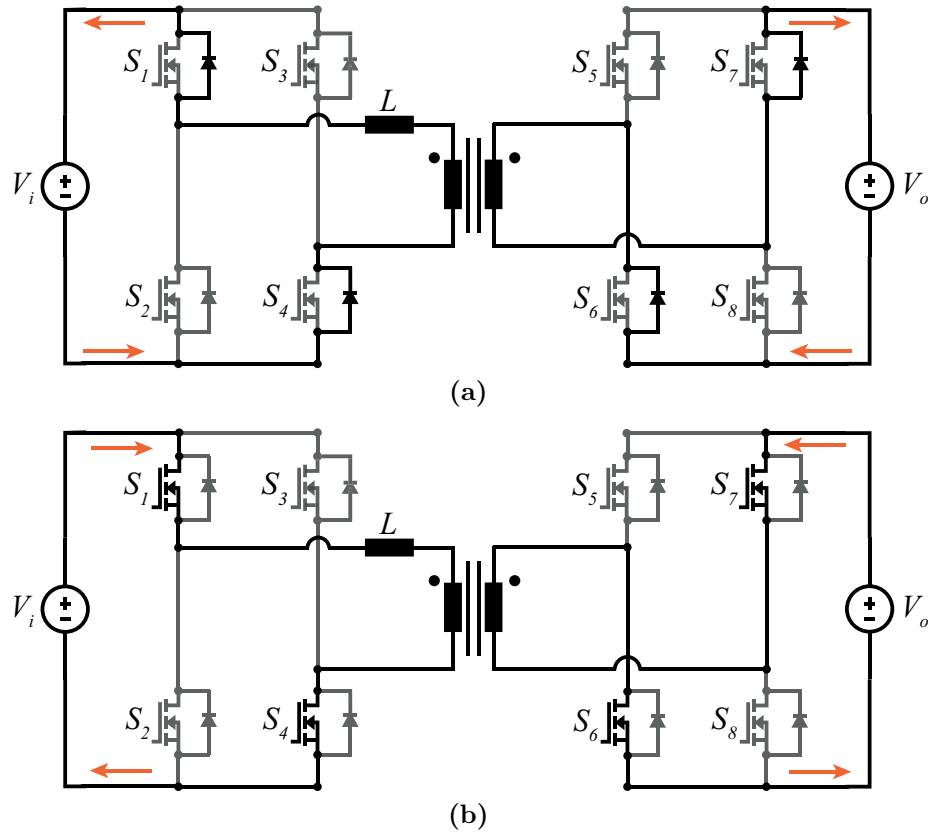
Note. Own authorship.

### 2.2.1 Interval I

During the initial switching interval of converter operation, the current waveform within the inductor exhibits both negative and positive phases. At this juncture, switches  $S_1$  and  $S_4$  on the primary side, along with switches  $S_6$  and  $S_7$  on the secondary side, are responsible for conducting current. As a result, the current flow during this interval manifests as depicted in Figure 2.4, where it can be delineated into two distinct phases.

In the initial phase, portrayed in Figure 2.4a, the inductor's current assumes a negative polarity and traverses through the body diodes of the switches until these diodes block the current. This transition marks the commencement of the subsequent phase within the first operation interval. Here, as illustrated in Figure 2.4b, the inductor's current switches to a positive polarity and directly flows through the switches until the conclusion of the initial interval.

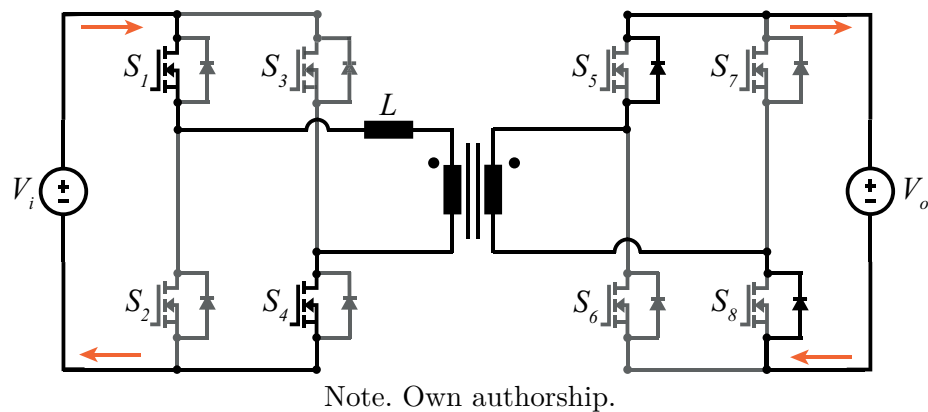


**Figure 2.4** – DAB interval I: Negative inductor current(a); Positive inductor current(b).

Note. Own authorship.

### 2.2.2 Interval II

In the second operational interval, as depicted in Figure 2.5, switches  $S_1$  and  $S_4$  continue to conduct current on the primary side, while on the secondary side, current begins to flow through the body diodes of switches  $S_5$  and  $S_8$ , maintaining a positive polarity throughout the entire interval.

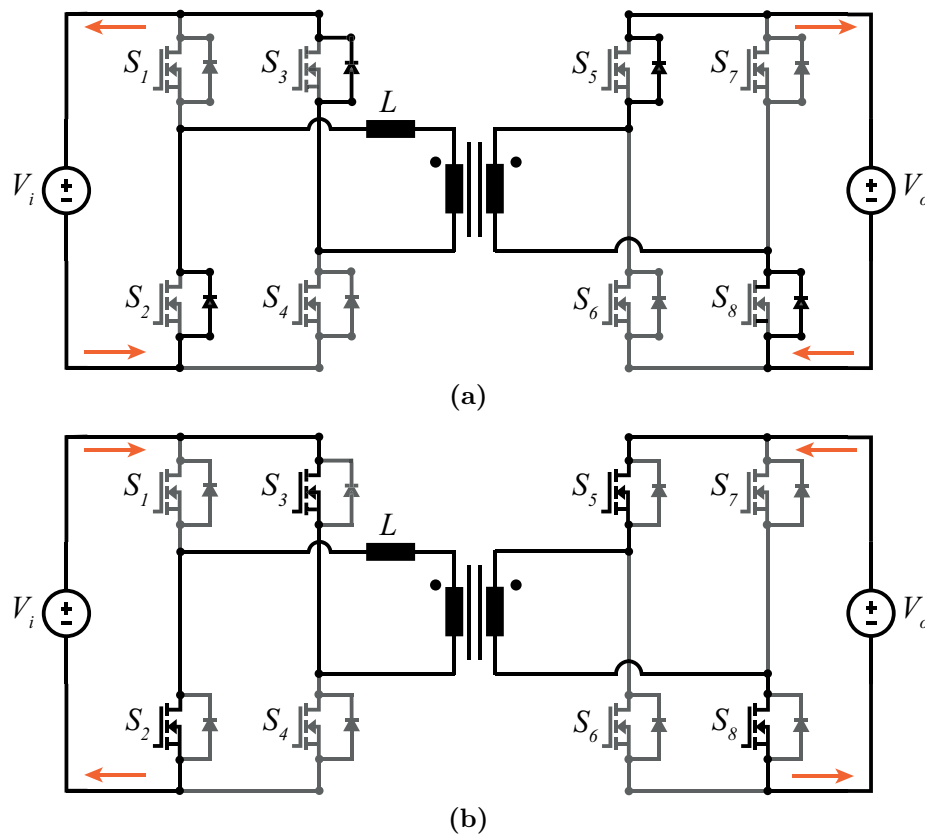
**Figure 2.5** – DAB interval II.

### 2.2.3 Interval III

Moving on to the third operational interval, a similar pattern to the first interval emerges, albeit with switches  $S_2$  and  $S_3$  conducting current on the primary side, and switches  $S_5$  and  $S_8$  on the secondary side, as shown in Figure 2.6. The inductor's current waveform once again transitions between negative and positive phases, but with a noteworthy distinction: the initial phase commences with a positive current and concludes with a negative current, as illustrated in Figure 2.6.

During the initial phase within this interval, depicted in Figure 2.6a, current solely flows through the body diodes of the switches. Subsequently, as these body diodes begin to block the current, the flow redirects through the switches themselves, as demonstrated in Figure 2.6b.

**Figure 2.6** – DAB interval III: Positive inductor current(a); Negative inductor current(b).

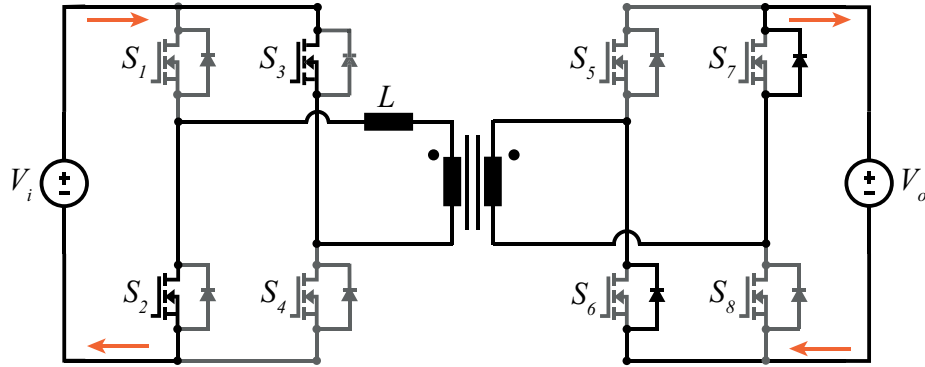


Note. Own authorship.

### 2.2.4 Interval IV

In the fourth operational interval, as illustrated in Figure 2.7, a resemblance to the second interval is noted, albeit with switches  $S_2$  and  $S_3$  conducting current on the primary side, while switches  $S_6$  and  $S_7$  on the secondary side operate via their body diodes. Notably, the current within the inductor maintains a negative polarity throughout the entire duration of this interval.

Figure 2.7 – DAB interval IV.

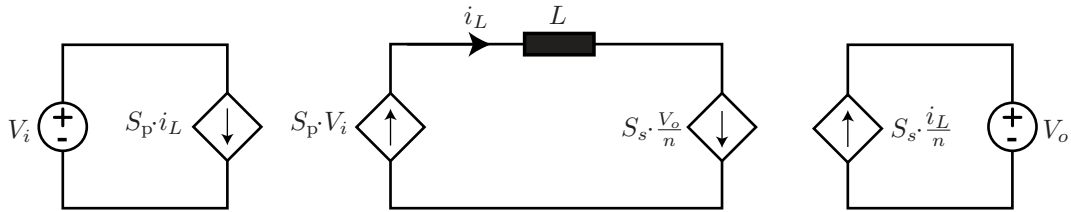


Note. Own authorship.

### 2.3 INDUCTOR CURRENT AND POWER TRANSFER

The model simplification of the DAB converter, presented in Figure 2.8, categorizes the power switches on both the primary and secondary sides into two states. Specifically, on the primary side, if switches  $S_1$  and  $S_4$  are activated, the variable  $S_p$  assumes a value of 1; conversely, when switches  $S_2$  and  $S_3$  are activated,  $S_p$  becomes -1. Similarly, on the secondary side, activation of switches  $S_6$  and  $S_7$  leads to  $S_s$  being -1, while activation of switches  $S_5$  and  $S_8$  sets  $S_s$  to 1.

Figure 2.8 – Simplified DAB Model.



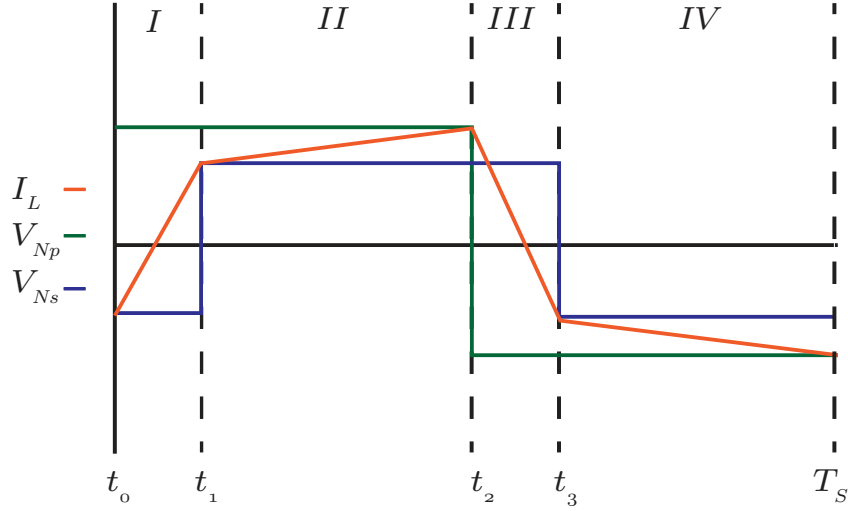
Note. Own authorship.

Under single-phase shift modulation, the voltage levels across the primary ( $V_{Np}$ ) and secondary ( $V_{Ns}$ ) sides, alongside the inductor current, exhibit characteristics as illustrated in Figure 2.9. The states of  $S_p$  and  $S_s$  are comprehensively detailed in Table 2.1.

Table 2.1 – Switching states.

| Switches | Intervals |    |     |    |
|----------|-----------|----|-----|----|
|          | I         | II | III | IV |
| $S_p$    | 1         | 1  | -1  | -1 |
| $S_s$    | -1        | 1  | 1   | -1 |

Note. Own authorship.

**Figure 2.9** – Transformer voltage and inductor current.

Note. Own authorship.

Within the first interval (I), the switches  $S_p$  and  $S_s$  assume states of 1 and -1, respectively. Consequently, the voltage level across the primary is positive, while across the secondary, it is negative. Furthermore, at the onset of this period, the inductor's current denoted as  $i_{L,t_1}$  is equivalent to  $-i_{L,t_2}$  owing to the half-cycle symmetry inherent in the converter. Subsequently, the current rises along a defined slope until reaching the conclusion of this interval, where the inductor's current can be precisely characterized as:

$$i_{L(t_1)} = i_{L(t_0)} + \frac{t_1}{L} \left( V_i + \frac{V_o}{n} \right), \quad (2.1)$$

the period of  $t_1$  can be given as,

$$t_1 = \frac{\phi}{2\pi f_s}, \quad (2.2)$$

the value for  $i_{L(t_0)}$  is given by the equation 2.10, resulting in the equation,

$$i_{L(t_1)} = \frac{\pi(V_o - nV_i\pi) - 2V_o\phi}{4L\pi f_s n}, \quad (2.3)$$

for the inductor's current  $i_{L,t_1}$  which is the initial value for the second interval of operation.

During the second (II) operational interval, switches  $S_p$  and  $S_s$  assume states of 1 and 1, respectively. Consequently, both the primary and secondary voltage levels are positive throughout this period. The upward slope of the current comes to a halt as this interval concludes, reaching its peak at  $t_2$ , at which point it can be accurately defined as:

$$i_{L(t_2)} = i_{L(t_1)} + \frac{t_2 - t_1}{L} \left( V_i - \frac{V_o}{n} \right), \quad (2.4)$$

in the equation 2.4 the period of  $t_2$  can be given as,

$$t_2 = \frac{1}{2f_s}, \quad (2.5)$$

and the resulting equation being:

$$i_{L(t_2)} = \frac{\pi(V_o - nV_i\pi) + 2nV_i\phi}{4L\pi f_s n}, \quad (2.6)$$

ending the second interval and the first half of converter's operation cycle.

In the latter half of the operational cycle, spanning intervals III and IV, the equations will demonstrate a notable similarity, although with inverted signals in comparison to intervals I and II.

Within the third interval (III), switches  $S_p$  and  $S_s$  adopt states of -1 and 1, respectively. Consequently, the voltage level across the primary is negative, while across the secondary, it is positive. The slope of the inductor's current during this interval mirrors that of the first interval but in an inverted manner. At the conclusion of this interval, the current can be defined by the equation:

$$i_{L(t_3)} = i_{L(t_2)} + \frac{t_3 - t_2}{L} \left( -V_i - \frac{V_o}{n} \right), \quad (2.7)$$

the period of  $t_3$  can be given as,

$$t_3 = \frac{\left( \frac{\phi}{2\pi} + \frac{1}{2} \right)}{f_s}, \quad (2.8)$$

resulting in,

$$i_{L(t_3)} = \frac{\pi(nV_i - V_o) + 2V_o\phi}{4L\pi f_s n}, \quad (2.9)$$

initializing the fourth and final interval of operation.

During the fourth interval (IV), the complete operational cycle of the converter comes to a conclusion. In this phase, switches  $S_p$  and  $S_s$  assume states of -1 and -1, respectively, resulting in negative voltage levels across both the primary and secondary. The slope of the inductor's current within this interval closely resembles that of the second interval, ultimately reaching its initial value of  $t_0$  by the interval's conclusion, as delineated in the equation:

$$i_{L(T_s)} = i_{L(t_0)} = i_{L(t_3)} + \frac{T_s - t_3}{L} \left( V_i - \frac{V_o}{n} \right), \quad (2.10)$$

where in the equation 2.10 the period of  $T_s$  can be given as,

$$T_s = t_0 = 1/f_s \quad (2.11)$$

resulting in the equation:

$$i_{L(Ts)} = \frac{\pi(V_o + nV_i) - 2nV_i\phi}{4L\pi f_s n}, \quad (2.12)$$

To calculate the power output ( $P_o$ ) of this converter, the average of the inductor's current across the first two intervals is taken, a step facilitated by the half-cycle symmetry inherent in the DAB converter. Multiplying this average by  $V_o$  yields the equation for  $P_o$ .

$$i_{Avg} = \frac{1}{n} \left( 2f_s \left( \int_{t_0}^{t_1} \left( i_{L(t_0)} + \frac{i_{L(t_1)} - i_{L(t_0)}}{t_1 - t_0} t \right) dt + \int_{t_1}^{t_2} \left( i_{L(t_1)} + \frac{i_{L(t_2)} - i_{L(t_1)}}{t_2 - t_1} t \right) dt \right) \right), \quad (2.13)$$

$$i_{Avg} = \frac{Vi\phi(\phi - \pi)}{2Lf_s n \pi^2}, \quad (2.14)$$

resulting in the equation,

$$P_o = \frac{V_i V_o \phi(\phi - \pi)}{2Lf_s n \pi^2}, \quad (2.15)$$

where the phase shift angle ( $\phi$ ) can be defined as,

$$\phi = \frac{\pi \left( V_i V_o - 2\sqrt{\frac{V_i V_o (V_i V_o - 8LP_o \cdot f_s \cdot n)}{4}} \right)}{2V_i V_o}. \quad (2.16)$$

Along with SPS modulation on the DAB converter, it is possible to achieve ZVS on the switches turn-on, depending on the polarity of the inductor's current ( $i_L$ ), as seen in [29]:

$$ZVS = \begin{cases} S_1, S_4, S_6, S_7 & = i_L < 0 \\ S_2, S_3, S_5, S_8 & = i_L > 0 \end{cases} \quad (2.17)$$

If the current of a switch is negative while being activated, Zero Voltage Switching (ZVS) will occur. The ZVS range for each phase shift can be acquired by the equations

$$\begin{cases} \phi_{ZVS, pri} > \frac{(1-d)\pi}{2} \\ \phi_{ZVS, sec} > \frac{(1-d)\pi}{2} \end{cases} \quad (2.18)$$

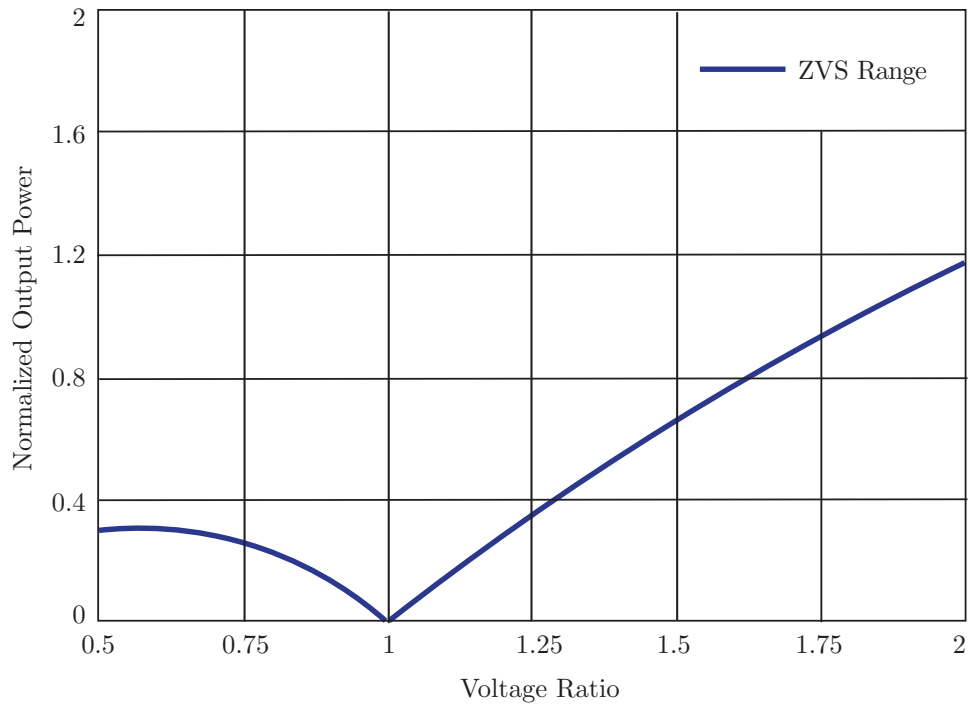
where when the phase shift  $\phi$  condition is true, ZVS is achieved at each side of the converter, the voltage ratio  $d$  is defined by

$$d = n \cdot \frac{V_o}{V_i}. \quad (2.19)$$

Since the phase shift is proportional to the output power, the ZVS range can be plotted on an normalized output power over voltage ratio graph, as shown in Figure 2.10. The ZVS range can be further extended by applying different control schemes, such as

extended-phase shift, dual-phase shift, or triple-phase shift control [23].

**Figure 2.10** – ZVS range with normalized output power over voltage ratio.



Note. Own authorship.

## 2.4 CONCLUSION

This chapter focused into the DAB converter, specifically on the single phase shift modulation technique utilized in this study. It elucidates the chosen modulation approach, detailing the switching sequence and operational intervals.

The primary equations presented upon in this chapter are the inductor current across each operational interval, the power output ( $P_o$ ), and the definition of the phase shift angle ( $\phi$ ). Additionally, the conditions necessary for achieving Zero Voltage Switching (ZVS) are elaborated upon.

---

## DAB Design Optimization

This chapter presents the design methodology for the DAB converter, accompanied by an overview of the Particle Swarm Optimization (PSO), its evolution, and widespread applications across diverse domains. The chapter further delves into the implementation of PSO within the context of the present work, detailing relevant equations and emphasizing the focal points of the optimization process for the DAB converter.

### 3.1 PARTICLE SWARM OPTIMIZATION

Originating as a meta-heuristic optimization algorithm, Particle Swarm Optimization (PSO) draws inspiration from the collective movements observed in natural systems, such as bird flocks and fish schools. Its inception can be traced back to the seminal work of Kennedy and Eberhart in 1995 [30]. Initially conceptualized as a simulation of social behavior, PSO quickly evolved into a potent tool for optimizing non-linear functions. Early iterations of PSO integrated concepts like nearest neighbor velocity matching and introduced randomness to facilitate exploration within the solution space. Subsequent refinements streamlined the algorithm, eliminating redundant variables and its optimization prowess. The algorithm's adaptability was further demonstrated through its extension to handle multidimensional optimization problems by leveraging matrices instead of one-dimensional arrays [31].

The versatility of PSO is evidenced by its widespread application across various fields to solve complex optimization problems. Noteworthy applications span domains such as machine learning [32], dynamical systems [33], and environments characterized by noise and dynamism [34]. Within the realm of power electronics, PSO finds utility in optimizing power electronics circuits [35] and facilitating the optimal design of converters with specific objectives, be it minimizing power losses [36], reducing overall size [37], or optimizing operational costs [38].



### 3.2 PSO ALGORITHM

In pursuit of optimizing the DAB converter using PSO, several operation points denoted as  $i = N_{points}$  serve as focal points within the optimization process. Here, the objective is to leverage the PSO algorithm to identify the optimal parameter combinations for  $N_{points}$ , with the overarching goal of minimizing cumulative losses across all operation points.

The emphasis on minimizing losses across operation points directly translates to reduced load process losses. However, it's essential to note that increasing the number of points for optimization improves precision but also demands more computational time for calculations.

To enhance the efficacy of the optimization process, a modulation strategy facilitates precise adjustments to both the phase shift ( $\phi$ ) and the frequency ( $f_s$ ) of the converter. This modulation strategy is exemplified in the DAB single-phase shift power transfer equation:

$$P(\phi, f_s) = \frac{V_i \cdot V_o \cdot \phi \cdot (\phi - \pi)}{2\pi^2 \cdot f_s \cdot L \cdot n} \quad (3.1)$$

this approach attains a heightened degree of flexibility, thus augmenting the overall performance of the converter significantly.

It is imperative to underscore that the power transfer mechanism within the DAB converter aligns with the formulation delineated in Equation 3.1, exerting a direct influence on the converter's operational efficiency. To gauge the converter's efficacy, optimization will be conducted at both fixed and variable frequencies, allowing for a comprehensive comparison of results.

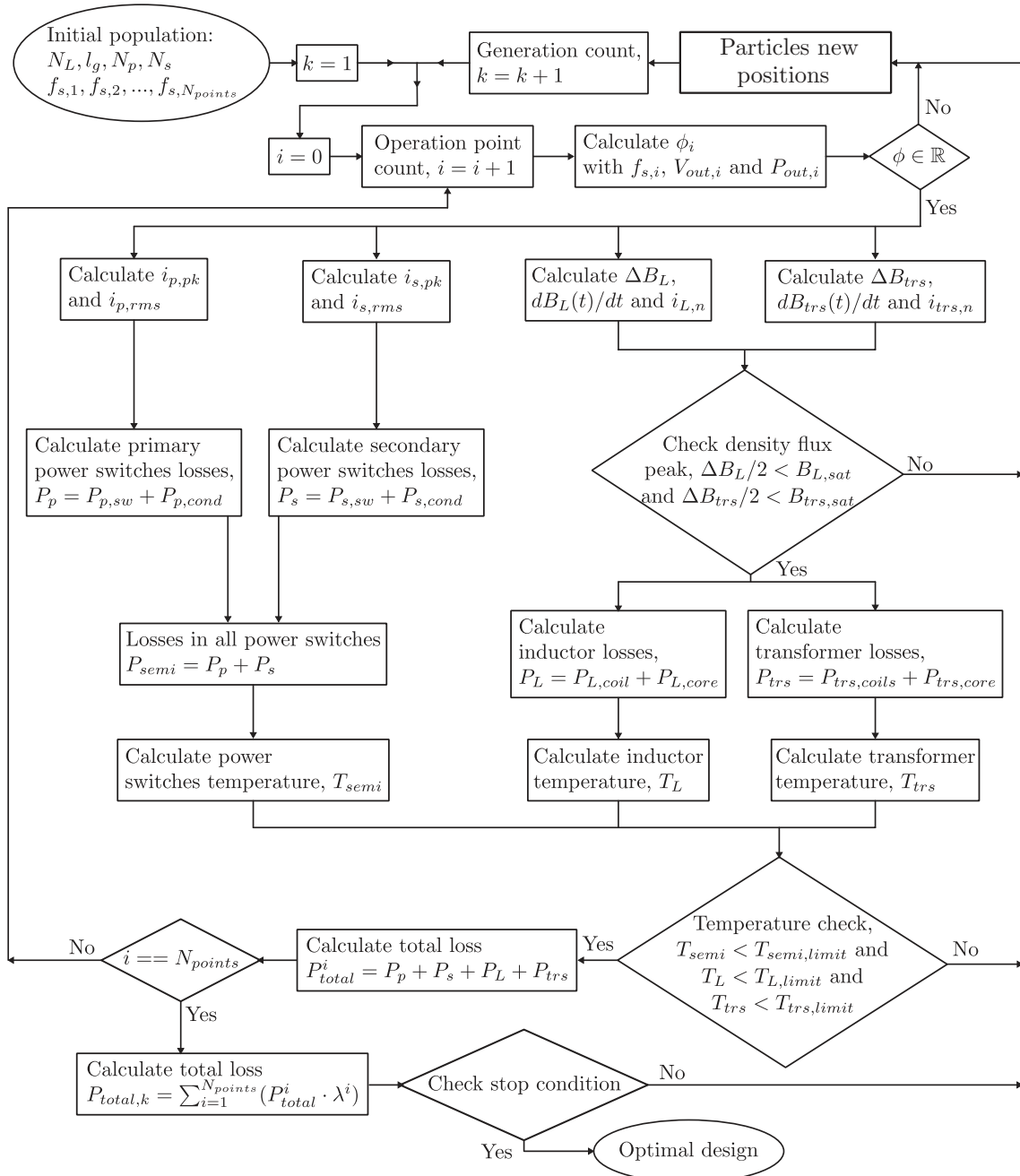
The optimization process, as depicted in Flowchart 3.1, revolves around the determination of five key parameters: the number of turns in the inductor ( $N_L$ ), the length of the inductor gap ( $l_g$ ), the number of turns in the primary ( $N_p$ ), the number of turns in the secondary ( $N_s$ ), and the switching frequency ( $f_s$ ).

Given the numerous potential solutions for the converter, the algorithm systematically explores and identifies the optimal combination for each operating point  $i$ . This process involves evaluating the population at every operation point. Notably, a distinct frequency ( $f_{s,i}$ ) is designated as the variable subject to optimization.

The determination of the angle ( $\phi$ ) for each operation point  $i$  is predicated on specific parameters, including the frequency ( $f_{s,i}$ ), output voltage ( $V_{o,i}$ ), and output power ( $P_{o,i}$ ).

Then, the following elements are calculated:

- the peak current in the primary power switches ( $i_{p,pk}$ );
- the RMS value of current in the primary power switches ( $i_{p,rms}$ );

**Figure 3.1** – Design optimization flowchart for obtaining construction parameters.

Note. Own authorship.

- the peak current in the secondary power switches ( $i_{s,pk}$ );
- the RMS value of current in the secondary power switches ( $i_{s,rms}$ );
- the peak-to-peak density flux in the inductor ( $\Delta B_L$ );
- the derivative of the density flux in the inductor ( $dB_L(t)/dt$ );
- the inductor current in  $n^{th}$  harmonic ( $i_{L,n}$ );
- the peak-to-peak density flux in the transformer ( $\Delta B_{trs}$ );
- the derivative of the density flux in the transformer ( $dB_{trs}(t)/dt$ );
- and the transformer current in ( $i_{trs,n}$ ) at  $n^{th}$  harmonic.

With these values at hand, it becomes feasible to evaluate potential magnetic element saturation and subsequently initiate the optimization process. This involves calculating the power losses inherent to the converter, which primarily embraces:

- the primary power switches ( $S_p$ );
- the secondary power switches ( $S_s$ );
- the inductor losses ( $P_L$ );
- and the transformer losses ( $P_{trs}$ ).

Subsequently, it becomes possible to scrutinize whether any component within the converter surpasses the prescribed temperature limits. Specifically, this involves ensuring that the power switches' temperature ( $T_{Semi}$ ) remains below ( $T_{Semi,limit}$ ), the inductor's temperature ( $T_L$ ) stays under ( $T_{L,limit}$ ), and the transformer's temperature ( $T_{trs}$ ) does not exceed ( $T_{trs,limit}$ ). Should any of these conditions be violated, the algorithm rejects the population, prompting a mutation of parameters before undergoing retesting.

The rms value for the current for the primary side of the converter can be given by the equation,

$$i_{rms,pri} = 2\sqrt{f_s \left( \int_{t_0}^{t_1} \left( i_{L(t_0)} + \frac{i_{L(t_1)} - i_{L(t_0)}}{t_1 - t_0} t \right)^2 dt + \int_{t_1}^{t_2} \left( i_{L(t_1)} + \frac{i_{L(t_2)} - i_{L(t_1)}}{t_2 - t_1} t \right)^2 dt \right)}, \quad (3.2)$$

as such the rms value of current for the secondary side is given by,

$$i_{rms,sec} = i_{rms,p} \cdot \frac{1}{n}, \quad (3.3)$$

The rms value of current for the primary switches ( $i_{p,rms}$ ) of the converter are be given by the equation,

$$i_{p,rms} = \frac{i_{rms,pri}}{\sqrt{2}}, \quad (3.4)$$

the same way, the rms value of current for the secondary switches ( $i_{s,rms}$ ) of the converter are be given by the equation,

$$i_{s,rms} = \frac{i_{rms,sec}}{\sqrt{2}}. \quad (3.5)$$

### 3.3 DAB CONVERTER PARAMETERS DEFINITION

Once the material characteristics, upper and lower bounds, and optimization objectives are established, all prerequisites for commencing the optimization process are fulfilled. This allows for the calculation of converter parameters, wherein each iteration involves incrementing the values for  $N_L$ ,  $l_g$ ,  $N_p$ ,  $N_s$ , and  $f_s$  through the PSO algorithm, while concurrently computing the total power losses for the converter. Additionally, characteristics pertaining to component construction, such as those of the transformer and inductor, as well as the converter's operational frequency and phase shift, are defined in tandem.

#### 3.3.1 Inductor

The inductor construction is defined by the selected material characteristics, so its inductance ( $L$ ) can be defined by the equation

$$L = \frac{\mu_{ef} \cdot \mu_0 \cdot A_e}{l_e} \cdot N_t^2, \quad (3.6)$$

the effective relative permeability ( $\mu_{ef}$ ) is determined by the ratio of the magnetic permeability of the material ( $\mu_0$ ) to the product of the effective magnetic cross section ( $A_e$ ) and the effective magnetic path length ( $l_e$ ) [39]. Mathematically,  $\mu_{ef}$  can be expressed as:

$$\mu_{ef} = \frac{\mu_r}{1 + \mu_r \cdot \frac{l_{gap}}{l_e}}, \quad (3.7)$$

thus, the PSO algorithm furnishes all the requisite parameters for constructing the inductor, embracing the necessary core gap ( $l_g$ ) and the number of turns in the windings ( $N_L$ ).

#### 3.3.2 Transformer

The construction process for the transformer mirrors that of the inductor. Material characteristics and optimization bounds are defined, and at each iteration, parameters such as  $N_p$  and  $N_s$  are adjusted, leading to the determination of a transformer ratio ( $n$ ). Given a specified input voltage ( $V_i$ ) and output voltage ( $V_o$ ), the optimization process incrementally

adjusts variables to achieve the most efficient transformer ratio ( $n$ ) by comparing power losses and identifying a solution that optimizes losses across all operation points.

Utilizing the provided equations and following the outlined flowchart, one can proceed to evaluate power losses and assess the feasibility of each converter design until arriving at an optimized solution.

### 3.4 POWER LOSSES AND THERMAL MODELS

The study incorporates models for losses and thermal effects, embracing both semiconductor losses and magnetic losses.

#### 3.4.1 Semiconductor losses

The Semiconductor losses are divided into two main categories: conduction losses and switching losses.

- Conduction losses: These losses are calculated upon the on-resistance ( $R_{ds-on}$ ) of the switches and the RMS value of the currents at the switches and can be expressed by the equation,

$$P_{cond} = R_{ds-on} \cdot I_{rms,i}^2 \quad (3.8)$$

- Switching losses: These losses are calculated based on the energy characteristics as specified in the manufacturer's datasheets for the switches, the switching losses for the turn-on of the switches is given by

$$P_{on} = E_{on,i} \cdot f_s, \quad (3.9)$$

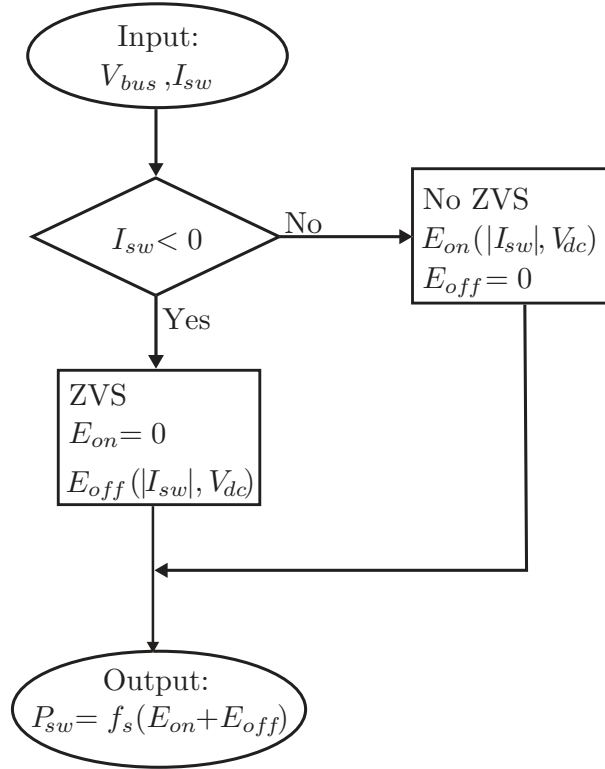
while the switching losses for the turn-off is given by

$$P_{off} = E_{off,i} \cdot f_s. \quad (3.10)$$

resulting on the total switching losses being

$$P_{sw} = P_{on} + P_{off}. \quad (3.11)$$

Based on the flowchart depicted in Figure 3.2, the calculation of switching losses hinges on the values of  $V_{bus}$  and  $I_{sw}$  for both the primary and secondary sides of the converter. Specifically, achieving zero voltage switching (ZVS) occurs when  $I_{sw} < 0$  during turn-on.

**Figure 3.2** – Switching loss flowchart.

Note. Own authorship.

### 3.4.2 Magnetic losses

For the magnetic losses, the DAB converter comprises two magnetic elements: the transformer and the inductor. Each of these elements incurs losses in their copper windings and magnetic cores.

#### 3.4.2.1 Core losses

The core losses can be calculated Steinmetz Equation [40] expressed as,

$$P_v = k_c f_s^\alpha B_{max}^\beta, \quad (3.12)$$

where:

- $k_c$ ,  $\alpha$ , and  $\beta$ : material constants usually found on manufacturer's datasheet;
- $B_{max}$ : peak value for the magnetic flux density
- $f_s$ : operational frequency.

While the Steinmetz Equation is frequently employed to estimate core losses under sinusoidal excitation, its applicability diminishes when addressing power electronics applications characterized by non-sinusoidal waveforms, DC components, or multiple frequencies. In such scenarios, the core losses are more accurately computed using an

improved model known as the Generalized Steinmetz Equation (iGSE), as proposed in [41]. This variant of the Steinmetz Equation is specifically tailored to account for the diverse waveform characteristics and frequency components encountered in modern power electronics systems.

$$P_v = \frac{1}{T} \int_0^T k_i \left| \frac{dB(t)}{dt} \right|^\alpha |\Delta B|^{\beta-\alpha} dt, \quad (3.13)$$

where  $k_i$  is defined by the equation,

$$k_i = \frac{k_c}{(2\pi)^{\alpha-1} \int_0^{2\pi} |\cos\theta|^\alpha 2^{\beta-\alpha} d\theta}, \quad (3.14)$$

This methodology takes into consideration the peak-to-peak magnetic flux density ( $\Delta B$ ) instead of solely the peak value. By doing so, it becomes possible to time-average the power loss for each segment of operation [42].

The magnetic flux density ( $B$ ) can be determined using the following equations for a magnetic element [43]:

- through the voltage:

$$B(t) = \int_0^t \frac{v(t)}{NA_c} dt, \quad (3.15)$$

where  $v(t)$  is the voltage at the magnetic element,  $N$  the number of turns,  $A_c$  the cross-sectional area of the magnetic core.

- through the current:

$$B(t) = \frac{i(t) \cdot L}{NA_c}, \quad (3.16)$$

where  $i(t)$  is the current at the magnetic element,  $N$  the number of turns,  $A_c$  the cross-sectional area of the magnetic core.

The peak-to-peak flux density can be calculated by

$$\Delta B = \max(B(t)) - \min(B(t)), \quad (3.17)$$

By analyzing the voltage levels across the inductor and transformer during the intervals delineated in Figure 2.9, it becomes feasible to ascertain the magnetic flux density for each component. Consequently, the peak-to-peak density flux for the inductor ( $\Delta B_L$ ) and the transformer ( $\Delta B_{trs}$ ) can be derived, enabling the PSO algorithm to determine the core loss within the magnetic elements.

### 3.4.2.2 Copper losses

Copper losses in the windings result from the skin effect and proximity effect, which are exacerbated by high-frequency operation. These phenomena lead to an increase in the AC resistance of the windings [44, 45]. The assessment of these losses is facilitated through the utilization of Dowell's equation [46].

$$F_R = \frac{R_{w,ac}}{R_{w,dc}} = A(F_p + F_s), \quad (3.18)$$

its possible to to determinate the ratio  $F_R$  of the DC resistance ( $R_{w,dc}$ ) and the AC resistance ( $R_{w,ac}$ ) for the windings where:

$$A = \frac{d_w}{\delta_w}, \quad (3.19)$$

with  $\delta_w$  being skin depth of the wire, and  $d_w$  being the equivalent square cross section width of the wire, determined by the equation,

$$d_w = \frac{\sqrt{\pi}}{2} \cdot D_m, \quad (3.20)$$

where  $D_m$  is the diameter of the circular cross section of the wire, the skin depth ( $\delta_w$ ) of the conductor is given by the equation,

$$\delta_w = \sqrt{\frac{\rho_w}{\pi\mu_0 f s}} \quad (3.21)$$

where  $\rho_w$  is the resistivity of the material,  $\mu_0$  is the magnetic permeability of the free space and  $f s$  is the frequency of operation.

With  $F_p$  in the equation 3.22 being the proximity effect factor,  $F_s$  in the equation 3.23 being the skin effect factor and  $N_l$  the number of winding layers.

$$F_p = \frac{2(N_l^2 - 1)}{3} \cdot \frac{\sinh(A) - \sin(A)}{\cosh(A) + \cos(A)} \quad (3.22)$$

$$F_s = \frac{\sinh(2A) + \sin(2A)}{\cosh(2A) - \cos(2A)} \quad (3.23)$$

The implementation of litz wire necessitates adjustments to Dowell's equation. Litz wire is chosen for its ability to mitigate skin effect and proximity effect losses, achieved through its design as a multi-strand conductor that distributes the total cross-sectional area of the wire across numerous conductors [47]. Consequently, with the utilization of litz wire, Dowell's equation is modified as follows:

$$A = \left(\frac{\pi}{4}\right)^{0.75} \frac{d_l}{\delta_w} \sqrt{\eta p}, \quad (3.24)$$



$$F_p = \frac{2(N_l^2 \cdot k - 1)}{3} \cdot \frac{\sinh(A) - \sin(A)}{\cosh(A) + \cos(A)}, \quad (3.25)$$

where  $d_l$  is the diameter of the litz-wire strand conductor,  $N_l$  is the number of winding layers,  $k$  the number of strands, and  $\eta p$  is the equivalent porosity factor for the litz-wire.

The  $R_{w,dc}$  resistance is obtained with the equation,

$$R_{w,dc} = \frac{4\rho_w N_l}{k\pi d_l^2} \cdot \frac{\sinh(A) - \sin(A)}{\cosh(A) + \cos(A)}, \quad (3.26)$$

the  $R_{w,ac}$  resistance can be determined the equation 3.18, where,

$$R_{w,ac} = F_R \cdot R_{w,dc}, \quad (3.27)$$

then the copper losses are given by the equation

$$P_{cu} = \sum_{j=1}^{\infty} R_{w,ac} I_n(f)^2, \quad (3.28)$$

since these resistances are contingent on frequency, the calculation involves multiplying the  $R_{w,ac}$  resistance with the root mean square (rms) value of current for the odd harmonic frequencies  $I_n$ , computed through a Fourier series analysis.

Consequently, the overall loss in the magnetic elements of the converter is determined by summing the copper losses and core losses of each element. This summation embraces the losses in the inductor, the primary winding of the transformer, and the secondary winding of the transformer.

### 3.4.3 Thermal Models

The thermal models utilized in this study are derived from [45] for the magnetic components and [48] for the semiconductors. This methodology serves a dual purpose: it enables the estimation of temperature increases in the components and functions as a constraint within the PSO algorithm. Specifically, it sets temperature limits for the magnetic components ( $T_L$  and  $T_{trs}$ ) and the semiconductors ( $T_{semi}$ ).

#### 3.4.3.1 Semiconductors thermal models

The temperature rise of the semiconductors  $T_{emp_{sw}}$  is estimated based on the power losses of the switches, by the equation

$$T_{semi} = P_{semi} \cdot \left( R_{htk} + \frac{(R_{th_{iso}} \cdot N_{sw}) + R_{jc}}{N_{sw}} \right) + T_a, \quad (3.29)$$

in the thermal analysis,  $P_{semi}$  represents the power losses in the semiconductors, while  $R_{jc}$  denotes the junction-to-case thermal resistance. The heat-sink thermal resistance is

denoted by  $R_{htk}$ , and  $R_{th_{iso}}$  signifies the insulator thermal resistance.  $N_{sw}$  refers to the number of switches mounted on the heat sink, and  $T_a$  represents the ambient temperature.

### 3.4.3.2 Magnetic thermal models

The temperature rise of the magnetic elements is given by power loss density ( $\Psi$ ) of the element,

$$\Psi = \frac{P_{cw}[W]}{A_t[cm^2]} \quad (3.30)$$

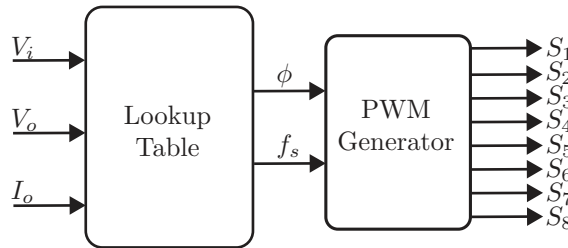
where  $P_{cw}$  is the total power loss of the element, including its core losses and winding losses, and  $A_t$  is the outer heat radiating surface area. With this the temperature rise ( $\Delta T$ ) can be defined as

$$\Delta T = 450\Psi^{0.826}[^{\circ}C]. \quad (3.31)$$

### 3.4.4 Lookup table

As previously referenced, the DAB converter boasts a remarkable degree of flexibility owing to its ability to finely adjust both the phase shift ( $\phi$ ) and frequency ( $f_s$ ). Figure 3.3 illustrates the modulation capability employed to generate the necessary PWM signals. These signals controls the power switches integrated within the converter.

**Figure 3.3** – PWM generator based on lookup table.



Note. Own authorship.

A lookup table is generated to determine the optimal operational point for the converter. This table is structured to evaluate the most favorable combination of phase shift angle and frequency, taking into account parameters such as  $V_o$  and  $I_o$ . Through this process, an efficiency map for the converter is created, showcasing the results obtained from the optimization efforts.

## 3.5 CONCLUSION

This chapter provides a concise overview of particle swarm optimization (PSO) and its broad applications. Subsequently, the primary optimization process is delineated

through a detailed flowchart, emphasizing the central objective of minimizing power losses within the converter.

The discussion further elaborates on the computation of power losses and thermal models specific to each major component. Special attention is given to the methodologies employed for the magnetic elements and power switches, elucidating the intricate processes involved in optimizing their performance.

---

## Optimization Process

This chapter delineated the parameters employed in the optimization process, along with their respective upper and lower bounds, to streamline the execution of the PSO algorithm. The resulting outcomes have been elucidated, accompanied by supplementary configurations aimed at augmenting the optimization procedure. A comparative analysis has been conducted between distinct configurations within the optimization framework: one with a fixed frequency value and another varying the frequency values for each operational point. Furthermore, an assessment of the achieved outcomes at this stage has been provided, with a delineation of the Zero Voltage Switching (ZVS) regions for the converter under both optimization configurations, facilitating a comprehensive comparison.

### 4.1 OBJECTIVE OF THE CONVERTER OPTIMIZATION DESIGN

The DAB converter optimization presented in this work is designed with the objective of reducing the overall power losses, maximising the efficiency ( $\eta$ ) as seen in the objective function equation ( $f_{ob}$ ) 4.1, maintaining fixed values for input voltage ( $V_i$ ) and Power output ( $P_o$ ), while varying the voltage output ( $V_o$ ),

- $V_i$ : (400 V);
- $P_o$ : (2 kW);
- $\vec{V}_o$ : (300 V 350 V 400 V 450 V);

$$\max f_{ob}(i) = \eta(i) = \left( \eta \Big|_{V_o = \vec{V}_o(i)} \right). \quad (4.1)$$

### 4.2 PSO INITIALIZATION

The optimization process in this study is driven by key parameters such as  $P_o$  and  $V_o$ , complemented by upper and lower bounds for the initial population. These parameters,

depicted in the flowchart Figure 3.1, are accompanied by a comprehensive material list table. Each material in the list has been meticulously characterized, taking into account its unique properties and limitations, all of which are factored into the optimization limits.

The upper and lower bounds necessary to create the initial population for the PSO algorithm, are detailed in the accompanying Table 4.1.

**Table 4.1** – Optimization limits.

| Parameter | Lower Bounds | Upper Bounds |
|-----------|--------------|--------------|
| $N_L$     | 2            | 15           |
| $l_g$     | 0.02 mm      | 2.0 mm       |
| $N_p$     | 2            | 15           |
| $N_s$     | 2            | 15           |
| $f_s$     | 20 kHz       | 150 kHz      |

Note. Own authorship.

The materials utilized in this study have been extensively detailed in Table 4.2. Each material's specific characteristics for the validity of the model have been considered. This includes factors such as electrical characteristics for the switches, magnetic permeability for the ferrite cores, and other relevant attributes that play a significant role in the optimization strategy.

**Table 4.2** – Material list.

| Components                 | Code           |
|----------------------------|----------------|
| Primary power switches     | C3M0075120K    |
| Secondary power switches   | C3M0075120K    |
| Primary Heatsink           | LAM4K15012     |
| Secondary Heatsink         | LAM4K15012     |
| Inductor core              | E80/38/20-N87  |
| Inductor wire              | 392x37AWG Litz |
| Transformer core           | E80/38/20-N87  |
| Transformer primary wire   | 392x37AWG Litz |
| Transformer secondary wire | 392x37AWG Litz |

Note. Own authorship.

### 4.3 DAB OPTIMIZATION RESULTS

After the optimization process concludes, the specifications for the DAB converter can be obtained. During this stage, the construction parameters have undergone optimization under specific conditions, including a fixed input voltage of 400 V, an output power of 2 kW, and a variable output voltage ranging from 300 V to 450 V. The results derived from this optimization process are meticulously presented in Table 4.3.

**Table 4.3** – Optimum design summary.

| Optimized converter parameters |               |
|--------------------------------|---------------|
| $N_p$                          | 14            |
| $N_s$                          | 12            |
| $N_L$                          | 14            |
| $l_g$                          | 0.52 mm       |
| $f_s$                          | 60 kHz        |
| $L_{dab}$                      | 87.69 $\mu$ H |
| $T_{semi-p}^{max}$             | 37°C          |
| $T_{semi-s}^{max}$             | 40°C          |
| $T_{tr}^{max}$                 | 113°C         |
| $T_L^{max}$                    | 98°C          |
| $B_{L-pk}^{max}$               | 328 mT        |
| $B_{tr-pk}^{max}$              | 200 mT        |

Note. Own authorship.

For each operation point was defined a phase shift by the optimization, allowing the desired power flow in the converter as presented in the Table 4.4.

**Table 4.4** – Converter's frequency and phase shift and operation points.

| i     | $V_i$ [V] | $V_o$ [V] | $f_s$ [kHz] | $\phi$ | $P_o$ [W] |
|-------|-----------|-----------|-------------|--------|-----------|
| i = 1 | 400       | 300       | 60          | 33.17  | 2000      |
| i = 2 | 400       | 350       | 60          | 27.35  | 2000      |
| i = 3 | 400       | 400       | 60          | 23.31  | 2000      |
| i = 4 | 400       | 450       | 60          | 20.33  | 2000      |

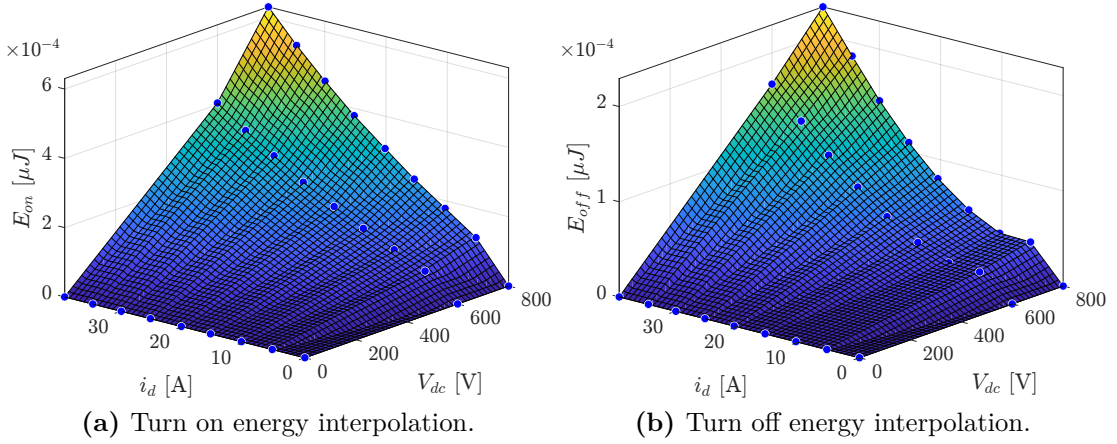
Note. Own authorship.

#### 4.3.1 Power switches losses results

As outlined in the preceding chapter, the losses incurred by the power switches are calculated by summing the conduction losses with the switching losses.

In line with this, to obtain accurate data regarding the turn-on and turn-off energy curves for the C3M007512K switches from Wolfspeed, interpolation becomes essential. This necessity arises because the manufacturer's datasheet only provides voltage levels for 600 V and 800 V, whereas the optimized design targets voltage levels ranging from 300 V to 450 V. Consequently, the interpolated turn-on energy curve is depicted in Figure 4.1a, while the turn-off energy curve is represented in Figure 4.1b.

**Figure 4.1** – Energy interpolation curves.



Note. Own authorship.

Indeed, as previously discussed in the preceding chapter, the equations 3.9 and 3.10 detail the process for calculating the switching losses at each operation point  $i$ .

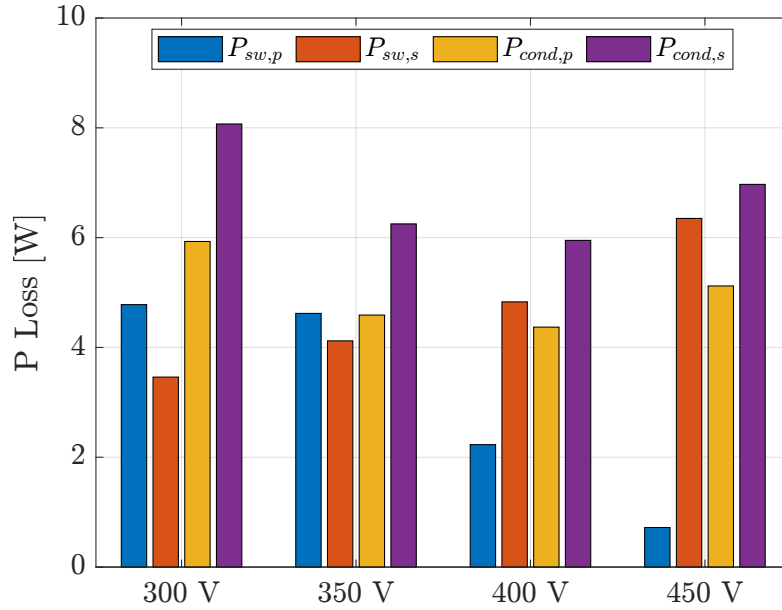
Moreover, for the conduction losses, the equation 3.8 elucidates the method for determining the conduction losses at each operation point  $i$ , which culminates in the presentation of power switch losses in Table 4.5.

**Table 4.5** – Switches power losses.

| $i$     | $V_o$ [V] | $P_{sw,p}$ [W] | $P_{sw,s}$ [W] | $P_{cond,p}$ [W] | $P_{cond,s}$ [W] |
|---------|-----------|----------------|----------------|------------------|------------------|
| $i = 1$ | 300       | 4.78           | 3.46           | 5.93             | 8.07             |
| $i = 2$ | 350       | 4.62           | 4.12           | 4.59             | 6.25             |
| $i = 3$ | 400       | 2.23           | 4.83           | 4.37             | 5.95             |
| $i = 4$ | 450       | 0.72           | 6.35           | 5.12             | 6.97             |

Note. Own authorship.

On the graphs on the Figure 4.2, shows that the switches power losses are higher on the 300 V point, with most of the variation on the losses being present on the switching losses.

**Figure 4.2** – Switches power losses [W].

### 4.3.2 Magnetics results

The optimization process yielded an inductance ( $L$ ) of  $87.69 \mu\text{H}$  for the inductor, with a gap ( $l_g$ ) of  $0.52 \text{ mm}$  and 14 turns ( $N_L$ ) for the windings.

However, regarding the transformer, initial results were not satisfactory due to exceeding the temperature limit ( $T_{trs,limit}$ ) and reaching the maximum density flux ( $B_{trs,sat}$ ), which could lead to core saturation. To address this issue, a workaround was implemented by employing two transformers connected in series. This approach effectively divided both the temperature and density flux stresses by half, making the design feasible. The detailed results for the magnetic elements can be observed in Table 4.6.

**Table 4.6** – Magnetics elements power losses.

| i     | $V_o$ [V] | $P_{ind,core}$ [W] | $P_{ind,cu}$ [W] | $P_{trs,core}$ [W] | $P_{trs,p,cu}$ [W] | $P_{trs,s,cu}$ [W] |
|-------|-----------|--------------------|------------------|--------------------|--------------------|--------------------|
| i = 1 | 300       | 13.77              | 13.77            | 9.83               | 13.13              | 8.27               |
| i = 2 | 350       | 7.96               | 10.36            | 14.13              | 10.36              | 6.52               |
| i = 3 | 400       | 12.14              | 9.87             | 19.34              | 9.87               | 6.22               |
| i = 4 | 450       | 18.91              | 11.38            | 25.50              | 11.38              | 7.16               |

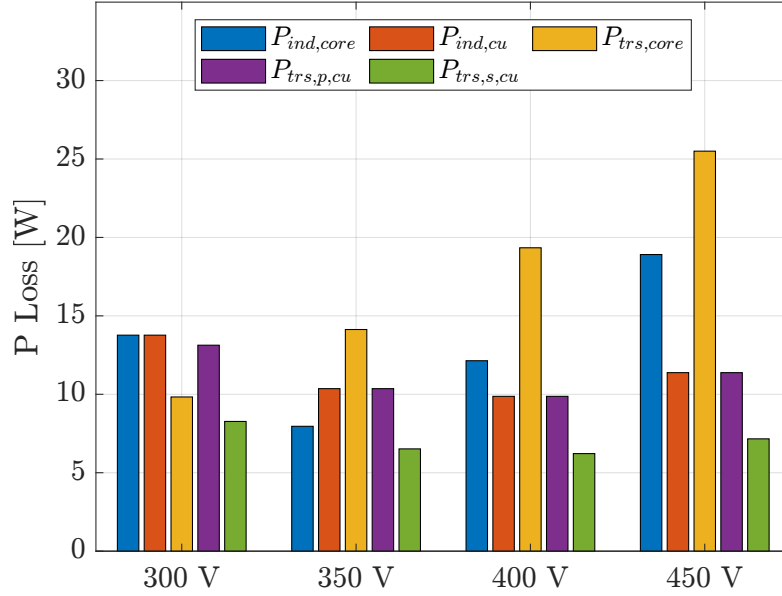
Note. Own authorship.

where the power losses in the inductor's magnetic core ( $P_{ind,core}$ ) and the power losses in the inductor's copper windings ( $P_{ind,cu}$ ) were calculated. Similarly, the power losses in the transformer's magnetic core ( $P_{trs,core}$ ), the power losses in the transformer primary's copper windings ( $P_{trs,p,cu}$ ), and the power losses in the transformer secondary's copper windings ( $P_{trs,s,cu}$ ) were determined.



By seeing graphs on the Figure 4.3 the magnetic power losses are high at the 450 V point.

**Figure 4.3** – Magnetic elements power losses [W].



The maximum density flux for both the transformer and inductor is outlined in Table 4.7.

**Table 4.7** – Magnetics elements density flux.

| i     | $V_o$ [V] | $B_{L-pk}^{max}$ [mT] | $B_{tr-pk}^{max}$ [mT] |
|-------|-----------|-----------------------|------------------------|
| i = 1 | 300       | 134                   | 273                    |
| i = 2 | 350       | 156                   | 198                    |
| i = 3 | 400       | 175                   | 259                    |
| i = 4 | 450       | 200                   | 328                    |

Note. Own authorship.

where  $B_{L-pk}^{max}$  is the maximum flux density of the inductor and  $B_{tr-pk}^{max}$  is the maximum flux density of the transformer. The temperature rise for the above mentioned components is described in the Table 4.8,

**Table 4.8** – Components temperature rise.

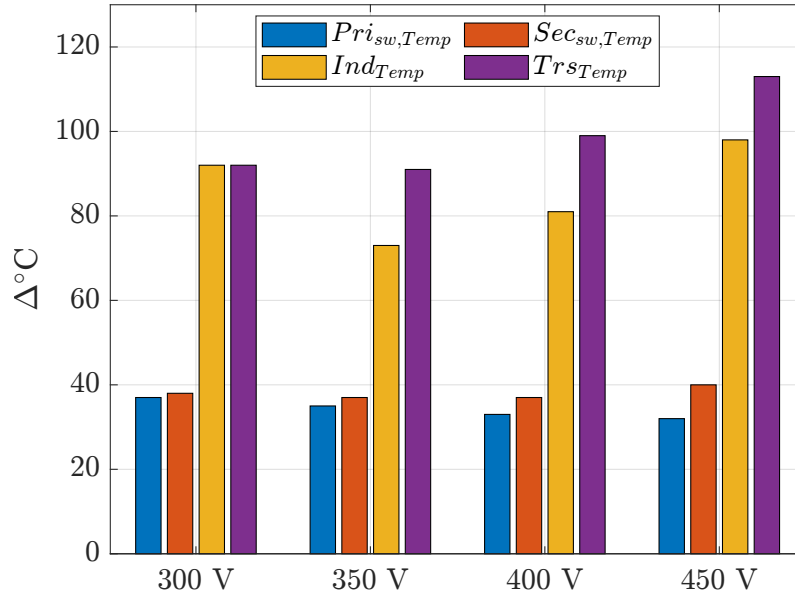
| i     | $V_o$ [V] | $Pr_{i_{sw},Temp}$ [°C] | $Sec_{sw,Temp}$ [°C] | $Ind_{Temp}$ [°C] | $Trs_{Temp}$ [°C] |
|-------|-----------|-------------------------|----------------------|-------------------|-------------------|
| i = 1 | 300       | 37°C                    | 38°C                 | 92°C              | 92°C              |
| i = 2 | 350       | 35°C                    | 37°C                 | 73°C              | 91°C              |
| i = 3 | 400       | 33°C                    | 37°C                 | 81°C              | 99°C              |
| i = 4 | 450       | 32°C                    | 40°C                 | 98°C              | 113°C             |

Note. Own authorship.

where  $Pri_{sw,Temp}$  is the temperature rise in the primary switches,  $Sec_{sw,Temp}$  is the temperature rise in the secondary switches,  $Ind_{Temp}$  is the temperature rise in the inductor and  $Trs_{Temp}$  is the temperature rise in the transformer.

The temperature rise show in graphs on the Figure 4.4 demonstrates that there is no significant variation on the temperatures estimation.

**Figure 4.4** – Components temperature rise [ $^{\circ}\text{C}$ ].



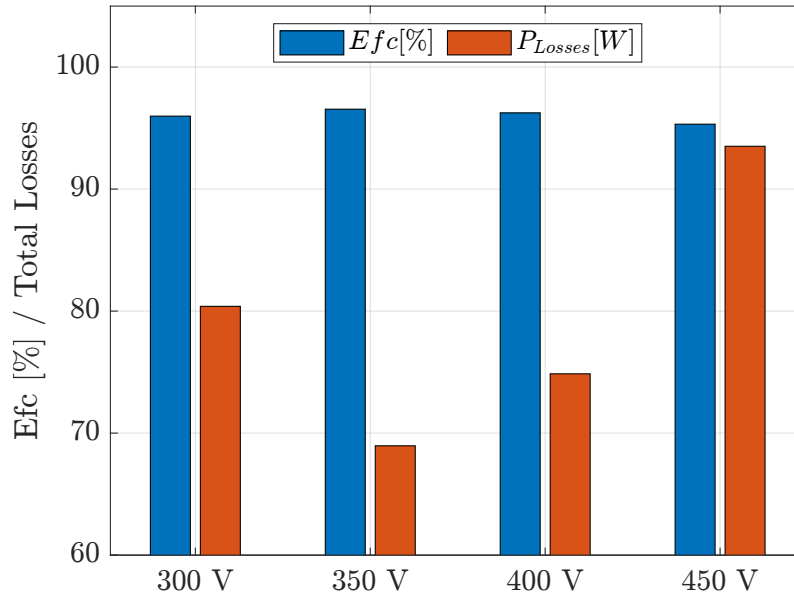
The theoretical converter efficiency for each operating point along with the total power losses of each point are presented in the Table 4.9.

**Table 4.9** – Theoretical converter's efficiency.

| i     | $V_o$ [V] | $Efc$ [%] | $P_{LOSS}$ [W] |
|-------|-----------|-----------|----------------|
| i = 1 | 300       | 95.98     | 80.39          |
| i = 2 | 350       | 96.55     | 68.96          |
| i = 3 | 400       | 96.25     | 74.86          |
| i = 4 | 450       | 95.32     | 93.51          |

Note. Own authorship.

By analyzing the graphs in Figure 4.5, which display the theoretical efficiency of the converter, it is evident that the efficiency remains approximately 95% across all points. However, there is variation in power losses for each point, with 350 V exhibiting the lowest losses and 450 V showing the highest.

**Figure 4.5** – Theoretical converter’s efficiency.

The results showcasing a converter efficiency exceeding 95% across all operational points, are indeed promising. However, further improvements are conceivable. The optimization process, as currently configured, maintains a fixed frequency for all operation points. As discussed in Chapter 3, adjusting both the frequency and the phase shift can yield variable outcomes, potentially leading to even higher efficiency levels.

#### 4.4 DAB OPTIMIZATION RESULTS - VARIABLE FREQUENCY

To introduce a variable frequency for the converter, a subsequent optimization process is required. This process utilizes the results obtained from the initial optimization, focusing solely on optimizing the frequency parameter. The objective is to achieve the optimal combination between the phase shift angle and frequency based on the output voltage ( $V_o$ ) and current ( $I_o$ ). It is important to highlight that the second optimization process significantly expedites the overall procedure, as there is only one parameter to optimize.

##### 4.4.1 Variable frequency optimization

Upon completion of the second optimization process, new specifications for the DAB converter have been obtained. The results of this optimization process are presented in Table 4.10.

The construction parameters remain unchanged; however, there are significant alterations in the maximum flux density of the magnetics, temperature rise of the components, and total losses. Additionally, the frequency and phase shift are now optimized, with the best frequency determined for each point concerning the constructed magnetics, as illustrated in the previous table.

**Table 4.10** – Optimum design summary variable frequency.

| Optimized converter parameters |                   |
|--------------------------------|-------------------|
| Variable frequency             |                   |
| $N_p$                          | 14                |
| $N_s$                          | 12                |
| $N_L$                          | 14                |
| $l_g$                          | 0.52 mm           |
| $f_s$                          | 30.91 – 61.54 kHz |
| $L_{dab}$                      | 87.69 $\mu$ H     |
| $T_{semi-p}^{max}$             | 34°C              |
| $T_{semi-s}^{max}$             | 40°C              |
| $T_{tr}^{max}$                 | 113°C             |
| $T_L^{max}$                    | 99°C              |
| $B_{L-pk}^{max}$               | 320 mT            |
| $B_{tr-pk}^{max}$              | 180 mT            |

Note. Own authorship.

For each operation point, a phase shift and an operational frequency have been defined through the optimization process, facilitating the desired power flow within the converter, as detailed in Table 4.11.

**Table 4.11** – Converter's frequency and phase shift - variable frequency.

| i     | $V_o$ [V] | $f_s$ [kHz] | $\phi$ |
|-------|-----------|-------------|--------|
| i = 1 | 300       | 30.91       | 15.22  |
| i = 2 | 350       | 34.01       | 14.28  |
| i = 3 | 400       | 43.05       | 15.98  |
| i = 4 | 450       | 61.54       | 20.94  |

Note. Own authorship.

#### 4.4.2 Power switches losses variable frequency results

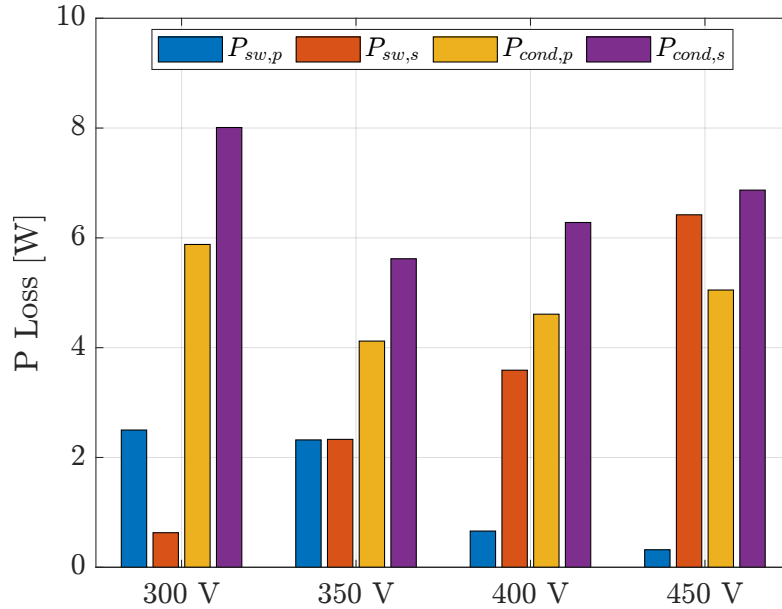
In the Table 4.12 can be seen the power losses for the switches when using variable frequency for each operation point.

**Table 4.12** – Power switch losses - variable frequency.

| i     | $V_o$ [V] | $P_{sw,p}$ [W] | $P_{sw,s}$ [W] | $P_{cond,p}$ [W] | $P_{cond,s}$ [W] |
|-------|-----------|----------------|----------------|------------------|------------------|
| i = 1 | 300       | 2.50           | 0.63           | 5.88             | 8.01             |
| i = 2 | 350       | 2.32           | 2.33           | 4.12             | 5.62             |
| i = 3 | 400       | 0.66           | 3.59           | 4.61             | 6.28             |
| i = 4 | 450       | 0.32           | 6.42           | 5.05             | 6.87             |

Note. Own authorship.

By examining the graphs in Figure 4.6, it is evident that the conduction losses of the switches remain comparable to those observed in the fixed frequency optimization. However, the switching losses are reduced, attributable to the lower operating frequency.

**Figure 4.6** – Switches power losses [W].

#### 4.4.3 Magnetics results - Variable Frequency

The results for the magnetic elements when using variable frequency are exhibited on the Table 4.13.

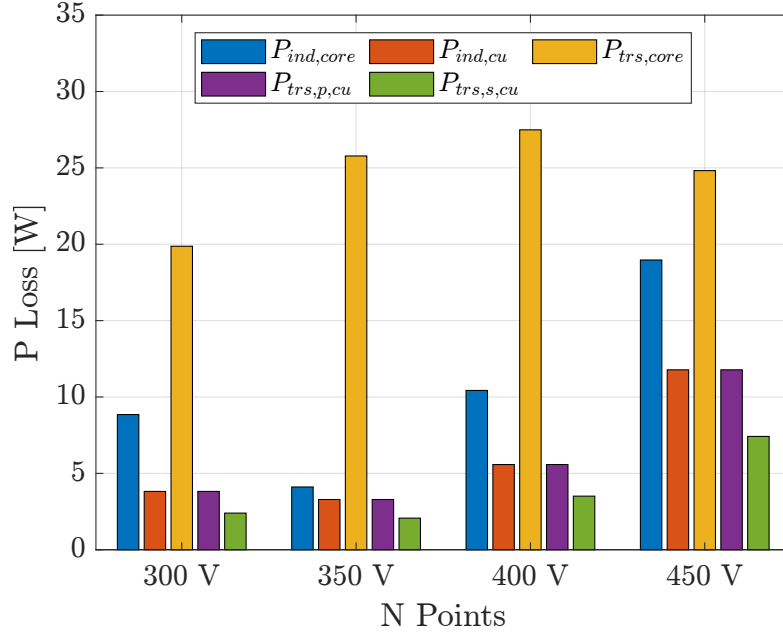
**Table 4.13** – Magnetics elements power losses.

| i     | $V_o$ [V] | $P_{ind,core}$ [W] | $P_{ind,cu}$ [W] | $P_{trs,core}$ [W] | $P_{trs,p,cu}$ [W] | $P_{trs,s,cu}$ [W] |
|-------|-----------|--------------------|------------------|--------------------|--------------------|--------------------|
| i = 1 | 300       | 8.85               | 3.82             | 19.87              | 3.82               | 2.40               |
| i = 2 | 350       | 4.11               | 3.29             | 25.78              | 3.29               | 2.07               |
| i = 3 | 400       | 10.43              | 5.58             | 27.49              | 5.58               | 3.51               |
| i = 4 | 450       | 18.97              | 11.78            | 24.82              | 11.78              | 7.42               |

Note. Own authorship.

The graphs in Figure 4.7 illustrate that the losses in the transformer core increase with the variable frequency. However, other prominent magnetic element losses, such as the winding losses, are significantly lower due to the optimized frequencies for each operating point.

**Figure 4.7** – Magnetic elements power losses.



The max density flux for variable frequency are exhibited on the Table 4.14.

**Table 4.14** – Magnetics elements density flux.

| i     | $V_o$ [V] | $B_{L-pk}^{max}$ [mT] | $B_{tr-s-pk}^{max}$ [mT] |
|-------|-----------|-----------------------|--------------------------|
| i = 1 | 300       | 323                   | 255                      |
| i = 2 | 350       | 193                   | 272                      |
| i = 3 | 400       | 292                   | 249                      |
| i = 4 | 450       | 324                   | 180                      |

Note. Own authorship.

The temperature rise for each component its shown in the Table 4.15.

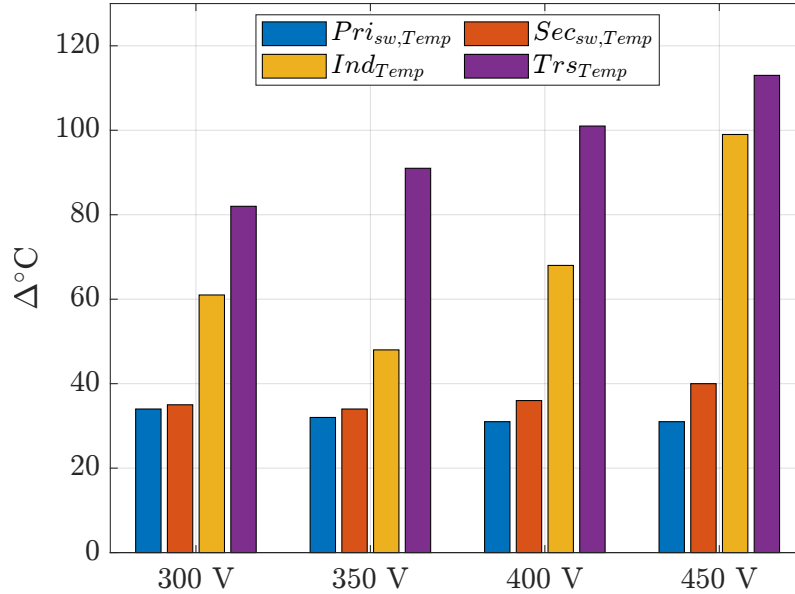
**Table 4.15** – Components temperature rise.

| i     | $V_o$ [V] | $Pr_{i-sw,Temp}$ [°C] | $Sec_{sw,Temp}$ [°C] | $Ind_{Temp}$ [°C] | $Trs_{Temp}$ [°C] |
|-------|-----------|-----------------------|----------------------|-------------------|-------------------|
| i = 1 | 300       | 34°C                  | 35°C                 | 61°C              | 82°C              |
| i = 2 | 350       | 32°C                  | 34°C                 | 48°C              | 91°C              |
| i = 3 | 400       | 31°C                  | 36°C                 | 68°C              | 101°C             |
| i = 4 | 450       | 31°C                  | 40°C                 | 99°C              | 113°C             |

Note. Own authorship.

The graphs in Figure 4.8 clearly indicate that the temperature rise estimation is not significantly impacted by the variable frequency optimization. This suggests that while other parameters may vary, the thermal performance of the converter remains stable across different frequencies.

**Figure 4.8** – Components temperature rise [ $^{\circ}\text{C}$ ].



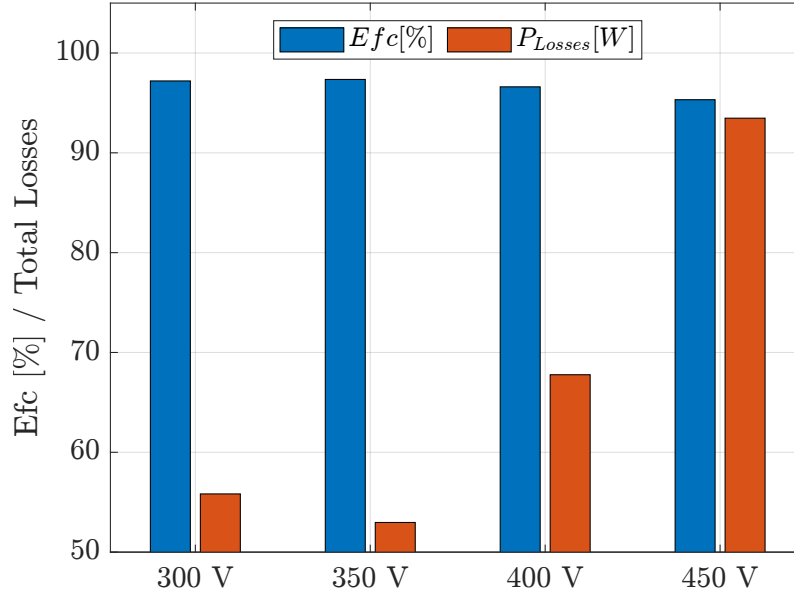
The theoretical efficiency for each point is shown in the Table 4.16.

**Table 4.16** – Theoretical converter's efficiency.

| i     | $V_o[V]$ | $Efc[\%]$ | $P_{LOSS}[W]$ |
|-------|----------|-----------|---------------|
| i = 1 | 300      | 97.20     | 55.83         |
| i = 2 | 350      | 97.35     | 52.97         |
| i = 3 | 400      | 96.61     | 67.77         |
| i = 4 | 450      | 95.32     | 93.47         |

Note. Own authorship.

The graphs in Figure 4.9 illustrate that total losses at each operational point are reduced when employing variable frequency optimization. This optimization results in the converter achieving an efficiency of 96.55% at the 350 V point.

**Figure 4.9** – Theoretical converter’s efficiency.

#### 4.4.4 Variable frequency x Fixed frequency comparison

As shown in Table 4.17, both designs share remarkable similarities. The most significant difference between the two designs is their operating frequencies. The fixed frequency design maintains a constant frequency of 60 kHz, whereas the variable frequency design spans a range from 30.91 kHz to 61.54 kHz.

**Table 4.17** – Optimum design summary comparison.

|                    | Fixed Frequency | Variable Frequency     |
|--------------------|-----------------|------------------------|
| $N_p$              | 14              | 14                     |
| $N_s$              | 12              | 12                     |
| $N_L$              | 14              | 14                     |
| $l_g$              | 0.52 mm         | 0.52 mm                |
| $f_s$              | 60 kHz          | 30.91 kHz to 61.54 kHz |
| $L_{dab}$          | 87.69 $\mu$ H   | 87.69 $\mu$ H          |
| $T_{semi-p}^{max}$ | 37°C            | 34°C                   |
| $T_{semi-s}^{max}$ | 40°C            | 40°C                   |
| $T_{tr}^{max}$     | 113°C           | 113°C                  |
| $T_L^{max}$        | 98°C            | 99°C                   |
| $B_{L-pk}^{max}$   | 328 mT          | 320 mT                 |
| $B_{tr-pk}^{max}$  | 200 mT          | 180 mT                 |

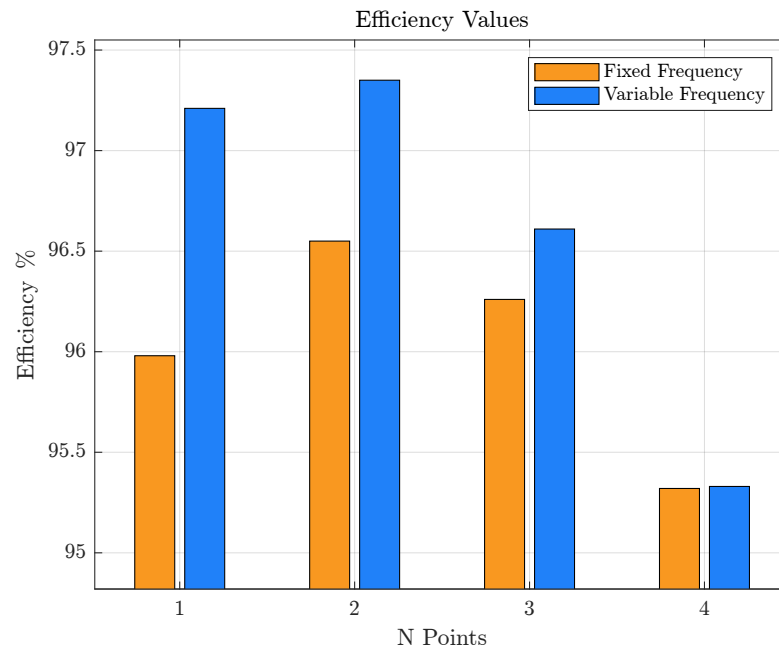
Note. Own authorship.

When evaluating the efficiency of both converter designs, it becomes apparent that both are viable options. However, upon closer examination, it is evident that the converter



with variable frequency optimization yields superior results. This is demonstrated in Figure 4.10, where the converter consistently achieves higher efficiency at every optimized point when considering variable frequency operation.

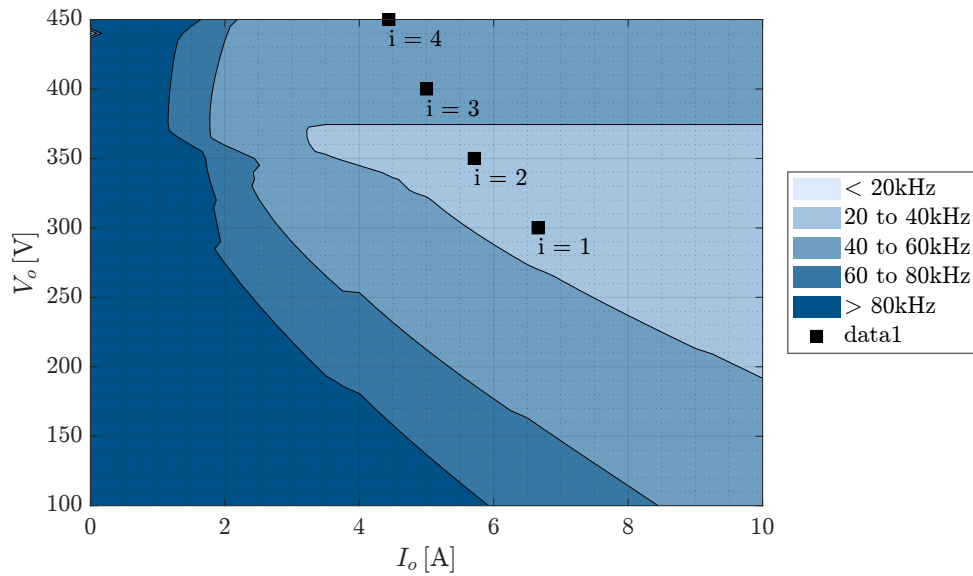
**Figure 4.10** – Converters efficiency comparison.



Note. Own authorship.

Creating a lookup table with multiple combinations of frequency and phase shift for the desired operating points of the converter allows for a comprehensive comparison between the fixed and variable frequency designs. This table presents various combinations of output power and output current, aiming to maximize the converter efficiency for any  $V_o$  and  $I_o$ , including points outside of the initially defined optimization range.

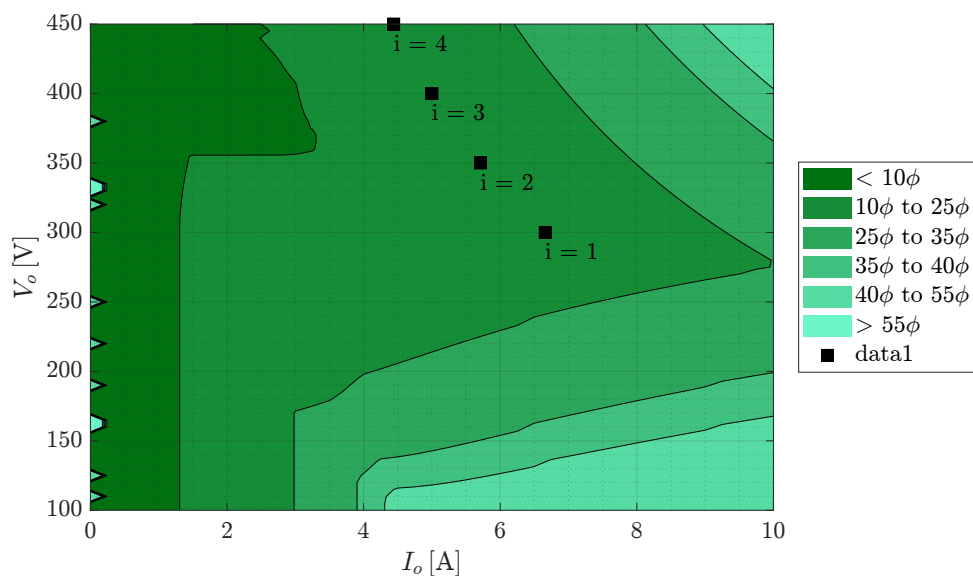
Figure 4.11 illustrates multiple values for the operation frequency ( $f_s$ ) of the converter. Notably, the operating frequency increases as the voltage and current of the converter decrease while still maintaining the desired power output. This dynamic relationship between frequency, voltage, current, and power output highlights the adaptability and efficiency potential of the variable frequency design.

**Figure 4.11** – Frequency lookup table ranging from 20 kHz < to > 80 kHz.

Note. Own authorship.

In Figure 4.11, contour lines based on the operation frequency were plotted to delineate the operation points for the desired  $V_o$  and  $I_o$ , aiding in better comprehension of the variable frequency design's performance.

Figure 4.12 illustrates multiple values for the phase shift ( $\phi$ ) of the converter. Notably, the phase shift increases as the voltage remains at a high value and the current of the converter decreases, all while maintaining the desired power output. This graphical representation further elucidates the relationship between phase shift, voltage, current, and power output in the converter's operation.

**Figure 4.12** – Phase-Shift lookup table ranging from < 10  $\phi$  to > 55  $\phi$ .

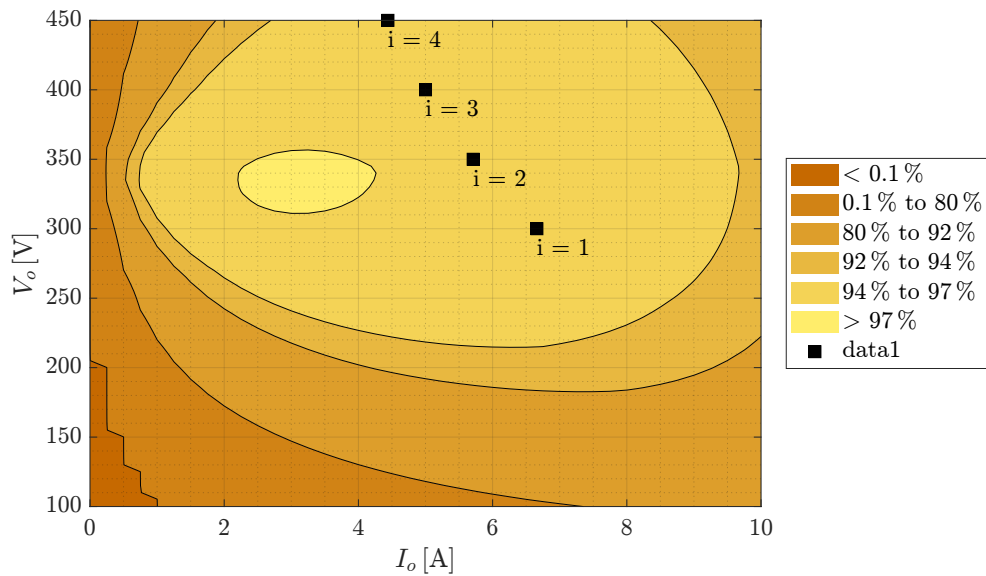
Note. Own authorship.

In Figure 4.12, contour lines based on the phase shift were plotted to delineate the

operation points for the desired  $V_o$  and  $I_o$ , aiding in better comprehension of the variable phase shift's impact on converter performance.

Comparing the DAB efficiency in the lookup tables shown in Figures 4.13 and 4.14, both can be considered as efficiency maps for the DAB converter, showcasing the efficiency variations across different operating points and configurations.

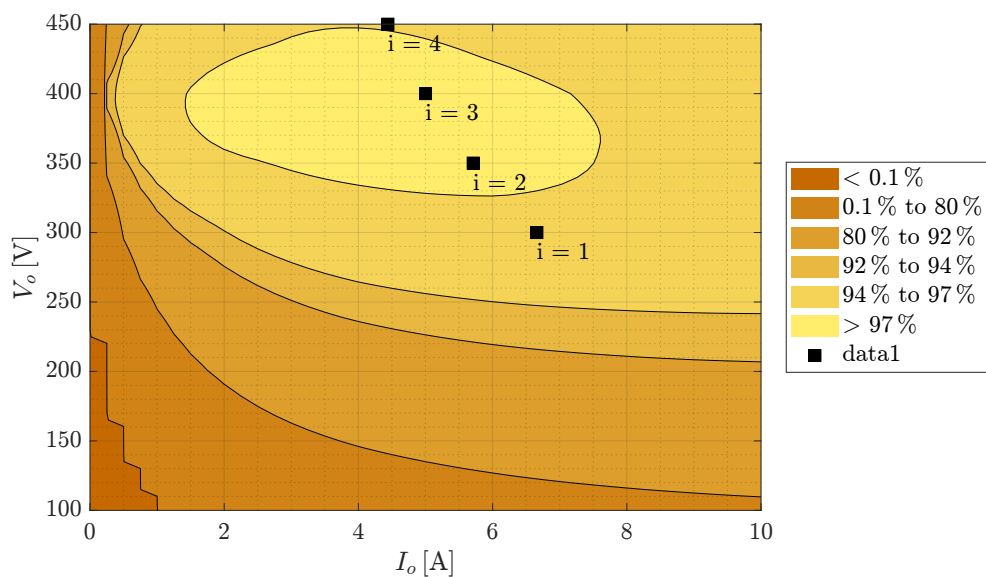
**Figure 4.13** – Dab Efficiency map FF ranging from  $<0.1\%$  to  $>97\%$ .



Note. Own authorship.

Figure 4.13 delineates a voltage span extending from 100 V to 450 V, complemented by a current range spanning from 0 A to 10 A, yielding a consistent power output of 2 kW across all points. This operational profile is maintained under a fixed frequency of 60 kHz, coupled with a phase shift that fluctuates between  $20.33 \phi$  and  $33.17 \phi$ .

**Figure 4.14** – Dab Efficiency map for VF ranging from  $<0.1\%$  to  $>97\%$ .

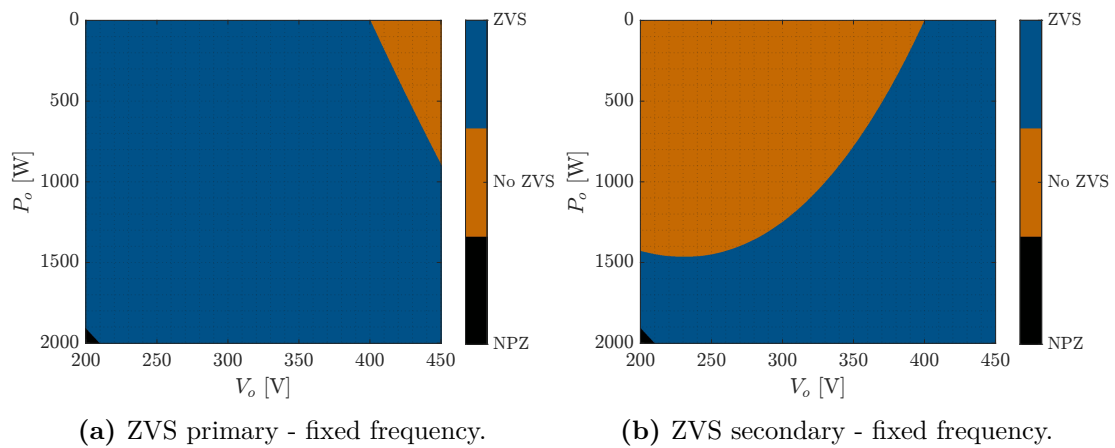


Note. Own authorship.

In Figure 4.14, a comprehensive analysis shows a voltage span of 100 V to 450 V, coupled with a current range from 0 A to 10 A, and a consistent power output of 2 kW across all points. This configuration operates under a variable frequency regime, oscillating between 30.91 kHz to 61.54 kHz, and a phase shift that varies between  $15.22 \phi$  and  $20.94 \phi$ .

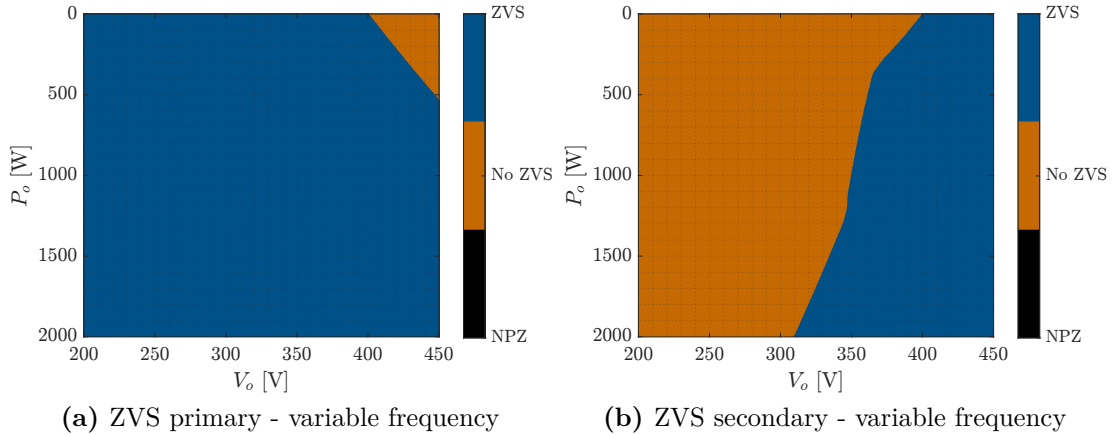
Upon examining the entirety of the figures, the disparity between employing a fixed frequency versus a variable frequency extends well beyond the displayed results in Figure 4.10. Although both strategies achieve an efficiency surpassing 97%, the operational range for this efficiency level is notably broader with variable frequency, showing the region between 94% and 97% efficiency.

Additionally, a comparison can be drawn regarding the Zero Voltage Switching (ZVS) regions for the converter, illustrated in Figures 4.15 and 4.16.



**Figure 4.15** – ZVS regions - fixed frequency.

In Figure 4.15a, the Zero Voltage Switching (ZVS) regions for the primary side of the converter are depicted, while Figure 4.15b illustrates the ZVS regions for the secondary side of the converter under fixed frequency conditions, ZVS is successfully achieved. This holds true for a majority of the operational scenarios outlined in the figures. Additionally, there is a region termed the non-project zone (NPZ), which designates the zone where no feasible project can be realized given the specified parameters.

**Figure 4.16** – ZVS regions - variable frequency.

Note. Own authorship.

In Figure 4.16a, the Zero Voltage Switching (ZVS) regions for the primary side of the converter are illustrated, while Figure 4.16b showcases the ZVS regions for the secondary side of the converter under variable frequency conditions. Notably, for most of the operation points outlined in Table ??, ZVS is effectively achieved. However, it's worth mentioning that achieving ZVS at 300 V is unattainable under these conditions, resulting in increased switching losses compared to the fixed frequency option. Another notable observation is the absence of the *NPZ* region in this scenario where the frequency is variable.

Despite the higher switching losses associated with this approach, the overall losses of the converter are lower due to the capability of operating at lower frequencies, thus contributing to higher efficiency.

#### 4.5 CONCLUSION

This chapter has detailed the parameters employed in the Particle Swarm Optimization (PSO) algorithm, including their upper and lower bounds. The initial results showcased a fixed frequency for the operation of the converter.

However, through a subsequent optimization process that enabled frequency adjustment for each operational point, significant refinements were achieved. It is noteworthy that while the initial results were viable, further improvements were attained without altering any construction parameters. By solely optimizing the frequency of operation, and considering losses dependent on the frequency, such as winding losses and switching losses, the converter's performance could be further improved with a secondary optimization.

---

## DAB converter Prototype

In this chapter, the entire converter assembly process, the testing setup, and the efficiency results obtained will be detailed. Additionally, a comparison between the theoretical values, simulations conducted using the software PLECS 4.7.2, and experimental results obtained from the constructed prototype will be provided.

### 5.1 PROTOTYPE CONSTRUCTION

According to the specifications outlined in the previous chapter, the optimization process was conducted for the operation points specified in Table 4.1. Subsequently, the optimal design for the prototype was selected, necessitating a variable frequency configuration. The parameters of this design are detailed in Table 5.1.

**Table 5.1** – DAB prototype parameters

| Parameter | Value         |
|-----------|---------------|
| $N_{tr}$  | 2             |
| $N_p$     | 14            |
| $N_s$     | 12            |
| $n$       | 0.83          |
| $l_g$     | 0.52 mm       |
| $N_L$     | 14            |
| $L_{dab}$ | 87.69 $\mu$ H |

Note. Own authorship.

### 5.2 MAGNETICS DESIGN

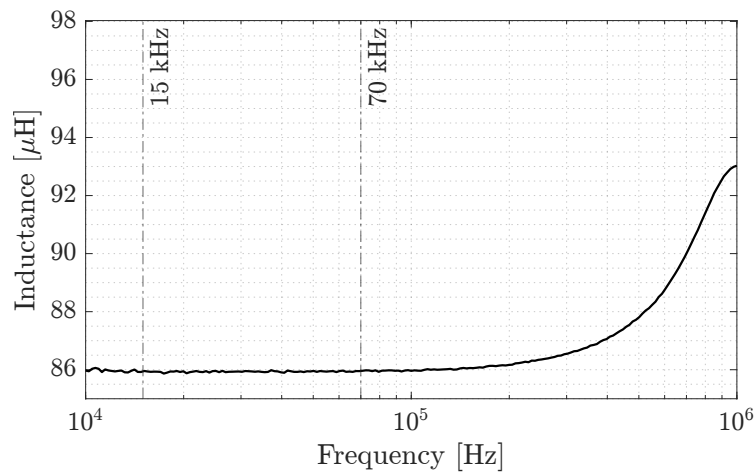
The design methodology for the magnetics in the DAB converter, as outlined in Chapter 3, was implemented. Both the inductor and transformer utilize the same set of

materials for construction, as specified in Table 4.2. The ferrite cores E80/38/20 employed in this design possess specific characteristics detailed in references [49] and [50].

### 5.2.1 Inductor Design

The inductance of the DAB converter, denoted as  $L_{\text{dab}}$ , is attained by employing 14 turns of litz wire 392x37AWG wound around the core with an air gap ( $l_g$ ) of 0.52 mm. The impedance of the inductor was measured using the Agilent 4294A impedance analyzer, and the obtained result is depicted in Figure 5.1.

**Figure 5.1** – Inductor impedance analyser.

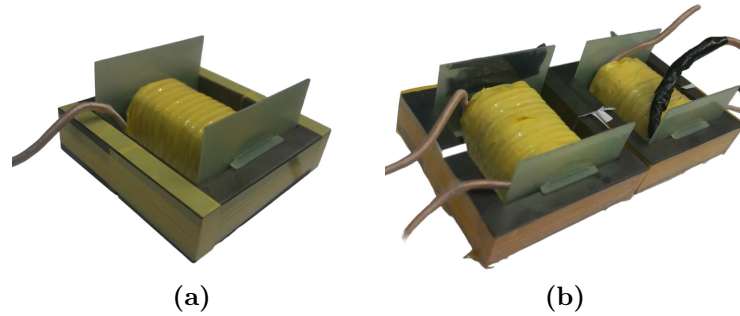


Note. Own authorship.

The inductance achieved, ranging from 15 kHz to 70 kHz, corresponding to the operational frequency of the converter, measures  $85.93 \mu\text{H}$ . The constructed inductor is visible in Figure 5.2.

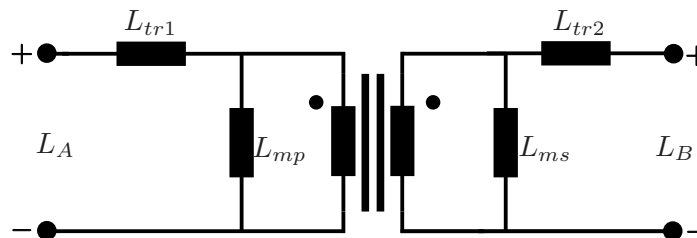
### 5.2.2 Transformer Design

The transformer was constructed using 14 turns of litz wire in the primary side and 12 turns in the secondary. Although no gap was considered during the optimization, a minimum gap of 0.2 mm was included in each transformer as a precaution against core saturation. The constructed transformers are depicted in Figure 5.2b.

**Figure 5.2** – Assembled magnetics: (a) inductor; (b) transformers.

Note. Own authorship.

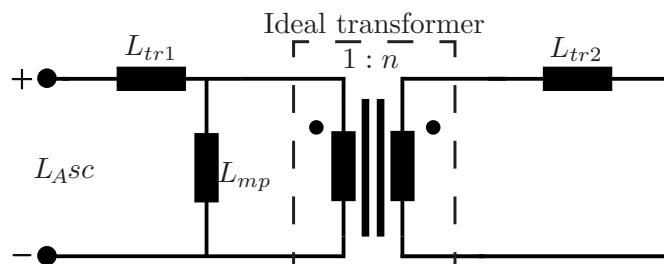
The leakage and magnetizing inductance of the transformers can be calculated by comparing the ideal model of the transformer with the measured total impedance of both the primary and secondary sides. This comparison is done with each side of the transformer measured individually while the opposite side is short-circuited, as illustrated in Figure 5.3 for the open-circuit model and Figure 5.4 for the short-circuit model.

**Figure 5.3** – Model transformer.

Note. Own authorship.

In the Figure 5.3 the equation for the transformer model can be defined as,

$$\begin{cases} L_A = L_{tr1} + L_{mp}, \\ or \\ L_B = L_{tr2} + L_{ms} \end{cases} \quad (5.1)$$

**Figure 5.4** – Leakage inductance characterization.

Note. Own authorship.



While for the Figure 5.4 the equation for the transformer when considering it referred to the secondary can be defined as

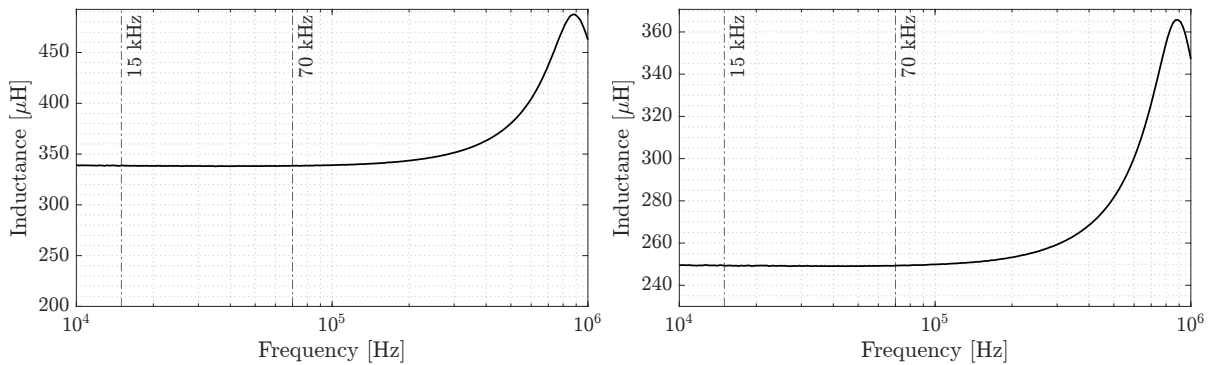
$$L_{ASC} = L_{tr1} + \frac{L_A \cdot L_{tr2} \cdot n^2}{L_A + L_{tr2} \cdot n^2} \quad (5.2)$$

when considering it referred to the primary, the value for  $L_{BSC}$  can be acquired.

With the equations described above, using the impedance analyser Agilent 4294A the values for  $L_A$ ,  $L_B$ ,  $L_{ASC}$  and  $L_{BSC}$  are acquired .

For the first transformer the measurements are:

**Figure 5.5** – Measured inductances transformer I primary and secondary.



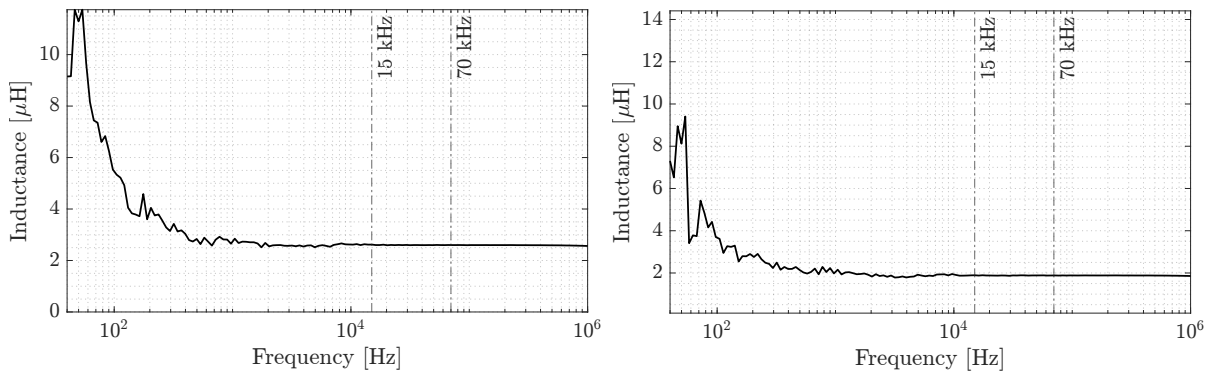
(a) Measured total inductance of the primary side. (b) Measured total inductance secondary side.

Note. Own authorship.

where the values obtained for the range of operation for  $L_A$  and  $L_B$  are,

$$\begin{cases} L_A = 338.5 \mu H \\ \text{and} \\ L_B = 249.1 \mu H \end{cases} \quad (5.3)$$

**Figure 5.6** – Measured total inductance transformer I while the opposing side is short-circuited.



(a) Measured total inductance referred to the secondary side. (b) Measured total inductance referred to the primary side.

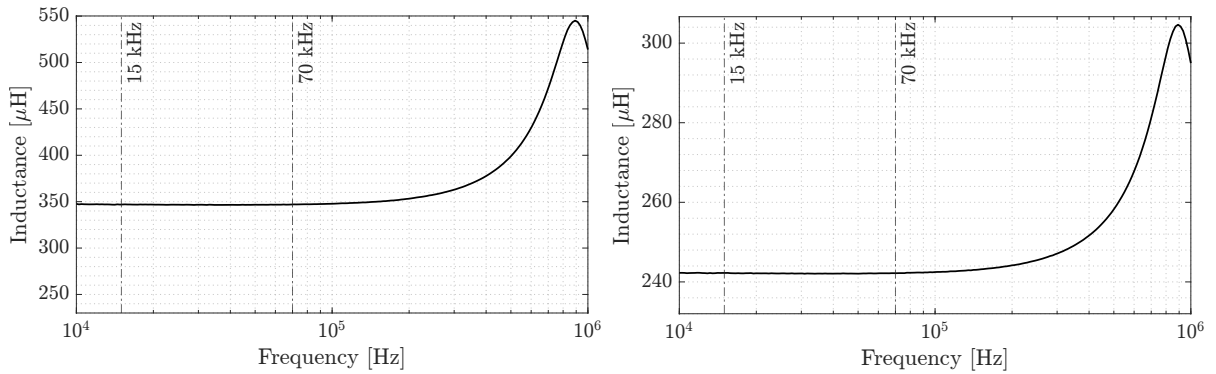
Note. Own authorship.

where the values obtained for the range of operation for  $L_A$  and  $L_B$  are,

$$\begin{cases} L_{ASC} = 2.7 \mu H \\ \text{and} \\ L_{BSC} = 1.9 \mu H \end{cases} \quad (5.4)$$

For the second transformer the measurements are:

**Figure 5.7** – Measured inductances transformer II primary and secondary.

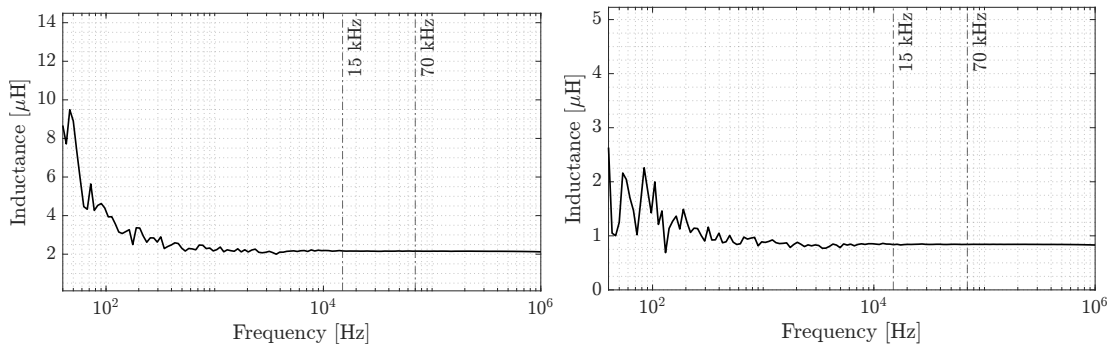


(a) Measured total inductance of the primary side. (b) Measured total inductance secondary side.

Note. Own authorship.

$$\begin{cases} L_A = 346.1 \mu H \\ \text{and} \\ L_B = 255.3 \mu H \end{cases} \quad (5.5)$$

**Figure 5.8** – Measured total inductance transformer II.



(a) Measured total inductance referred to the secondary side. (b) Measured total inductance referred to the primary side is short-circuited.

Note. Own authorship.

$$\begin{cases} L_{ASC} = 2.2 \mu H \\ \text{and} \\ L_{BSC} = 1.7 \mu H \end{cases} \quad (5.6)$$

By manipulating equations 5.1 and 5.2, the values for the magnetizing and leakage inductance for both transformers can be acquired. These values are respectively presented as follows: the leakage inductance for the first transformer ( $L_{tr1}$ ), the magnetizing inductance for the first transformer ( $L_{mag1}$ ), the leakage inductance for the second transformer ( $L_{tr2}$ ), and the magnetizing inductance for the second transformer ( $L_{mag2}$ ).

$$\begin{cases} L_{tr1} = 1.6 \mu H \\ L_{mag1} = 336 \mu H \\ L_{tr2} = 1.0 \mu H \\ L_{mag2} = 345 \mu H. \end{cases} \quad (5.7)$$

### 5.3 TRANSISTORS

The transistors utilized in this study are the C3M00751520K from Wolfspeed, featuring 3rd generation Silicon Carbide (SiC) MOSFET technology. The gate driver employed was developed according to specifications outlined in [51]. For switch control, a Texas Instruments microcontroller, specifically the LAUNCHXL-F280049C launchpad, was utilized, a common choice for power electronics applications [52].

Considering the rise time, fall time, turn-on, and turn-off delay time as specified in the manufacturer's datasheet for the MOSFET C3M00751520K [53], alongside a safety margin, the dead time defined for the switches amounts to 250 ns.

### 5.4 EXPERIMENTAL RESULTS

The experimental tests were conducted by cycling through each of the  $i$  points, as outlined in Table 5.2. All tests maintained a consistent input voltage of 400V, with the sole variation being in the phase shift angle ( $\phi$ ) and the operating frequency. These adjustments aimed to achieve the designated voltage output and power output for the converter while optimizing efficiency.

To measure the power processed by the converter, a wattmeter was utilized. Additionally, an oscilloscope was employed to monitor voltage and current levels across the transformer's primary and secondary sides, thereby ensuring the functionality and performance of each component within the converter.

**Table 5.2** – Converter’s testing parameters configuration.

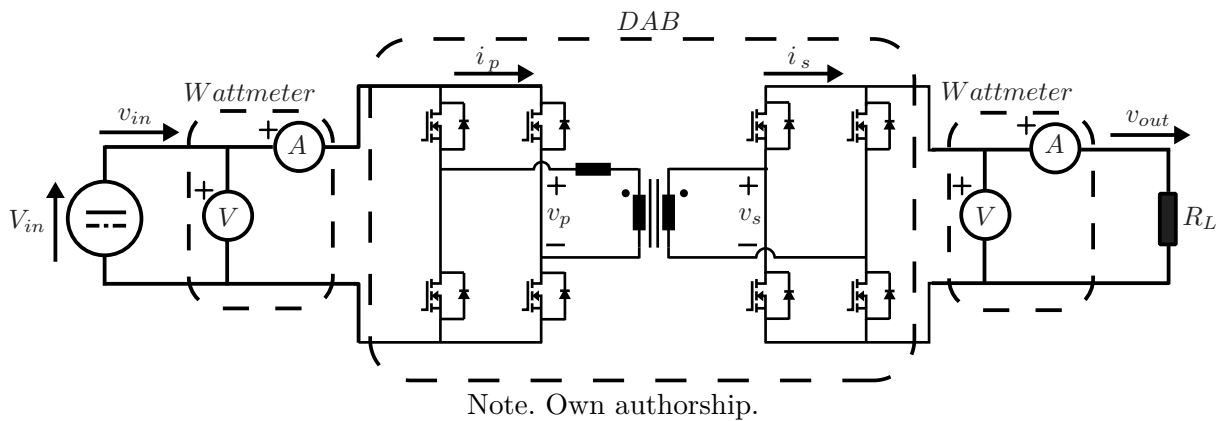
| Point | Design inputs |             |        | Design outputs |            |
|-------|---------------|-------------|--------|----------------|------------|
|       | $V_i$ [V]     | $f_s$ [kHz] | $\phi$ | $V_o$ [V]      | $P_o$ [kW] |
| i = 1 | 400           | 30.91       | 15.22  | 300            | 2          |
| i = 2 | 400           | 34.01       | 14.28  | 350            | 2          |
| i = 3 | 400           | 43.05       | 15.98  | 400            | 2          |
| i = 4 | 400           | 61.54       | 20.94  | 450            | 2          |

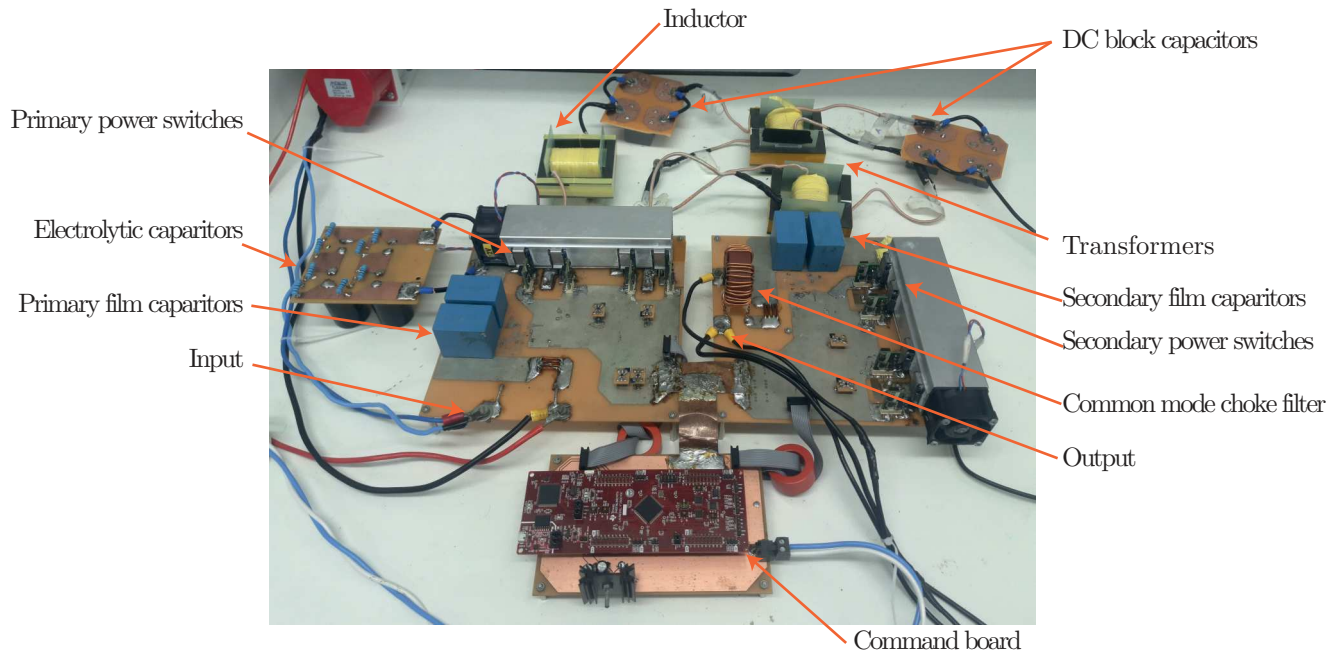
Note. Own authorship.

### 5.4.1 DAB test setup

The setup, as illustrated in the schematic in Figure 5.9, included a TS500-40 Programmable DC Power Supply serving as the voltage source ( $V_{in}$ ) for the DAB converter. A resistive load ( $R_L$ ) was connected at the converter’s output to facilitate the measurement of input and output voltage, current, and power. The Yokogawa WT1800 precision power analyzer served to measure these parameters at designated points.

To assess the transformer’s primary and secondary, an oscilloscope was linked to the output of the primary bridge and the input of the secondary bridge. Specifically, a Tektronix MSO 3040 oscilloscope was employed for this purpose. The physical prototype assembly is depicted in Figure 5.10.

**Figure 5.9** – DAB test setup schematic.

**Figure 5.10** – DAB converter prototype.

Note. Own authorship.

further specifications and about the prototype construction are detailed in the Appendix A.

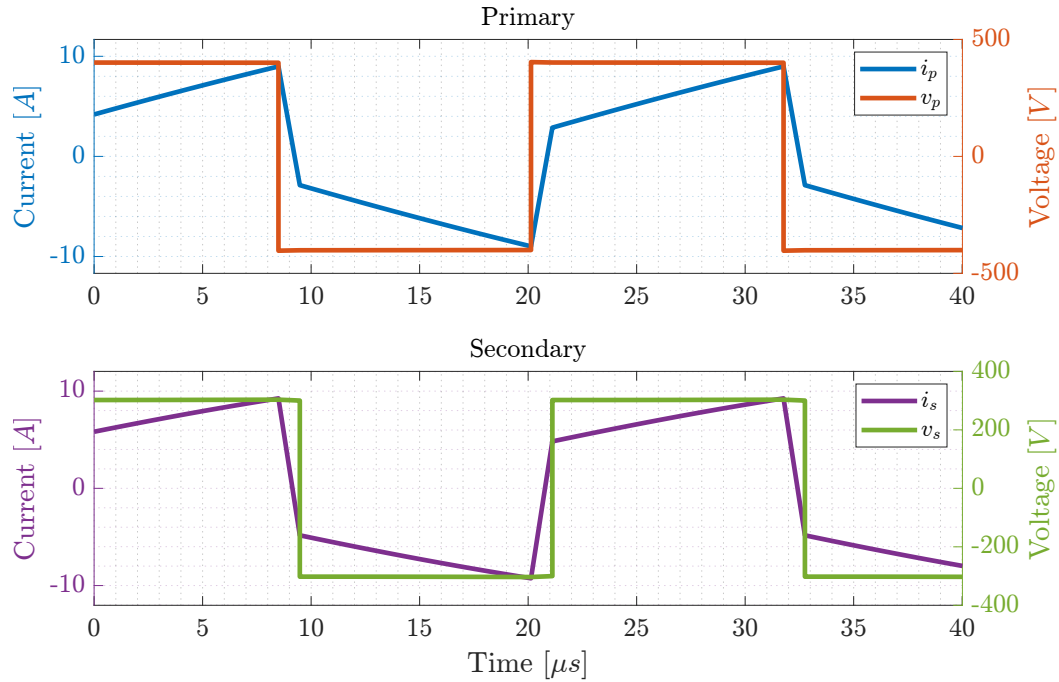
#### 5.4.2 Efficiency Comparison

It is in the subsequent sections that the results of each tested point are delineated. The comparison encapsulates theoretical values derived from optimization, simulation results, and, lastly, experimental findings obtained through the aforementioned testing setup.

##### 5.4.2.1 Experimental results - 300 V

It was noted during the testing of operation point  $i = 1$ , aiming for a power output of 2 kW and 300 V, that a resistive load of  $45 \Omega$  would have been ideal. Due to constraints, a slightly higher resistive load of  $48 \Omega$  was used, leading to minor discrepancies in the results. The findings depicted in Figure 5.11 and detailed in Table 5.3 were obtained through PLECS simulation, whereas the experimental data is illustrated in Figures 5.13 and 5.12.

Figure 5.11 showcases waveforms of current and voltage for both primary and secondary sides of the converter. On the primary side, a peak current of 8.98 A was observed alongside voltage fluctuations ranging from 400 V to -400 V. Conversely, the secondary side displayed a peak current of 9.25 A and voltage levels oscillating between 302 V to -302 V.

**Figure 5.11** – Converter’s primary and secondary waveforms in PLECS simulation - 300 V.

Note. Own authorship.

The overall outcomes of the converter operation during simulation are delineated in Table 5.3. Here, the converter received inputs of 400 V, 2099 W, and 5.24 A, yielding outputs of 302.62 V, 2035 W, and 6.72 A. The table exclusively accounts for losses stemming from the switches, totaling 16.34 W.

**Table 5.3** – 300 V PLECS simulation results.

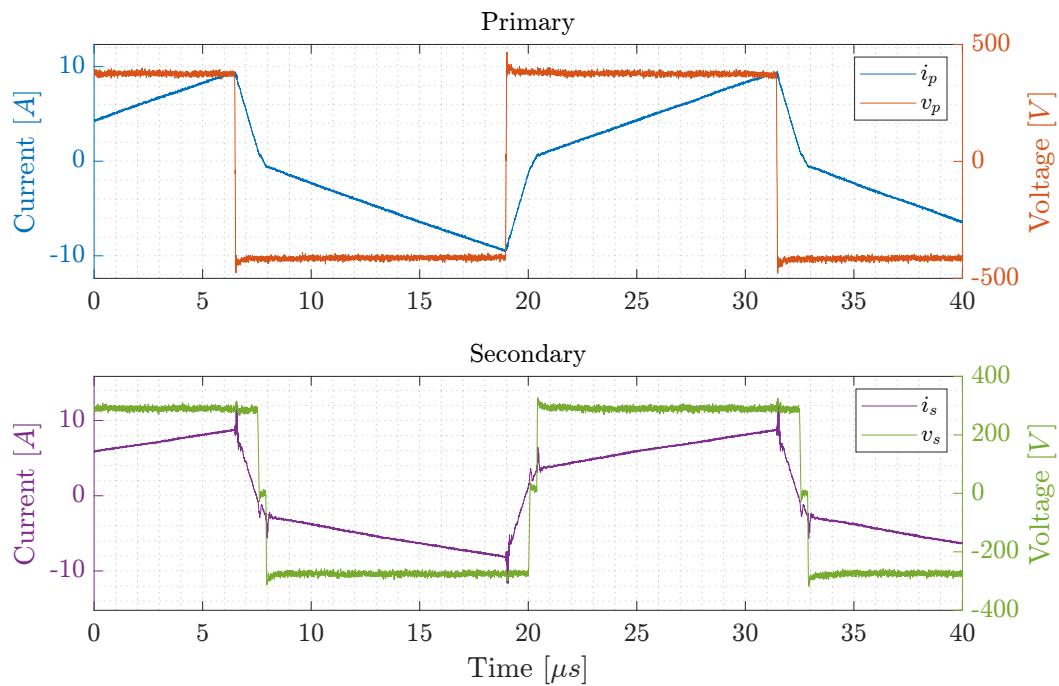
| Parameter         | Result     |
|-------------------|------------|
| $V_{inRMS}$       | 400 [V]    |
| $I_{inRMS}$       | 5.24 [A]   |
| $P_{in}$          | 2099 [W]   |
| $V_{outRMS}$      | 302.62 [V] |
| $I_{outRMS}$      | 6.72 [A]   |
| $P_{out}$         | 2035 [W]   |
| $\eta$            | 99.22 [%]  |
| $LOSS_{switches}$ | 16.34 [W]  |

Note. Own authorship.

In Figure 5.12, the waveforms depicting current and voltage on the primary and secondary sides of the converter during the experimental tests are presented. The peak current observed on the primary side is 9.40 A, accompanied by overvoltage peaking at 446 V at the initiation of a new operational cycle.

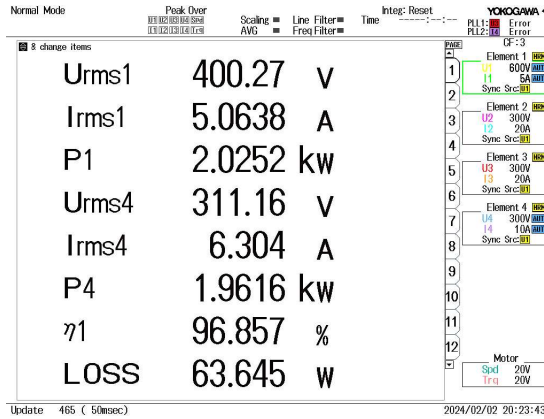
On the secondary side, conspicuous peaks of overcurrent and overvoltage are apparent whenever a switch transitions, with the current reaching a peak of 12.08 A and the voltage cresting at 317.95 V. Furthermore, a discernible effect of the converter's dead time is noticeable on the secondary side, wherein the voltage level briefly drops to zero during these intervals. This phenomenon is not as pronounced on the primary side due to the presence of the inductor and the capacitance of the switches, which discharge during the dead time, thus maintaining the voltage level on the primary side.

**Figure 5.12** – Converter's primary and secondary waveforms - 300 V.



Note. Own authorship.

The results obtained from the wattmeter are depicted in Figure 5.13. The converter inputs were 400 V, 2 kW, and 5.06 A, while the outputs were 316.16 V, 1.96 kW, and 6.03 A. The total losses incurred by the converter amounted to 63.64 W, resulting in an efficiency of 96.85%.

**Figure 5.13** – 300 V wattmeter results.

Note. Own authorship.

Table 5.4 provides a comparison between the theoretical, simulation, and experimental results of the designed converter, including the percentage error ( $Err\%$ ) between the theoretical and experimental outcomes. The total losses and efficiency of the converter during the simulation results are not included at this time.

**Table 5.4** – 300 V Results comparison

|                  | Theoretical | Simulation | Experimental | Err [%] |
|------------------|-------------|------------|--------------|---------|
| $V_{out}rms$ [V] | 300         | 302.62     | 311.16       | 3.72    |
| $I_{out}rms$ [A] | 6.66        | 6.72       | 6.30         | 5.40    |
| $P_{out}$ [W]    | 2000        | 2099       | 1961         | 1.95    |
| Loss [W]         | 55.83       | -          | 63.64        | 13.98   |
| $\eta$ [%]       | 97.20       | -          | 96.85        | 0.36    |

Note. Own authorship.

Comparing the theoretical, simulation, and experimental results of the DAB converter operating at a voltage output of 300 V, it is evident that the waveforms observed during experimental tests maintain the expected characteristics when compared with the simulation. However, there are noticeable spikes in voltage and current during switching events in the experimental results. To mitigate this issue, improvements to the layout of the converter may be necessary.

Despite these spikes, the efficiency and losses of the converter at this configuration are satisfactory, as they remain close to the theoretical expectations. The percentage error of the results is low, indicating a reliable performance of the converter under these operating conditions.

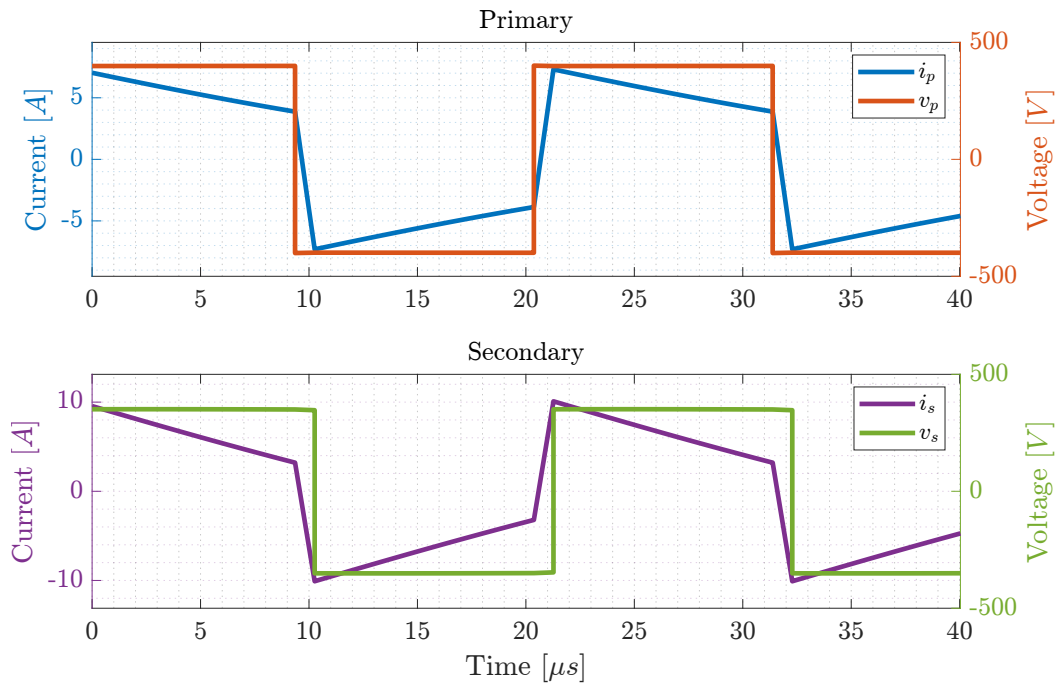


## 5.4.2.2 Experimental results - 350 V

The operation point  $i = 2$  necessitated a resistive load of  $61.5 \Omega$  to achieve a power output of 2 kW and 350 V. The simulation results depicted in Figure 5.14 and Table 5.5, along with the experimental results showcased in Figures 5.16 and 5.15, offer a comprehensive comparison.

Figure 5.14 illustrates the waveforms of current and voltage for both primary and secondary sides of the converter. On the primary side, a peak current of 7.38 A was observed, with voltage levels ranging from 400 V to -400 V. Conversely, the secondary side exhibited a peak current of 10.08 A, with voltage levels varying from 357 V to -357 V.

**Figure 5.14** – Converter’s primary and secondary waveforms in PLECS simulation - 350 V.



Note. Own authorship.

The overall results of the converter operation during simulation are detailed in Table 5.5. For the input parameters of 400 V, 2086 W, and 5.21 A, the converter produced outputs of 353.67 V, 2033 W, and 5.75 A. Notably, the losses from the switches totaled 15.10 W.

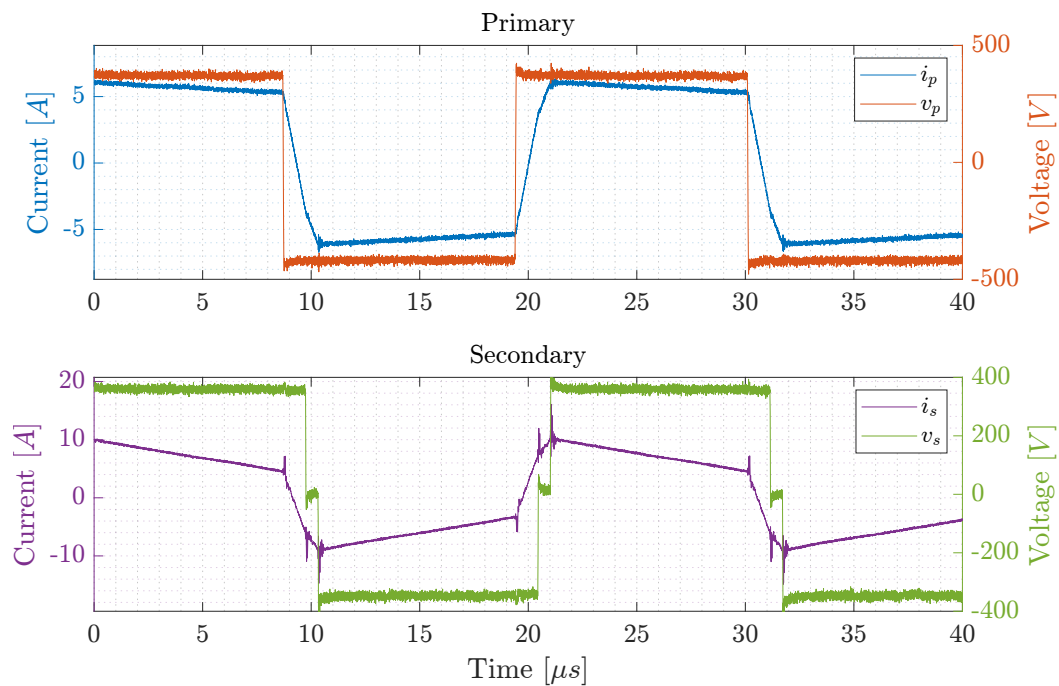
**Table 5.5** – 350 V PLECS simulation results.

| Parameter         | Result     |
|-------------------|------------|
| $V_{inRMS}$       | 400 [V]    |
| $I_{inRMS}$       | 5.21 [A]   |
| $P_{in}$          | 2086 [W]   |
| $V_{outRMS}$      | 353.67 [V] |
| $I_{outRMS}$      | 5.75 [A]   |
| $P_{out}$         | 2033 [W]   |
| $\eta$            | 99.28 [%]  |
| $LOSS_{switches}$ | 15.10 [W]  |

Note. Own authorship.

The Figure 5.15 illustrates the waveforms depicting current and voltage on both the primary and secondary sides of the converter during experimental tests. The primary side exhibited a peak current of 6.81 A, accompanied by an overvoltage peaking at 421.95 V during the initiation of a new operational cycle.

Meanwhile, on the secondary side, notable peaks of overcurrent and overvoltage were observed during each switching event, with the current spiking at 16.07 A and the voltage reaching a peak of 447.96 V. Similar to the previous test, there were transient periods where the voltage level dropped to zero momentarily on the secondary side.

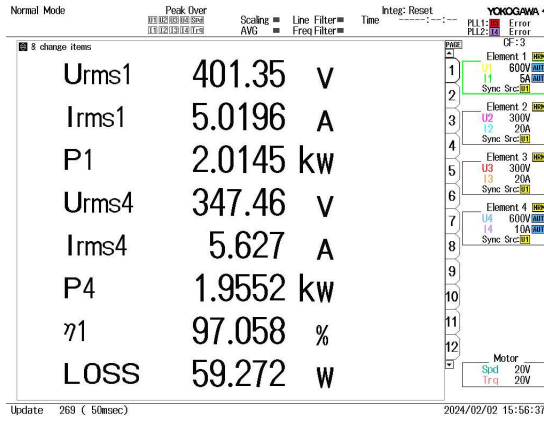
**Figure 5.15** – Converter's primary and secondary waveforms - 350 V.

Note. Own authorship.

The Figure 5.16 presents the results derived from the wattmeter during testing, with

the converter input parameters set at 401 V, 2 kW, and 5.01 A. Conversely, the converter output metrics registered 347.46 V, 1.95 kW, and 5.6 A, with total losses amounting to 59.27 W and an efficiency rating of 97.05 %.

**Figure 5.16** – 350 V wattmeter results.



Note. Own authorship.

The Table 5.6 facilitates a comparative analysis among the theoretical, simulation, and experimental outcomes of the designed converter, inclusive of the percentage error ( $Err\%$ ) calculated between the theoretical and experimental results. It's important to note that the total losses and efficiency of the converter during the simulation phase are not included in this comparison at the moment.

**Table 5.6** – 350 V Results comparison

|                  | Theoretical | Simulation | Experimental | Err [%] |
|------------------|-------------|------------|--------------|---------|
| $V_{out}rms$ [V] | 350         | 353.67     | 347.46       | 0.72    |
| $I_{out}rms$ [A] | 5.71        | 5.75       | 5.62         | 1.57    |
| $P_{out}$ [W]    | 2000        | 2033       | 1955         | 2.25    |
| Loss [W]         | 52.97       | -          | 59.27        | 11.89   |
| η [%]            | 97.35       | -          | 97.27        | 0.08    |

Note. Own authorship.

The comparison among the theoretical, simulation, and experimental results of the DAB converter with a voltage output of 350 V reveals that the waveforms observed during the experimental tests align well with the expected characteristics derived from the simulation. Despite encountering similar phenomena observed in previous tests, such as voltage and current spikes during switching, the converter's performance remains consistent.

The efficiency and losses of the converter at this operational point are notably satisfactory and meet the anticipated outcomes, as indicated by the low error margin

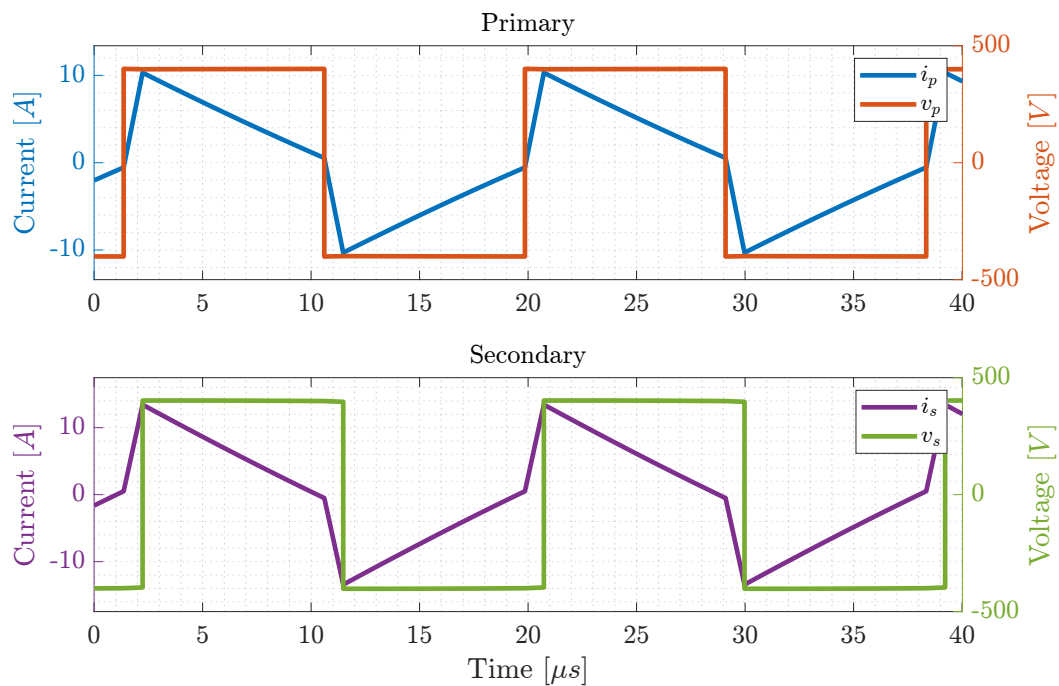
in the results. Additionally, it's worth noting that this particular operational point has yielded the best results among all the tests conducted in the present study.

#### 5.4.2.3 Experimental results - 400 V

During the assessment of operation point  $i = 3$ , a power output of 2 kW and a voltage of 400 V necessitated a resistive load of 80  $\Omega$ . The simulation outcomes are delineated in Figure 5.17 and Table 5.7, while the experimental findings are depicted in Figures 5.19 and 5.18.

Figure 5.17 provides an overview of the current and voltage waveforms for both the primary and secondary sides of the converter. On the primary side, a peak current of 9.95 A was observed, with voltage levels fluctuating between 400 V and -400 V. Conversely, the secondary side exhibited a peak current of 13.01 A, with voltage levels ranging from 405 V to -405 V.

**Figure 5.17** – Converter's primary and secondary waveforms in PLECS simulation - 400 V.



Note. Own authorship.

The Table 5.7 delineates the comprehensive outcomes of the converter's operation during simulation. For this scenario, the converter inputs were set at 400 V, 2066 W, and 5.16 A, while the outputs measured 401.13 V, 2011 W, and 5.01 A. Notably, the table accounts solely for losses attributed to the switches, totaling 17.13 W.

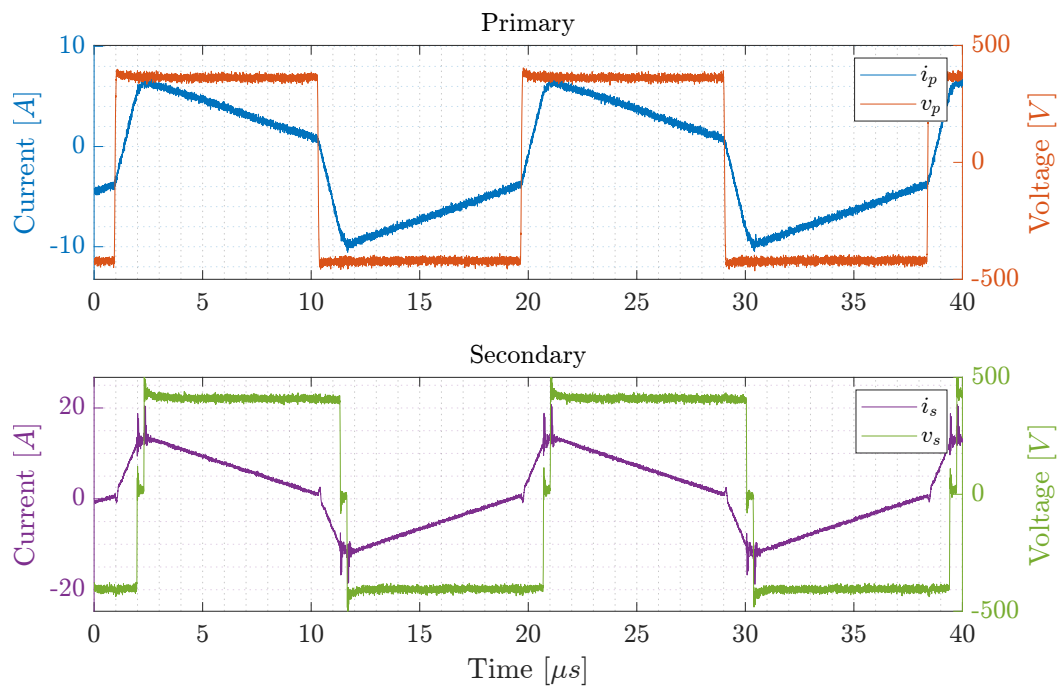
**Table 5.7** – 400 V PLECS simulation results.

| Parameter         | Result     |
|-------------------|------------|
| $V_{inRMS}$       | 400 [V]    |
| $I_{inRMS}$       | 5.16 [A]   |
| $P_{in}$          | 2066 [W]   |
| $V_{outRMS}$      | 401.13 [V] |
| $I_{outRMS}$      | 5.01 [A]   |
| $P_{out}$         | 2011 [W]   |
| $\eta$            | 99.15 [%]  |
| $LOSS_{switches}$ | 17.13 [W]  |

Note. Own authorship.

In Figure 5.18, the waveforms for current and voltage on both the primary and secondary sides of the converter during experimental tests are presented. It is notable that the peak current observed is 7.07 A on the primary side, accompanied by voltage levels peaking at 403 V at the beginning of a new operational cycle.

Conversely, the secondary side exhibits noticeable peaks of overcurrent and overvoltage during switching events, with the current reaching a peak of 20.79 A and the voltage peaking at 519.97 V. Similar to previous tests, there is a brief period where the voltage level remains at zero on the secondary side.

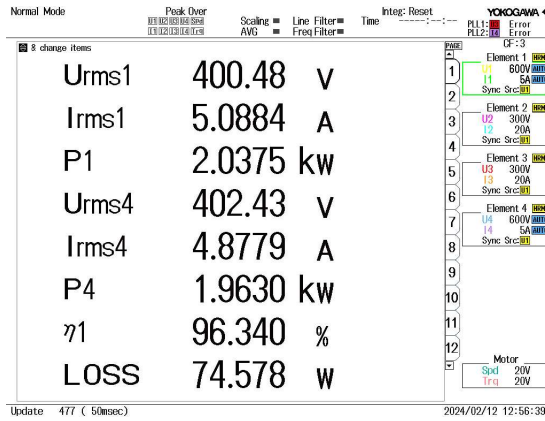
**Figure 5.18** – Converter's primary and secondary waveforms - 400 V.

Note. Own authorship.

The results obtained from the wattmeter, as depicted in Figure 5.19, reveal that the

converter operated with inputs of 400 V, 2 kW, and 5.08 A. Correspondingly, the converter outputs were measured at 402.43 V, 1.96 kW, and 4.8 A. The total losses incurred by the converter amounted to 74.57 W, resulting in an efficiency of 96.34%.

**Figure 5.19** – 400 V wattmeter results.



Note. Own authorship.

In the Table 5.8 it is possible to compare the experimental results with the design results and the percentage error ( $Err\%$ ) between values.

**Table 5.8** – 400 V Results comparison

|                  | Theoretical | Simulation | Experimental | Err [%] |
|------------------|-------------|------------|--------------|---------|
| $V_{out}rms$ [V] | 400         | 401.13     | 402.43       | 0.60    |
| $I_{out}rms$ [A] | 5.00        | 5.01       | 4.87         | 2.6     |
| $P_{out}$ [W]    | 2000        | 2011       | 1963         | 1.85    |
| Loss [W]         | 67.77       | -          | 74.57        | 10.03   |
| $\eta$ [%]       | 93.47       | -          | 96.34        | 3.07    |

Note. Own authorship.

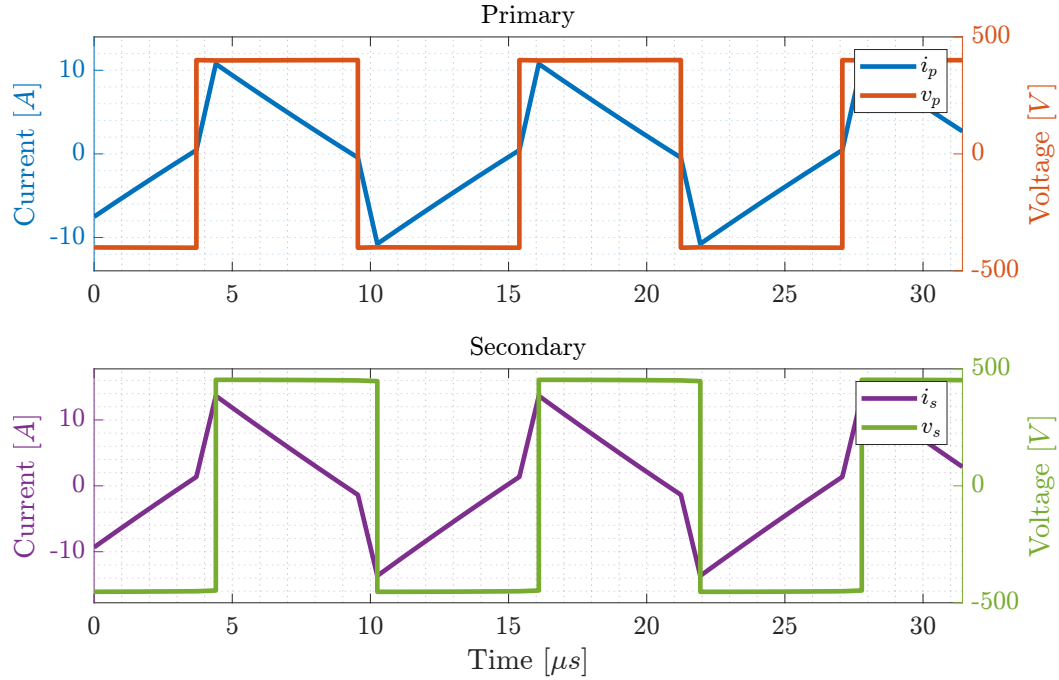
The findings from the DAB converter operating with a voltage output of 400 V indicate that the waveforms observed in the experimental tests align closely with the anticipated characteristics from the simulations. Despite recurring events similar to previous tests in the experimental data, such as spikes in voltage and current during switching, the converter's efficiency and losses persist at low levels, as observed in previous operating points. These results remain satisfactory and within the expected range.

#### 5.4.2.4 Experimental results - 450 V

When testing the final operation point  $i = 4$ , to achieve a power output of 2 kW and 450 V, a resistive load of  $101.25 \Omega$  was required. The simulation results are illustrated in Figure 5.20 and Table 5.9, while the experimental outcomes are depicted in Figures 5.22 and 5.21.

Figure 5.20 displays the waveforms of current and voltage for the primary and secondary sides of the converter. On the primary side, the peak current observed is 10.73 A, with voltage levels ranging from 400 V to -400 V. Conversely, on the secondary side, the peak current observed is 13.65 A, with voltage levels varying between 455 V and -455 V.

**Figure 5.20** – Converter’s primary and secondary waveforms in PLECS simulation - 450 V.



Note. Own authorship.

The Table 5.9 summarizes the comprehensive results of the converter operation during simulation. The converter inputs were 400 V, 2072 W, and 5.18 A, while the converter outputs were 451.83 V, 2016 W, and 4.46 A. The losses accounted for in this table pertain solely to the switches, amounting to 21.80 W.

**Table 5.9** – 450 V PLECS simulation results.

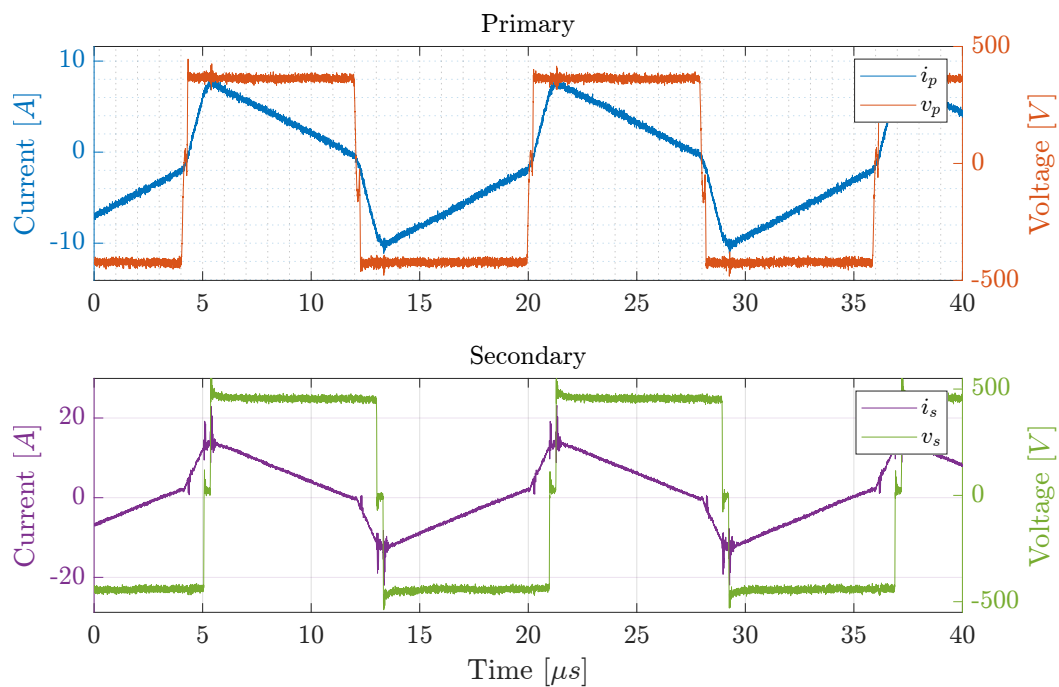
| Parameter         | Result |     |
|-------------------|--------|-----|
| $V_{in}RMS$       | 400    | [V] |
| $I_{in}RMS$       | 5.18   | [A] |
| $P_{in}$          | 2072   | [W] |
| $V_{out}RMS$      | 451.83 | [V] |
| $I_{out}RMS$      | 4.46   | [A] |
| $P_{out}$         | 2016   | [W] |
| $\eta$            | 98.95  | [%] |
| $LOSS_{switches}$ | 21.80  | [W] |

Note. Own authorship.

The Figure 5.21 depicts the waveforms of current and voltage on both the primary and secondary sides of the converter during experimental tests. Notably, a peak current of 8.51 A was observed on the primary side, accompanied by voltage levels reaching a peak of 445 V at the beginning of a new operational cycle. At this operational point, a distinct phenomenon is observed where the voltage levels on the primary side momentarily drop to zero, attributed to the dead time effect. It's important to highlight that at this specific operational point, the switching frequency is essentially twice that of the initial operational point. This implies reduced time for energy storage on the primary side, leading to an instant where no voltage is present.

Similarly, on the secondary side, peaks of overcurrent and overvoltage are evident during converter operation. The observed current peak is 23.15 A, and the voltage peak reaches 567.98 V. Once again, a brief period of zero voltage levels is observed on the secondary side, as seen in previous tests.

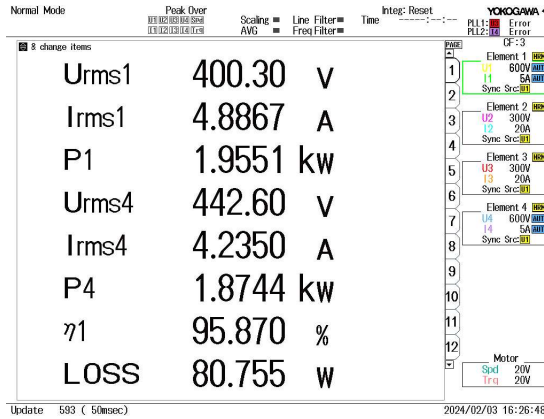
**Figure 5.21** – Converter's primary and secondary waveforms - 450 V.



Note. Own authorship.

The Figure 5.22 displays the results obtained from the wattmeter during testing, where the converter inputs comprised 400 V, 1.95 kW, and 4.88 A. Conversely, the converter outputs consisted of 442.60 V, 1.87 kW, and 4.23 A. The total losses of the converter were measured at 80.75 W, resulting in an efficiency of 95.87%.



**Figure 5.22** – 450 V wattmeter results.

Note. Own authorship.

In the Table 5.10 it is possible to compare the experimental results with the design results and the percentage error ( $Err\%$ ) between values.

**Table 5.10** – 450 V Results comparison

|                  | Theoretical | Simulation | Experimental | Err [%] |
|------------------|-------------|------------|--------------|---------|
| $V_{out}rms$ [V] | 450         | 451        | 442.60       | 1.64    |
| $I_{out}rms$ [A] | 4.44        | 5.18       | 4.23         | 4.72    |
| $P_{out}$ [W]    | 2000        | 2072       | 1874         | 6.3     |
| Loss [W]         | 93.47       | -          | 80.75        | 13.60   |
| $\eta$ [%]       | 95.32       | -          | 95.87        | 0.57    |

Note. Own authorship.

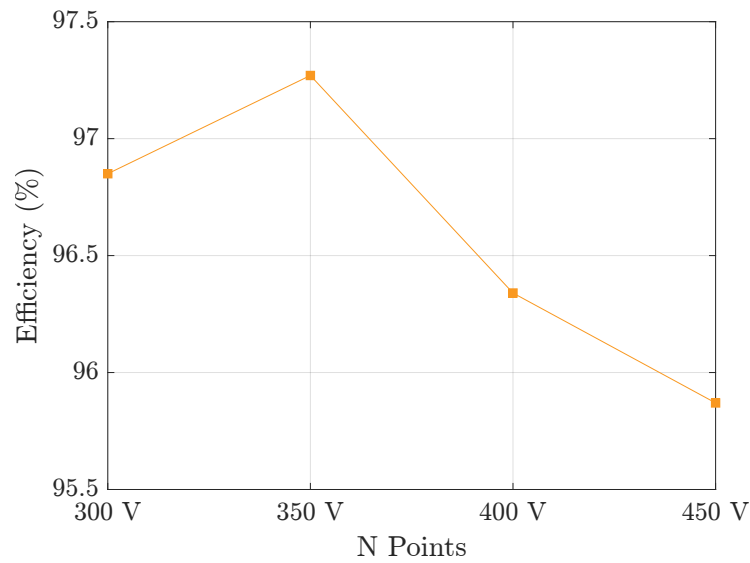
The results for the DAB converter with a voltage output of 450 V reveal that the waveforms in the experimental tests align with expectations compared to the simulation. However, similar to previous tests, there's an occurrence of the primary side voltage reaching zero at this operational point. Despite this, the overall efficiency and losses of the converter remain at low levels. It's noteworthy that this point represents the least optimized scenario, showcasing the lowest efficiency among all operational points tested. Nonetheless, the results are still deemed satisfactory and within the anticipated range based on prior expectations.

## 5.5 CONCLUSION

This chapter delves into the construction process of the DAB prototype, meticulously crafted through the PSO algorithm. It outlines the construction of its magnetic elements, offers insights into selected components, and elaborates on the assembly of the converter. Additionally, experimental results from the design, emphasizing variable frequency and phase shift, are presented.

The results obtained exhibit a minimal margin of error between the intended values and those observed in testing. Notably, the 350 V results showcase the highest efficiency, whereas the 450 V result represents the lowest. Nonetheless, all achieved outcomes are deemed satisfactory, meeting the objective of optimizing a converter for various operational points with different frequencies and phase shifts. Notably, each case demonstrates an efficiency exceeding 95% as can be observed in the Figure 5.23, underlining the success of the optimization approach employed.

**Figure 5.23** – Converter efficiency curve.



Note. Own authorship.

---

## Conclusion

At chapter 1 was introduced the IBDCs and its role at power electronics as a technology to improve sustainable energy generation and transmission throughout various applications, one such areas is on the electric vehicles charging systems. The OBCs can be employed at many applications aside of the from the vehicle charging, as V2G or V2H in moments were there is no need for use of the vehicles helping compensate the the intermittent nature of the renewable energy resources.

The chapter 2 explored the DAB converter, its working principle and, modulation technique and equations necessary for the design of the converter with the PSO algorithm.

As shown in the chapter 3 was presented the PSO algorithm, with its working principle and the main challenge of this methodology during the present study, that lies in the calculation of losses, and the unique construction characteristics of studied application. Nevertheless, the algorithm can be easily adapted since it has an modular structure so it can be used for the study of various converter topologies.

In the chapter 4 was introduced the operation points for which the converter would be optimized, a suitable voltage range and and power output was defined for use on a OBC, along with further configuration of the optimization process, based on the desired application. Furthermore, this methodology is not limited to this specific converter, it can be applied to other converters and application as well. As it operates on the principle of minimizing total losses in the studied converter.

Based on the obtained results presented on chapter 5, the effectiveness of the optimization process becomes evident as all obtained results were satisfactory. This iterative approach allows for the continuous refinement of the converter design, utilizing the available construction parameters to ensure the best possible assembly for optimization, suitable for an onboard charger application or any other application for an IBDC.

This study commenced with an introduction to Isolated Bidirectional DC-DC Converters and their significant role in improving sustainable energy generation and transmission across various applications, particularly in electric vehicle charging systems. OBCs were highlighted not only for vehicle charging but also for their potential in V2G

and V2H applications, demonstrating their ability to mitigate the intermittent nature of renewable energy sources.

The exploration of the DAB converter delved into its operating principles, modulation techniques, and the equations essential for its design using the PSO algorithm. This provided a comprehensive framework for optimizing the converter's performance, illustrating the theoretical underpinnings that guide practical implementations. The PSO algorithm was further elucidated, emphasizing its adaptability despite the challenges posed by loss calculations and unique construction characteristics. The algorithm's modular structure was showcased, underscoring its potential application to various converter topologies beyond the specific case studied.

Operation points for optimizing the converter established a suitable voltage range and power output for OBC applications. The flexibility of the optimization methodology was highlighted, demonstrating its applicability to different converters and applications by focusing on minimizing total losses. The results confirmed the effectiveness of this optimization process, with satisfactory outcomes across all tested scenarios. The iterative approach demonstrated how continuous refinement using available construction parameters could achieve optimal designs, making the methodology highly relevant for onboard chargers and other IBDC applications. The positive results underscore the potential for further advancements and optimizations in the field.

## 6.1 FUTURE WORKS

- Implement a closed loop control system to the converter;
- Optimize the system for the charging profile of commercially available battery packs;
- Reduce the size of the converter with planar magnetics and improved layout.
- Study the converter optimization under different modulation techniques such as dual phase shift.

---

## Bibliography

- [1] C. Liu, K. T. Chau, D. Wu, and S. Gao, “Opportunities and challenges of vehicle-to-home, vehicle-to-vehicle, and vehicle-to-grid technologies,” *Proceedings of the IEEE*, vol. 101, no. 11, pp. 2409–2427, 2013.
- [2] P. Kaloriya, N. Gupta, S. Vashisth, K. R. Niazi, and A. Swarnkar, “A new strategy for potential smart grids to alleviate heavy ev charging demand in residential areas,” in *2023 14th International Conference on Computing Communication and Networking Technologies (ICCCNT)*, pp. 1–6, 2023.
- [3] F. Rassaei, W.-S. Soh, and K.-C. Chua, “Demand response for residential electric vehicles with random usage patterns in smart grids,” *IEEE Transactions on Sustainable Energy*, vol. 6, no. 4, pp. 1367–1376, 2015.
- [4] D. Infield and L. Freris, *Renewable energy in power systems*. John Wiley & Sons, 2020.
- [5] J. Carrasco, L. Franquelo, J. Bialasiewicz, E. Galvan, R. PortilloGuisado, M. Prats, J. Leon, and N. Moreno-Alfonso, “Power-electronic systems for the grid integration of renewable energy sources: A survey,” *IEEE Transactions on Industrial Electronics*, vol. 53, no. 4, pp. 1002–1016, 2006.
- [6] X. Yu, C. Cecati, T. Dillon, and M. G. Simões, “The new frontier of smart grids,” *IEEE Industrial Electronics Magazine*, vol. 5, no. 3, pp. 49–63, 2011.
- [7] Y. Wang, Y. Guan, O. B. Fosso, M. Molinas, S.-Z. Chen, and Y. Zhang, “An input-voltage-sharing control strategy of input-series-output-parallel isolated bidirectional dc/dc converter for dc distribution network,” *IEEE Transactions on Power Electronics*, vol. 37, no. 2, pp. 1592–1604, 2022.
- [8] B. Zhao, Q. Song, J. Li, Q. Sun, and W. Liu, “Full-process operation, control, and experiments of modular high-frequency-link dc transformer based on dual active bridge for flexible mvdc distribution: A practical tutorial,” *IEEE Transactions on Power Electronics*, vol. 32, no. 9, pp. 6751–6766, 2017.

- [9] A. L. Kirsten *et al.*, *Metodologia de projeto do conversor DAB aplicado a transformadores de estado sólido*. PhD thesis, Universidade Federal de Santa Maria, 2014.
- [10] J. E. Huber and J. W. Kolar, “Applicability of solid-state transformers in today’s and future distribution grids,” *IEEE Transactions on Smart Grid*, vol. 10, no. 1, pp. 317–326, 2019.
- [11] D. Sha, Z. Guo, T. Luo, and X. Liao, “A general control strategy for input-series–output-series modular dc–dc converters,” *IEEE Transactions on Power Electronics*, vol. 29, no. 7, pp. 3766–3775, 2014.
- [12] Z. Guo, D. Sha, and K. Song, “Output-series connected dual active bridge converters for zero-voltage switching throughout full load range by employing auxiliary lc networks,” *IEEE Transactions on Power Electronics*, vol. 34, no. 6, pp. 5549–5562, 2019.
- [13] A. Mohammadpour, L. Parsa, M. H. Todorovic, R. Lai, R. Datta, and L. Garces, “Series-input parallel-output modular-phase dc–dc converter with soft-switching and high-frequency isolation,” *IEEE Transactions on Power Electronics*, vol. 31, no. 1, pp. 111–119, 2016.
- [14] W. Li, G. Joos, and C. Abbey, “A parallel bidirectional dc/dc converter topology for energy storage systems in wind applications,” in *2007 IEEE Industry Applications Annual Meeting*, pp. 179–185, 2007.
- [15] X. Shi, J. Jiang, and X. Guo, “An efficiency-optimized isolated bidirectional dc–dc converter with extended power range for energy storage systems in microgrids,” *Energies*, vol. 6, no. 1, pp. 27–44, 2013.
- [16] M. Safayatullah, M. T. Elrais, S. Ghosh, R. Rezaii, and I. Batarseh, “A comprehensive review of power converter topologies and control methods for electric vehicle fast charging applications,” *IEEE Access*, vol. 10, pp. 40753–40793, 2022.
- [17] D. Howell, S. Boyd, B. Cunningham, S. Gillard, L. Slezak, S. Ahmed, I. Bloom, A. Burnham, K. Hardy, A. Jansen, *et al.*, “Enabling extreme fast charging: A technology gap assessment,” 2017.
- [18] S. Rivera, S. Kouro, S. Vazquez, S. M. Goetz, R. Lizana, and E. Romero-Cadaval, “Electric vehicle charging infrastructure: From grid to battery,” *IEEE Industrial Electronics Magazine*, vol. 15, no. 2, pp. 37–51, 2021.
- [19] S. Kampl, “Topologies in on-board charging,” tech. rep., Infineon, 2020.

- [20] K. Fahem, D. E. Chariag, and L. Sbita, “On-board bidirectional battery chargers topologies for plug-in hybrid electric vehicles,” in *2017 International Conference on Green Energy Conversion Systems (GECS)*, pp. 1–6, 2017.
- [21] S. Balachandran and F. C. Lee, “Algorithms for power converter design optimization,” *IEEE Transactions on Aerospace and Electronic Systems*, vol. AES-17, no. 3, pp. 422–432, 1981.
- [22] Y. Xiao, Y. Wang, and Y. Sun, “Reactive power optimal control of a wind farm for minimizing collector system losses,” *Energies*, vol. 11, p. 3177, 11 2018.
- [23] L. Song, H. Ramakrishnan, N. Kumar, and M. Bhardwaj, “Bidirectional, dual active bridge reference design for level 3 electric vehicle charging stations,” Tech. Rep. tidues0c, Texas Instruments, Dallas, Texas, 2022.
- [24] F. Krismer, *Modeling and optimization of bidirectional dual active bridge DC-DC converter topologies*. Doctoral thesis, ETH Zurich, Zürich, 2010. Diss., Eidgenössische Technische Hochschule ETH Zürich, Nr. 19177, 2010.
- [25] R. De Doncker, D. Divan, and M. Kheraluwala, “A three-phase soft-switched high-power-density dc/dc converter for high-power applications,” *IEEE Transactions on Industry Applications*, vol. 27, no. 1, pp. 63–73, 1991.
- [26] M. Kheraluwala, R. Gascoigne, D. Divan, and E. Baumann, “Performance characterization of a high-power dual active bridge dc-to-dc converter,” *IEEE Transactions on Industry Applications*, vol. 28, no. 6, pp. 1294–1301, 1992.
- [27] F. Krismer and J. W. Kolar, “Accurate small-signal model for an automotive bidirectional dual active bridge converter,” in *2008 11th Workshop on Control and Modeling for Power Electronics*, pp. 1–10, 2008.
- [28] N. Noroozi, A. Emadi, and M. Narimani, “Performance evaluation of modulation techniques in single-phase dual active bridge converters,” *IEEE Open Journal of the Industrial Electronics Society*, vol. PP, pp. 1–1, 06 2021.
- [29] A. Rodríguez, A. Vázquez, D. G. Lamar, M. M. Hernando, and J. Sebastián, “Different purpose design strategies and techniques to improve the performance of a dual active bridge with phase-shift control,” *IEEE Transactions on Power Electronics*, vol. 30, no. 2, pp. 790–804, 2015.
- [30] J. Kennedy and R. Eberhart, “Particle swarm optimization,” in *Proceedings of ICNN’95 - International Conference on Neural Networks*, vol. 4, pp. 1942–1948 vol.4, 1995.

- [31] K. E. Parsopoulos and M. N. Vrahatis, *Particle swarm optimization and intelligence*. Advances in Computational Intelligence and Robotics, Hershey, PA: Information Science Reference, Mar. 2010.
- [32] C. Zhang, H. Shao, and Y. Li, "Particle swarm optimisation for evolving artificial neural network," in *Smc 2000 conference proceedings. 2000 ieee international conference on systems, man and cybernetics. 'cybernetics evolving to systems, humans, organizations, and their complex interactions' (cat. no.0*, vol. 4, pp. 2487–2490 vol.4, 2000.
- [33] Y. G. Petalas, K. E. Parsopoulos, and M. N. Vrahatis, "Entropy-based memetic particle swarm optimization for computing periodic orbits of nonlinear mappings," in *2007 IEEE Congress on Evolutionary Computation*, pp. 2040–2047, 2007.
- [34] H. Eskandari and C. D. Geiger, "Evolutionary multiobjective optimization in noisy problem environments," *Journal of Heuristics*, vol. 15, p. 559–595, June 2008.
- [35] J. Zhang, Y. Shi, and Z.-H. Zhan, "Power electronic circuits design: A particle swarm optimization approach," in *Simulated Evolution and Learning* (X. Li, M. Kirley, M. Zhang, D. Green, V. Ciesielski, H. Abbass, Z. Michalewicz, T. Hendtlass, K. Deb, K. C. Tan, J. Branke, and Y. Shi, eds.), (Berlin, Heidelberg), pp. 605–614, Springer Berlin Heidelberg, 2008.
- [36] B. Zhao, J. He, and X. Zhang, "Pso-algorithm-based optimal design of the lcllc resonant converters for space travelling-wave tube amplifiers applications," in *2019 IEEE 10th International Symposium on Power Electronics for Distributed Generation Systems (PEDG)*, pp. 520–523, 2019.
- [37] S. Varshney, L. Srivastava, and M. Pandit, "Comparison of pso models for optimal placement and sizing of statcom," in *International Conference on Sustainable Energy and Intelligent Systems (SEISCON 2011)*, pp. 346–351, 2011.
- [38] R. H. A. Hamid, A. M. A. Amin, R. S. Ahmed, and A. A. A. El-Gammal, "New technique for maximum efficiency and minimum operating cost of induction motors based on particle swarm optimization (pso)," in *2006 Eleventh International Middle East Power Systems Conference*, vol. 2, pp. 416–420, 2006.
- [39] *Transformer and Inductor Design Handbook, Fourth Edition*. CRC Press, Apr. 2011. ISBN 0-8247-5393-3.
- [40] C. P. Steinmetz, "On the law of hysteresis," *Proceedings of the IEEE*, vol. 72, pp. 197–221, 1984.
- [41] K. Venkatachalam, C. Sullivan, T. Abdallah, and H. Tacca, "Accurate prediction of ferrite core loss with nonsinusoidal waveforms using only steinmetz parameters,"



- in *2002 IEEE Workshop on Computers in Power Electronics, 2002. Proceedings.*, pp. 36–41, 2002.
- [42] W. Hurley and W. Wölflé, *Transformers and inductors for power electronics: theory, design and applications*. Hoboken, NJ: Wiley, 2013.
- [43] B. Bertoldi, “Systematic procedures for the design of passive components applied to a high performance three-phase rectifier,” 2021.
- [44] A. Dhole, S. K. Roy, and K. Basu, “Estimation and measurement of power loss in a high frequency inductor for a dab based dc-dc converter,” in *2021 National Power Electronics Conference (NPEC)*, pp. 1–6, 2021.
- [45] M. K. Kazimierczuk, “High-frequency magnetic components: Second edition,” *High-Frequency Magnetic Components: Second Edition*, pp. 1–729, 11 2013.
- [46] P. Dowell, “Effects of eddy currents in transformer windings,” in *Proceedings of the Institution of electrical Engineers*, vol. 113, pp. 1387–1394, IET, 1966.
- [47] S. Geng, M. Chu, W. Wang, P. Wan, X. Peng, H. Lu, and P. Li, “Modelling and optimization of winding resistance for litz wire inductors,” *IET Power Electronics*, vol. 14, no. 10, pp. 1834–1843, 2021.
- [48] D. C. MARTINS, “Transistores de potência,” *Edição dos autores*, p. 47, 2006.
- [49] TDK electronics, *Ferrites and acessórios, E80/38/20*, 10 2022.
- [50] TDK, *Ferrites and accessories, SIFERRIT material N87*, 2023.
- [51] L. M. Cúnico, “Estratégias de projeto e modulação para o conversor dab trifásico,” 2021.
- [52] D. Texas Instruments, “Tms320f28004x real-time microcontrollers technical reference manual.”
- [53] Wolfspeed, *C3M0075120K, 1200V 75mohm Silicon Carbide Power MOSFET*, 2023.
- [54] E. L. S. d. Silva *et al.*, “Modelagem e controle do conversor dual active bridge (dab),” 2019.

---

## DAB converter prototype

This appendix further outlines the design characteristics defined for the converter prototype, which was constructed to obtain the experimental results presented in this work.

### A.1 CAPACITORS

The capacitors of the DC buses, input and output, can be calculated by the equation A.1, by substituting the necessary values for the output or for the input when necessary [54], [9].

$$Bus_{Cap} = \frac{\phi \cdot P_o}{2 \cdot \pi \cdot f_s \cdot V_o^2 \cdot \Delta V_o \%} \quad (\text{A.1})$$

The DC block capacitors are introduced in order to prevent the transformer saturation due to unbalanced currents. This unbalanced currents can occur due to delays in gate drivers or other asymmetries during the start-up [23].

$$DC_{Cap} = \frac{100}{4 \cdot \pi^2 \cdot f_s^2 \cdot L} \quad (\text{A.2})$$

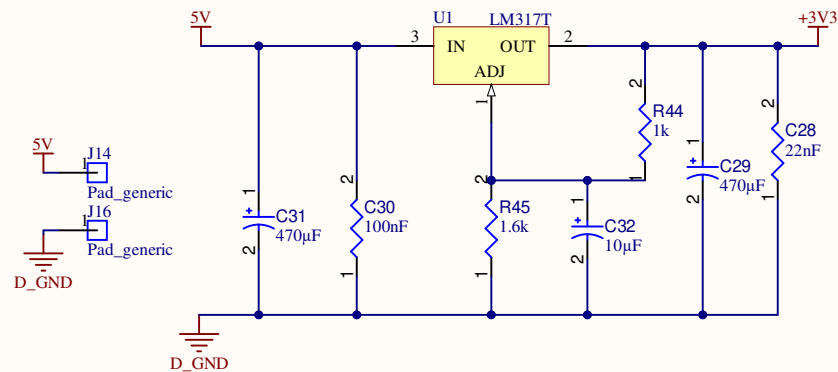
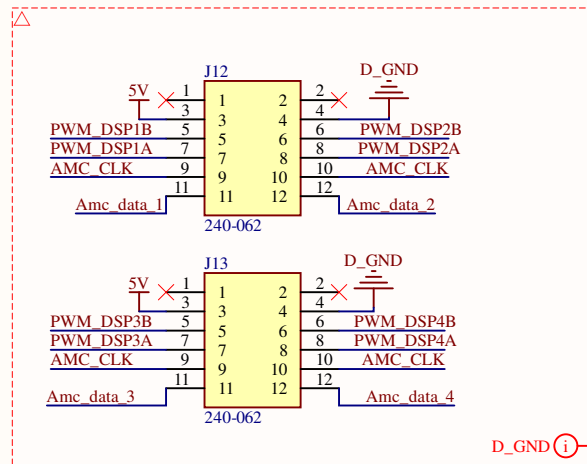
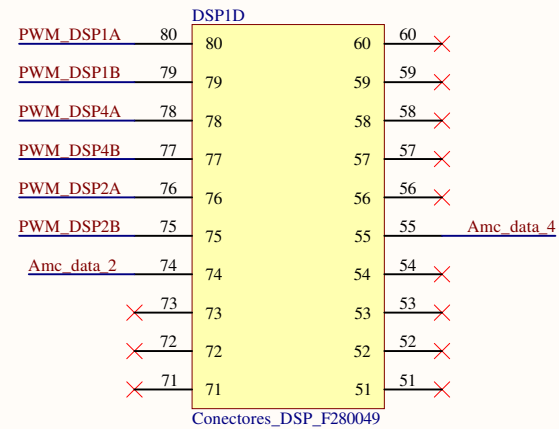
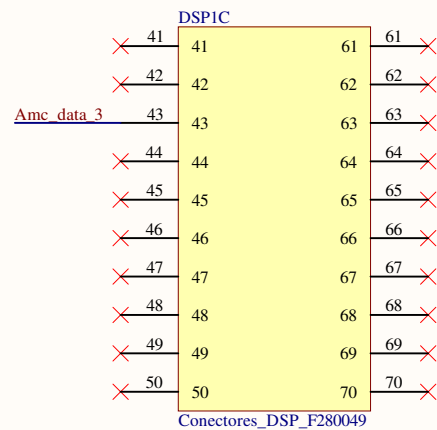
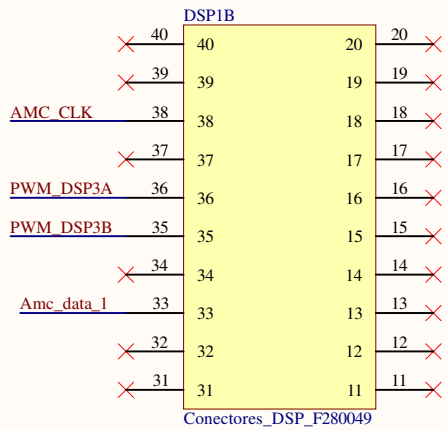
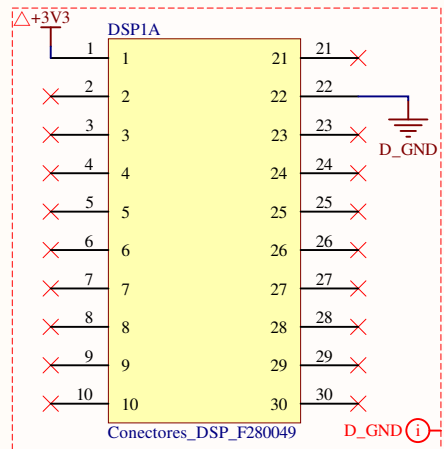
**Table A.1** – Capacitors.

| Parameter   | Code                    | Description        |
|-------------|-------------------------|--------------------|
| $Bus_{Cap}$ | EPCOS - M110165502 77E  | 800 V, 20 $\mu F$  |
| $DC_{Cap}$  | Kemmet - M1 QA11006 R75 | 160 V, 4.6 $\mu F$ |

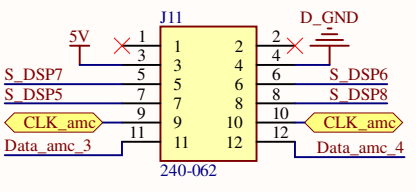
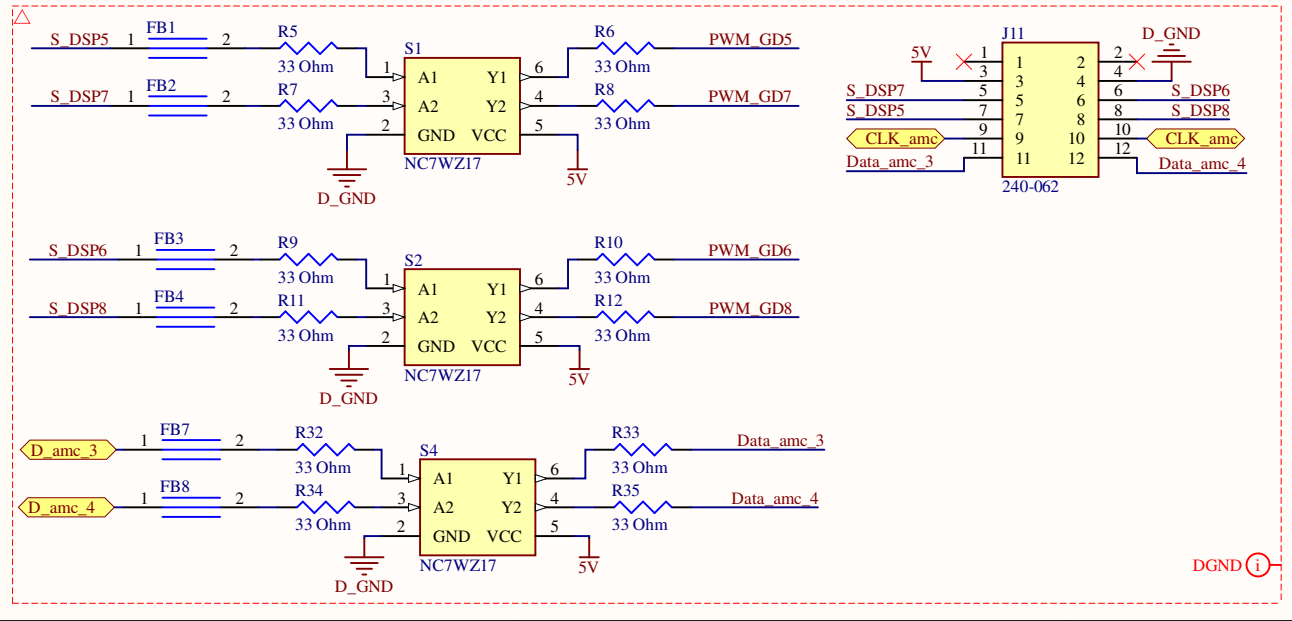
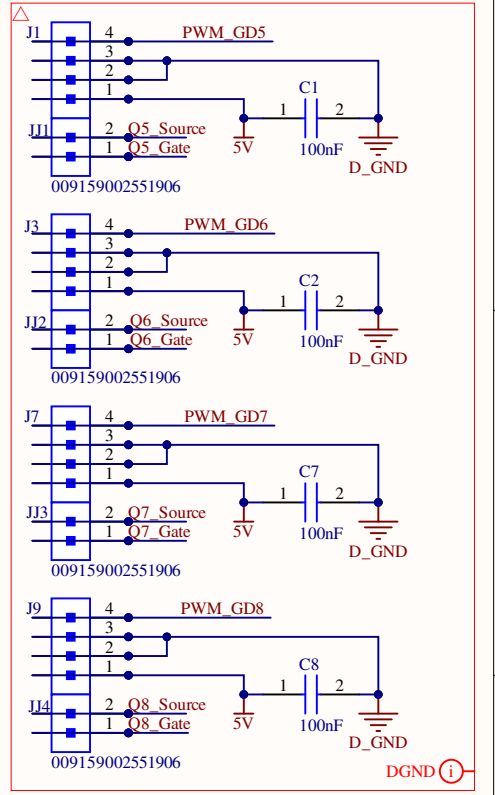
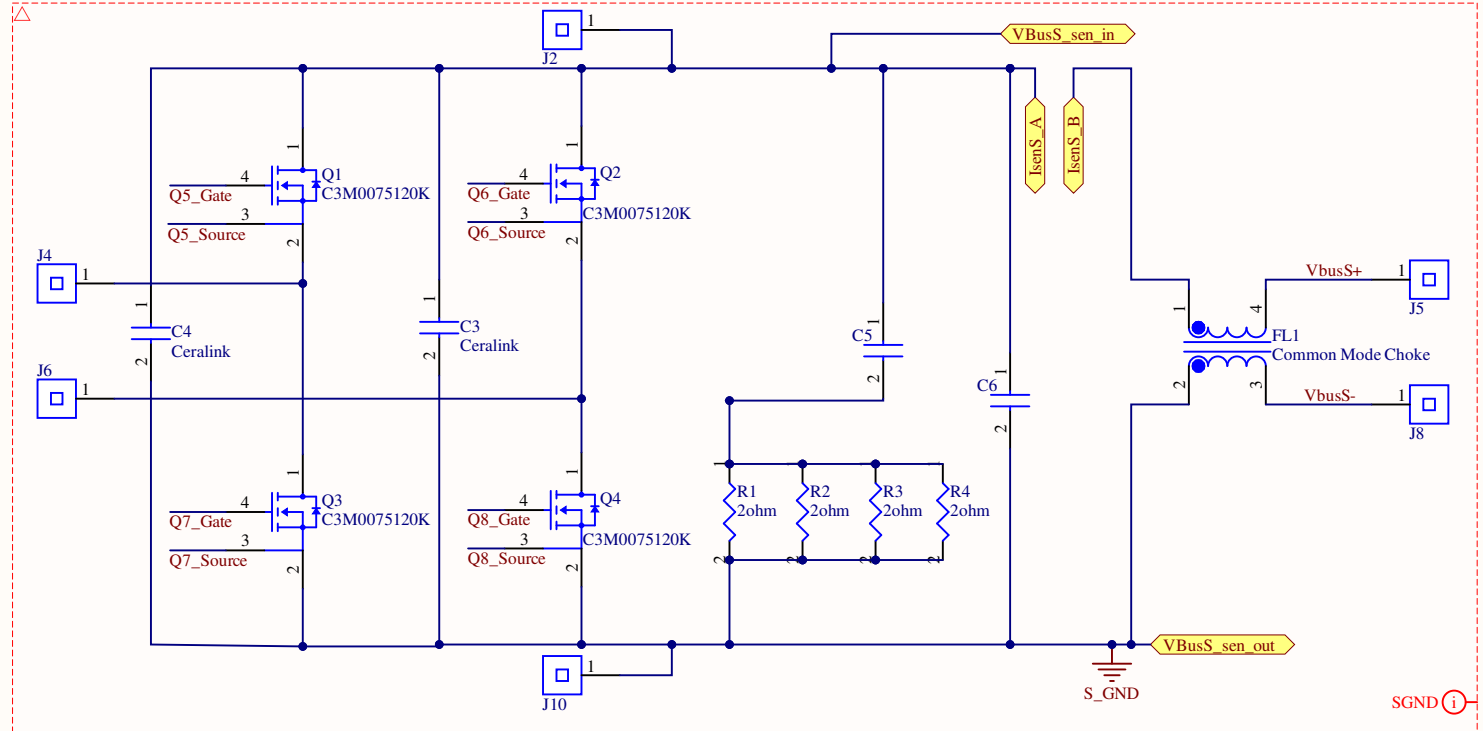
Note. Own authorship.

### A.2 DAB SCHEMATICS

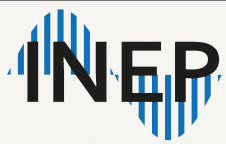
On the last pages are shown the schematics for the DAB project, with the primary and secondary components, DSP command board. Along with the main components, is also present the measurements components for current and voltage for further studies on future works.



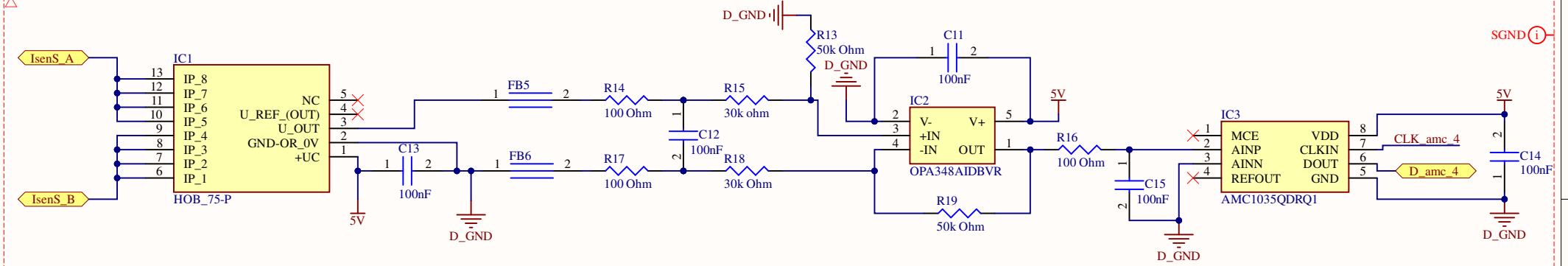
|   |                 |               |
|---|-----------------|---------------|
| Executor: Rossano Mendes Sotoriva                         |                 |               |
| Título do projeto: DAB_PCB_Project.PrjPcb                 |                 |               |
| Arquivo: DSP_049.SchDoc                                   |                 |               |
| Tamanho: A4   | Revisão: *      |               |
| Data: 14/05/2024  | Tempo: 14:32:46 | Folha: 6 de 6 |
| <a href="https://inep.ufsc.br/">https://inep.ufsc.br/</a> |                 |               |



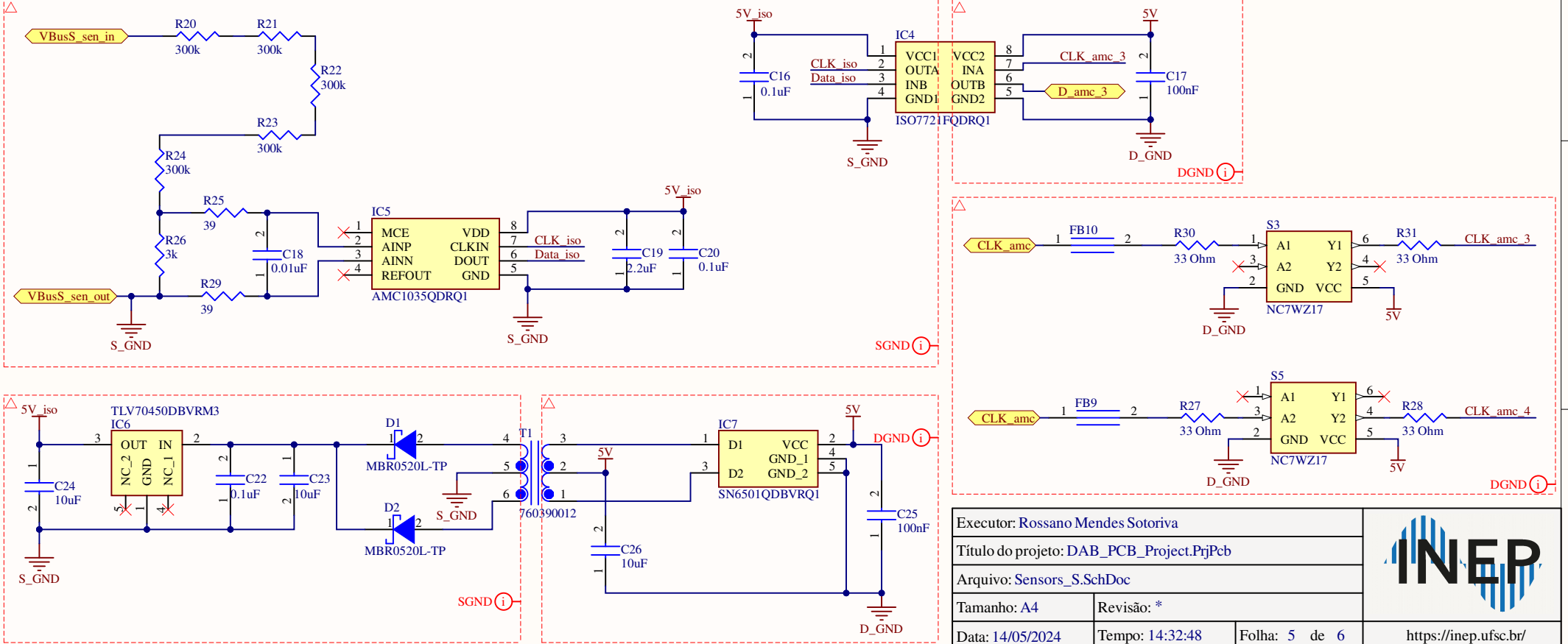
H1  
Heatsink  
Rep

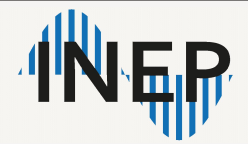
|   |                 |   |                       |
|---|-----------------|---|-----------------------|
| Executor: Rossano Mendes Sotoriva         |                 |  |                       |
| Título do projeto: DAB_PCB_Project.PrjPcb |                 |   |                       |
| Arquivo: Secondary.SchDoc                 |                 |   |                       |
| Tamanho: A4                               | Revisão: *      |   |                       |
| Data: 14/05/2024                          | Tempo: 14:32:47 | Folha: 3 de 6   | https://inep.ufsc.br/ |

Current sensor - Secondary



Voltagesensor - Secondary

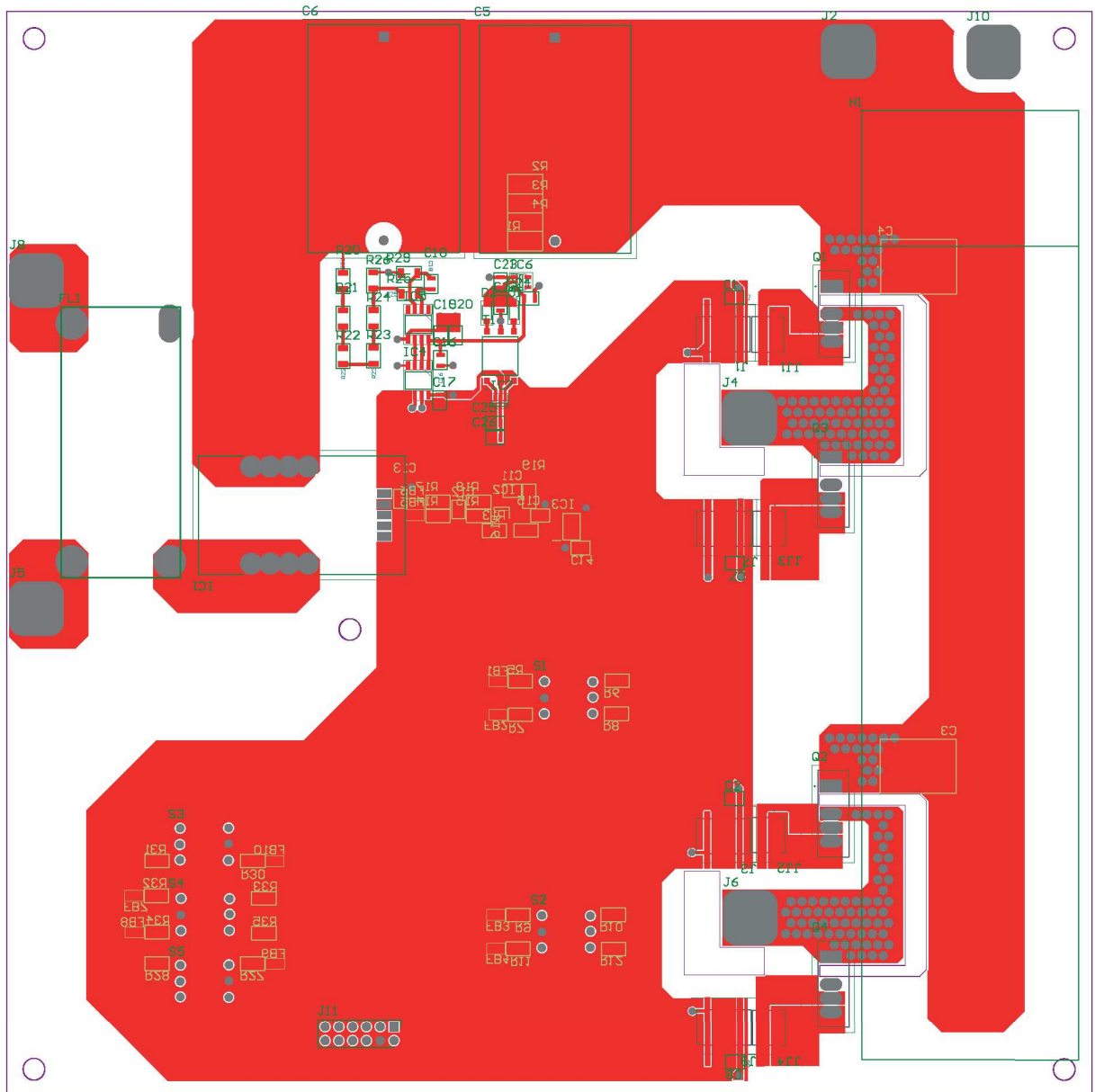


|   |                 |   |   |
|---|-----------------|---|---|
| Executor: Rossano Mendes Sotoriva         |                 |  |   |
| Título do projeto: DAB_PCB_Project.PrjPeb |                 |   |   |
| Arquivo: Sensors_S.SchDoc                 |                 |   |   |
| Tamanho: A4                               | Revisão: *      |   |   |
| Data: 14/05/2024                          | Tempo: 14:32:48 | Folha: 5 de 6   | <a href="https://inep.ufsc.br/">https://inep.ufsc.br/</a> |

### A.3 DAB LAYOUT

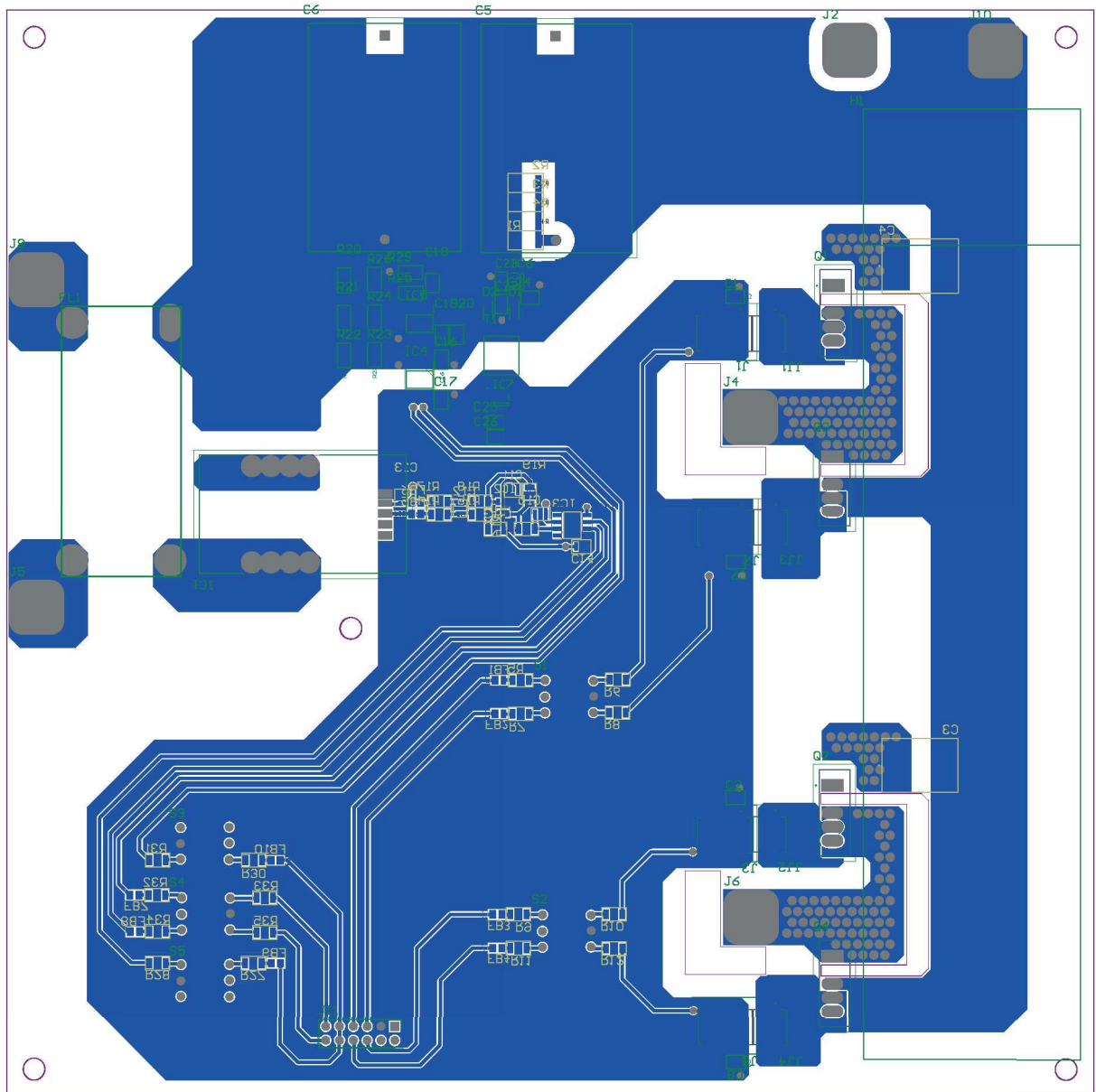
The schematic for the DAB converter is presented the PCB layout developed in the present study with the main converter layout being shown in the Figures A.1 and A.2 and the command board layout being shown in the Figures A.3 and A.4.

**Figure A.1** – DAB top layer.



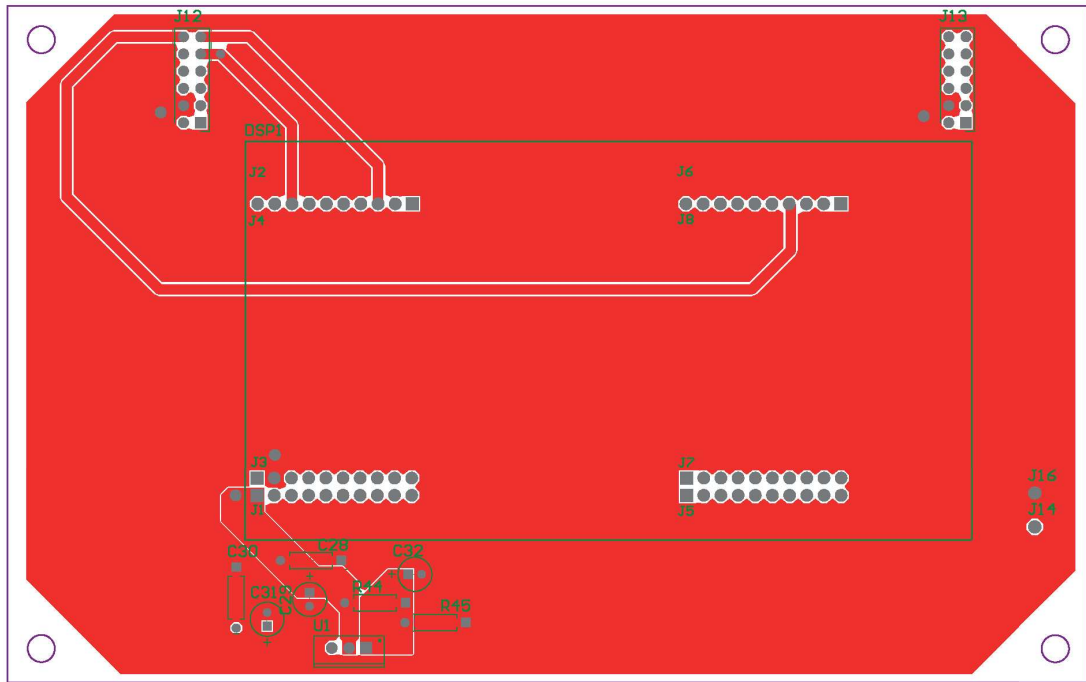
Note. Own authorship.

Figure A.2 – DAB bottom layer.



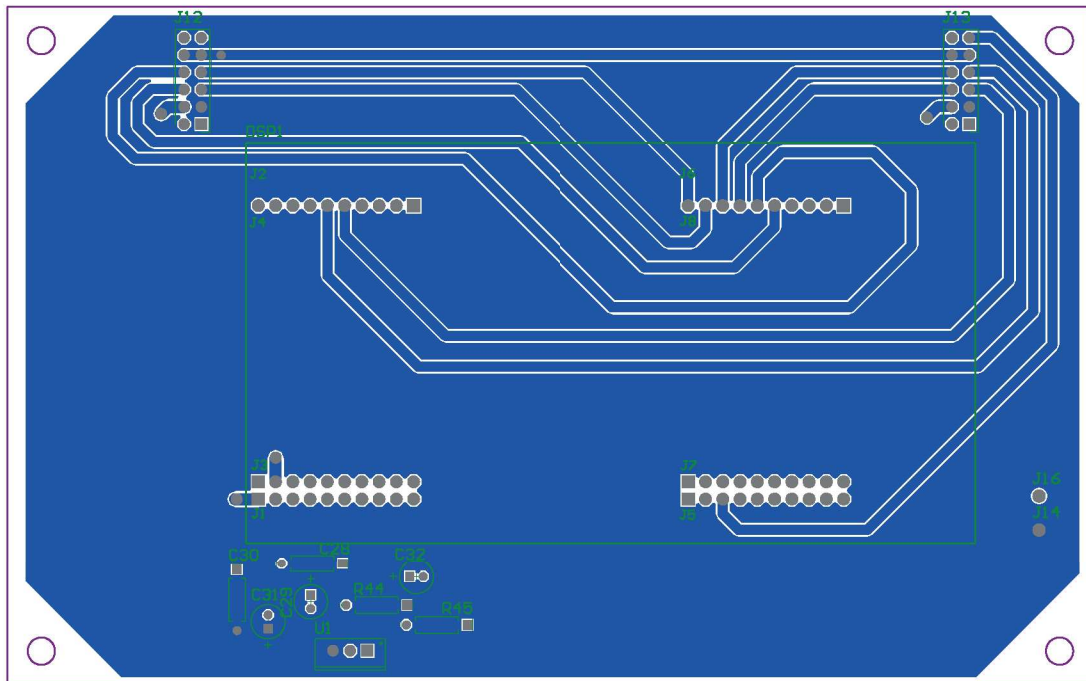
Note. Own authorship.

**Figure A.3** – DAB command board top layer.



Note. Own authorship.

**Figure A.4** – DAB command board bottom layer.



Note. Own authorship.